DESIGN OF A VARIABLE-TEMPERATURE SCANNING TUNNELING MICROSCOPE TO STUDY REACTION INTERMEDIATES IN HETEROGENEOUS CATALYSIS

THÈSE N^{O} 2982 (2004)

PRÉSENTÉE À LA FACULTÉ SCIENCES DE BASE

Institut de physique des nanostructures

SECTION DE PHYSIQUE

ÉCOLE POLYTECHNIQUE FÉDÉRALE DE LAUSANNE

POUR L'OBTENTION DU GRADE DE DOCTEUR ÈS SCIENCES

PAR

Sarah R. LONGWITZ

physicienne diplômée de l'Université de Berne
de nationalité suisse et originaire de Hochdorf (LU)

acceptée sur proposition du jury:

Prof. H. Brune, directeur de thèse
Prof. P. Aebi, rapporteur
Prof. G. Dietler, rapporteur
Prof. C. Henry, rapporteur

Lausanne, EPFL
2004

Abstract

Catalytic processes and in particular heterogeneous catalysis are vital for todays industry. However, many industrial catalytic processes require high temperatures and pressures to work efficiently. This stands in contrast to biological catalysts, which function under ambient temperatures and atmospheric pressures and excel in catalytic activity and selectivity. We may learn something from nature by studying the size-dependent reactivity of small metal particles resembling the active centers of biological catalysts. The catalytic properties of such metal clusters grown on suitable substrates can be investigated by scanning tunneling microscopy. Single-molecule vibrational spectroscopy at low temperatures allows one to identify adsorption sites and measure adsorption energies of reaction intermediates.

We have designed and mounted a variable-temperature scanning tunneling microscope dedicated to the study of reaction intermediates. Our beetle-type microscope is protected against external vibrations by a double-stage spring suspension system. It hangs inside two copper radiation shields, which are directly screwed onto a liquid He-flux cryostat. The microscope ramps for coarse approach are made of sapphire and reside on copper-beryllium balls. Direct electrical contacts to the sample for exact temperature reading exist. The microscope eigenresonances all lie beyond the critical frequency range of 1–10 kHz and rattling resonances are efficiently suppressed. The microscope has proved to work in air. Images of highly-oriented pyrolytic graphite in air were acquired, which showed that spectroscopic measurements are feasible. At the same time, during the microscope mounting period, several mechanical problems were identified and therefore suggestions for future improvements are made.

With the goal of finding a suitable substrate for our future model catalysts, we investigated ultrathin MgO layers on Mo(100) by low-energy diffraction and Auger electron spectroscopy. Defect-free thin oxide film with a superstructure can serve as templates for the growth of a regular array of small metal clusters. We report on the formation of a c(2×14) superstructure of 2.5 ± 0.4 ML of MgO on Mo(100)–(1×1)–O upon annealing at 1300 K. The observed structure is most probably induced by an interfacial reconstruction of the oxygen-covered Mo(100) surface since the annealed Mo(100)–(1×1)–O substrate exhibits a similar LEED pattern. This means that the reordering of the interface upon annealing is decisive for the oxide overlayer structure.

To investigate the growth of small metal islands we studied the two systems Co/Pt(111) and Pt/Pt(111). 0.1 ML Co or Pt were evaporated onto Pt(111) at 50 K and the island size as a function of annealing temperature

was imaged using a variable-temperature scanning tunneling microscope. For both systems we observe a stepwise increase of the mean island size, which can be well reproduced by kinetic Monte-Carlo simulations and mean-field nucleation theory calculations. This behaviour stands in contrast to the Ostwald ripening previously observed for Ag/Pt(111). It indicates that for Co/Pt(111) and Pt/Pt(111) the energy migration barriers of monomers, dimers and trimers must be significantly lower than the respective dissociation barriers.

Finally, high-pressure scanning tunneling microscopy was used to study the adsorption of CO on Pt(111) at room temperature and in equilibrium with the gas phase. The coverage is found to vary continuously and over the whole range from 10^{-6}–1 bar pressure-dependent moiré patterns are observed. This stands in contrast to the CO/Pt(111) lattice gas structures found at low temperatures in the same coverage range. Nevertheless, a true pressure gap cannot be established since sufficient cooling of the sample leads to the formation of hexagonal CO overlayers similar to those at high pressure. We found that below $1.3 \cdot 10^{-2}$ mbar the moiré superlattice is oriented along a 30° high symmetry direction of the substrate while near to 1 bar it becomes compatible with a $\left(\sqrt{19} \times \sqrt{19}\,\right)$ R23.4°-13CO commensurate structure.

Résumé

Les processus catalytiques ont une importance primordiale pour l'industrie de nos jours. Mais souvent, une bonne performance des catalyseurs industriels impliquent des pressions et températures très élevées. Au contraire, les catalyseurs biologiques fonctionnent à la pression atmosphérique et à une température ambiante, et en plus ils sont inégalés au niveau de l'activité et de la sélectivité catalytique. Donc, il est intéressant d'étudier la réactivité de particules métalliques, qui ressemblent aux centres actifs de catalyseurs biologiques, en fonction de leur taille. La déposition de tels clusters sur un substrat adéquat permet d'examiner leurs propriétés par un microscope à effet tunnel. On trouve les sites et les énergies d'absorption des molécules a l'aide de mesures spectroscopiques effectuées sur la molécule isolée.

Nous avons conçu et monté un microscope à effet tunnel, dédié aux études de produits intermédiaires dans la catalyse hétérogène. Notre microscope de type beetle est protégé contre des vibrations extérieures par un système de ressorts de suspension à deux niveaux. Il est suspendu à l'intérieur de deux écrans de radiation thermique en cuivre, qui sont directement vissés sur un cryostat à flux d'hélium liquide. Les rampes en saphir pour l'approche macroscopique reposent sur des billes en cuivre-beryllium. Des connections thermocouples sont en contact direct avec l'échantillon, ce qui donne des températures très précises. Les résonances propres du microscope se trouvent au-delà de la gamme critique de 1–10 kHz et peu de résonances rattling sont détectées. Le microscope a été testé à l'air, en faisant des mesures sur un échantillon de graphite (highly-oriented pyrolytic). D'après les résultats obtenus, des mesures spectroscopiques semblent réalistes. En même temps, nous avons pu identifier plusieurs problèmes mécaniques durant la période de construction et ainsi nous donnons des suggestions pour des futures améliorations.

Le but étant de trouver un substrat adéquat pour nos futures particules catalytiques, nous avons étudié des couches ultraminces de MgO sur Mo(100), en utilisant la diffraction d'électrons à basse énergie et la spectroscopie Auger. Des couches minces d'oxide avec une surstructure constituent des substrats excellents pour la croissance de plots d'îlots métalliques. Nous observons la formation d'une surstructure $c(2 \times 14)$ de 2.5 ± 0.4 ML de MgO sur Mo(100)–(1×1)–O après un recuit de la surface à 1300 K. Cette structure est probablement provoquée par une reconstruction interfaciale de la surface de molybdène couverte d'oxygène, puisque le recuit du substrat Mo(100) Mo(100)–(1×1)–O crée la même image de diffraction. Cela signifie que la reconstruction de l'interface a une influence cruciale sur la structure de la couche d'oxide.

Pour étudier la croissance d'îlots métalliques, nous nous sommes intéressés aux deux systèmes Co/Pt(111) et Pt/Pt(111). L'évaporation de 0.1 ML de Co ou de Pt sur Pt(111) à 50 K était suivi par la mesure de la taille moyenne d'îlots en fonction de la température de recuit avec un microscope à effet tunnel. Nous observons une augmentation de la taille moyenne par palier, ce que nous reproduisons par des simulations Monte-Carlo cinétiques et des calculs basés sur la théorie de nucleation de champ moyen. Ce comportement contraste avec le mûrissement d'Ostwald, qui a été observé pour le sytème Ag/Pt(111), et prouve que pour Co/Pt(111) et Pt/Pt(111), la barrière d'énergie de diffusion des monomères, dimères et trimères est nettement inférieure à la barrière de dissociation.

Finalement, nous avons étudié l'adsorption de CO sur Pt(111) à température ambiante et à l'équilibre avec la phase gazeuse, à l'aide d'un microscope à effet tunnel à haute pression. Le recouvrement varie de manière continue dans toute la gamme de pression de 10^{-6} bar à 1 bar et nous trouvons des structures moiré, par contraste aux structures "lattice gas", qui ont été rapportées pour des températures basses pour des mêmes taux de recouvrement. Pourtant, ceci ne correspond pas à un vrai "pressure gap" puisqu'on retrouve aussi des structures hexagonales à très basse température après un temps assez long de mesure. Nous trouvons que la structure moiré est orienté selon une direction de haute symétrie (30°) par rapport à la surface Pt(111) au-dessous de $1.3 \cdot 10^{-2}$ mbar et qu'elle approche une structure commensurable $\left(\sqrt{19} \times \sqrt{19}\right)$ R23.4°-13CO proche de la pression atmosphérique.

Contents

Chapter 1

Scientific Motivation: Model Catalysts

Catalytic processes play a crucial role in todays industry, as e.g. for the cleaning of car exhaust, the production of ammonia fertilizers, or processes in fuel cells [1]. When the catalyst is in a another phase than the reactants and products, the process is called heterogeneous catalysis. Often the catalyst is solid and the reactants are in the gas phase.

The performance of a catalyst is (apart from its intrinsic properties) determined by the reaction conditions, which include temperature and pressure. Unlike industrial catalysis, biological catalytic processes usually take place at ambient temperature and atmospheric pressure. Biological catalysts are enzymes, which are indispensable for plants, animals and human life. They control essentially every aspect of the chemistry in living cells. Biological catalysts are composed of proteins, which can contain metallic complexes. Nature has developed them to perfection regarding catalyst selectivity and activity.

One example of biological catalysis is the case of nitrogen reduction, a catalytic process used by plants to transform nitrogen into a metabolically usable form. The active center for this catalytic process turned out to be a metal-sulfide cluster ($MoFe_7S_9$) (see [2, 3] and refs. therein). According to recent density functional calculations [4], the nitrogen molecules adsorb on the cluster and are subsequently hydrogenated by protons and electrons arriving from the electrolytic cell environment. At no time during the reaction process does nitrogen dissociation occur. A first ammonia molecule splits directly from the reduced nitrogen molecule, followed by a second ammonia molecule after further reduction of the remaining nitrogen atom.

This process stands in contrast to industrial ammonia production, where the reaction proceeds via dissociation of N_2 and H_2 on iron or ruthenium particles exhibiting single crystal facets and subsequent hydrogenation of the adsorbed N atoms. To avoid contamination of all the reactive surface by strongly bound H and N atoms [5], the reaction must take place at about 400°C, which shifts the chemical equilibrium toward the reactants. To counterbalance this shift the pressure has to be increased up to about 100 bar.

The fact that biological catalysts work efficiently at ambient temperatures and pressures suggests that the currently used industrial catalysts might be significantly improved by learning from nature [6]. It is therefore interesting to investigate model catalysts with the size and composition of biological catalytic clusters in order to learn more about the basic mechanisms of the reaction processes.

It is known that structural properties greatly influence the reactivity of a catalyst [7–10]. The reactive centers on surfaces are often low-coordinated sites such as step and kink sites (see e.g. [9, 10]). A small cluster has a particularly high number of such low-coordinated sites. If metallic clusters are deposited on an appropriate surface they can be studied by STM. An STM can image the surface at intermediate stages of the catalytic reaction if the temperature is low enough to slow down the reaction sufficiently. A new technique involving the acquisition of vibrational spectra of single adsorbed molecules [11] allows the determination of binding sites and energies of the reactants and possibly of intermediate products. Binding sites and energies yield important information about the catalytic process. Hence the STM is a valuable tool to investigate the underlying principles of catalytic reactions on the atomic scale. The present work involves the design and construction of a variable-temperature STM to study catalytic reaction intermediates on clusters.

STM measurements require, however, a conductive sample while the substrate for the metal clusters should preferably be a non-reactive oxide. This leads us to the use of a thin oxide layer on a metal substrate as cluster template [12, 13]. Ultrathin oxide layers can exhibit a near bulk oxide band gap and tunneling through or into/from the oxide layer is possible (see e.g. [14]). When the oxide layer exhibits a superstructure, regularly spaced clusters with a narrow size distribution can be grown. The growth of superstructured thin oxides layers was one goal of this work, while a further chapter relates to the growth of metallic cluster arrays.

Chapter 2

Experimental Techniques

2.1 Scanning Tunneling Microscopy

This chapter provides some essential information on scanning tunneling microscopy. I start with giving a brief historical overview of the scanning tunneling microscope, focusing on the pioneering work. This is followed by an introduction into the main technical features and measurement modes of an STM. Finally, the theoretical principles of the STM are reviewed.

2.1.1 History

The idea of vacuum tunneling dates back to the very beginning of tunneling spectroscopy [15]. Attempts to measure a vacuum tunneling current were made by various scientists [16, 17]. The main obstacle to this kind of experiment were the vibrations transmitted to the tunneling unit, which render the distance between the two electrodes and thus the tunneling current very instable. In 1982 Binnig and Rohrer et al. reported on reproducible results on tunneling through a well-defined vacuum gap between a tungsten tip and a platinum plate [18]. They had overcome the vibration problem by a mechanical isolation system which included magnetic levitation.

The research of Binnig and Rohrer had been prompted by a major issue in the semiconductor industry at this time, which was the problem of inhomogeneities on the nanometer scale. Such inhomogeneities had become increasingly important due to the progressive miniaturization of electronic devices. The original idea of Binnig and Rohrer was actually to perform vacuum tunneling spectroscopy to study inhomogeneities in thin oxide layers on metals on a local scale (< 100 Å) [19, 20]. But soon they realized that scanning over a surface with a positionable tip could deliver topographic images.

The concept of surface scanning with a tip was in fact already applied much earlier by Young et al. [21]. Young et al. constructed a machine called Topografiner to measure the microtopography of a metal surface. They measured the field emission current between tip and surface while scanning. Using a tungsten tip and a platinum surface Young et al. even observed tunneling currents [22].

Binnig and Rohrer, apparently without knowing of the work of Young et al. [22] developed their scanning tunneling microscope (STM) and first images of surface reconstructions and monoatomic steps of $\mathrm{CaIrSn_4}(110)$ and Au(110) were published in 1982 [23]. A large part of the scientific community remained, however, sceptical about the physical reality of the results until Binnig and Rohrer could present measurements of the (7×7) reconstruction of Si(111) in 1983 [24].

At this time Binnig and Rohrer had built an STM working in UHV that was protected against vibrations by a double-stage spring system with eddy-current damping. They achieved atomic resolution, did first chemical imaging [25], and performed first scanning tunneling spectroscopy (STS) measurements [26, 27]. Other groups started to build STMs. Imaging under ambient-air pressure [28] and in liquids became possible and the first low-temperature STM was developed [29], followed later on by the first variable-temperature STM [30, 31]. Furthermore, the tunneling microscope has evolved from a merely measuring device to a tool allowing surface manipulation on the nanoscale [32, 33]. At the same time it is increasingly used in the fields of materials science and biology. With its unique capability of measuring surface properties on an atomic scale, the STM has become one of the most important tools in surface physics and nanoscience.

Recently, vibrational spectroscopy on single molecules adsorbed on a metal surface has been performed [11], an idea that was already expressed by Young et al. in 1971 [22]. With their experiment Stipe et al. [11] carried out the original vision of Binnig and Rohrer of local tunneling spectroscopy with a resolution beyond expectation.

2.1.2 Basic Principles

The main features of a scanning tunneling microscope can be seen in Figure 2.1. A sharp metal tip is brought into close proximity of a sample surface until a gap of only a few Ångströms is formed. Between tip and sample a voltage difference (tunneling voltage) of up to a few Volts is applied. Due to the overlap of the electron wavefunctions of tip and sample, which extend into the gap, a current referred to as tunneling current can flow between tip and sample. This current crucially depends on the distance between tip and sample, i.e. the tunneling gap width, which is always affected by thermal instabilities and mechanical vibrations. To control the tip-sample distance the measured tunneling current is fed into a feedback loop. The tunneling gap width is then readjusted by means of a piezoelectric transducer.

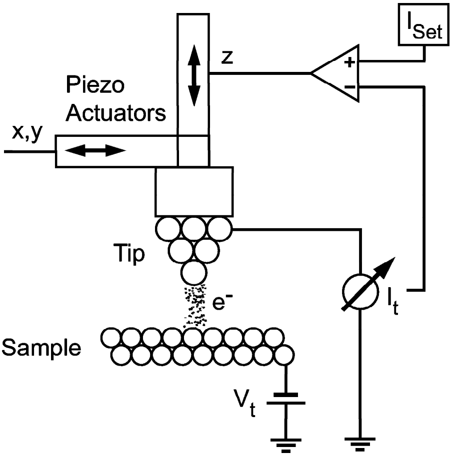

Figure 2.1: Basic principles of a scanning tunneling microscope. A conductive tip is brought close to a sample surface, which is held at a potential V_t with respect to the tip, and the tunneling current I_t is measured. Piezo actuators are used for height correction and lateral displacement of the tip.

A scanning tunneling microscope can be operated in different modes. The original first and most often used mode is the so-called constant current mode. In this mode the tip is raster-scanned laterally over the sample surface at constant current by means of piezoelectric transducers as is shown in Figure 2.1. During each scan step geometric height variations but also variations in the electronic structure of the surface may induce a change in current. Therefore, while scanning the actual current is continuously measured and compared to the set current and the feedback loop in the electronic circuit leads to a retraction or approach of the tip with respect to the sample whenever the current exceeds or falls below its setpoint. The height correction of the tip (z-signal) thus reflects the local electronic and geometric properties of the surface. It can give a nearly topographic image of the sample surface in cases where the geometrically induced height variations dominate, which is often the case for pure metal surfaces.

Another frequently used STM mode is called tunneling spectroscopy. Here, the feedback loop and the lateral scanning are temporarily switched off and during this time the tip should remain at a fixed position above the sample surface. A usually linear sweep in tunneling voltage is performed while recording the tunneling current. Very often, especially if one has to deal with small variations in current, it is preferable to measure the first and/or second derivative of the current with respect to the voltage using lock-in technique. The resulting spectroscopic data yield information about the local electronic structure of the sample surface convoluted with the one of the STM tip.

The two measurement modes can also be combined. One can perform tunneling spectroscopy after each step during a surface scan. This allows to map spatial variations in the local density of states (see e.g. [34]).

For further information on the principles and the use of the STM, see e.g. [35, 36].

2.1.3 Theory

In the following I always refer to an STM working in a UHV environment. Figure 2.2 shows a schematic view of an STM tunneling unit. If a voltage between tip and sample is applied, electrons may tunnel from filled tip states to empty sample states or vice versa. In order to calculate this tunneling current, one needs to exactly know the electronic states of both tip and sample as well as the electron potential in the tunnel gap region. Apart from the fact that detailed information is missing, in particular on the shape and the chemical composition of the tip apex and thus its electronic properties, only rough approximate calculations can be made due to the complexity of the issue. A few models have, however, been developed during the past twenty years.

First, Tersoff and Hamann [37, 38] applied Bardeen's [39] formalism to the tunneling microscope. The tunneling current is given to first order by

$$I = \frac{2\pi e}{\hbar} \sum_{\mu,\nu} f(E_\mu - eV)\,[1 - f(E_\nu)]\; |M_{\mu\nu}|^2\; \delta(E_\mu - E_\nu)\ , \tag{2.1}$$

where $f(E)$ is the Fermi function, V is the applied voltage, $M_{\mu\nu}$ is the tunneling matrix element between states ψ_μ of the tip and ψ_ν of the surface, and E_μ is the energy of the state ψ_μ in the absence of tunneling. The main problem is then to evaluate the matrix element $M_{\mu\nu}$. The starting point for

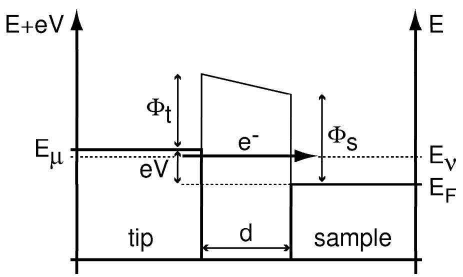

Figure 2.2: Schematic view of the tunneling process. The tip-sample distance is d and a voltage V is applied between tip and sample. Φ_t and Φ_s are the work functions of tip and sample, respectively. An electron can elastically tunnel from a tip electronic state E_μ into a sample electronic state E_ν.

Tersoff and Hamann's calculation was given by Bardeen [39]:

$$M_{\mu\nu} = \frac{\hbar^2}{2m} \int d\overrightarrow{S} \cdot (\psi_\mu^* \overrightarrow{\nabla} \psi_\nu - \psi_\nu \overrightarrow{\nabla} \psi_\mu^*) \ , \tag{2.2}$$

where the integral goes over any surface lying entirely within the region between tip and surface.

Tersoff and Hamann made the crucial assumption of a spherical tip shape in the tunnel gap region. They considered a tip of radius R with center of curvature at r_0. The wave functions of the tip extending into the tunneling gap are then assumed to have a spherical form. For simplicity the work function ϕ of the tip is assumed to be equal to that of the sample. Tersoff and Hamann calculated $M_{\mu\nu}$ under these conditions by expanding the wave functions of tip and surface in Fourier space. In the case of tunneling at small voltage and at room temperature or below, this leads to

$$I \propto V R^2 \, \mathrm{e}^{2\kappa R} \rho(\overrightarrow{r_0}, E_F) \quad \text{with} \quad \rho(\overrightarrow{r_0}, E) = \sum_\nu \left|\psi_\nu(\overrightarrow{r_0})\right|^2 \delta(E_\nu - E) \ , \tag{2.3}$$

where $\kappa = \sqrt{2m\phi}/\hbar$ is the minimum inverse decay length of all surface wave functions in the vacuum gap. Note that only sample and no tip wave functions appear in this equation. In fact, $\rho(\overrightarrow{r}, E_F)$ is simply the surface local density of states at the Fermi energy at point $\overrightarrow{r}$. Finally, the surface wave function ψ_ν decays exponentially within the tunnel gap:

$$\left|\psi_\nu(\overrightarrow{r_0})\right|^2 \propto \mathrm{e}^{-2k(R+d)} \quad \Rightarrow \quad I \propto V R^2 \, \mathrm{e}^{-2kd} \sum_\nu \delta(E_\nu - E) \ . \tag{2.4}$$

Thus the tunneling current depends exponentially both on tip-sample distance and on the inverse decay length. For a typical value of $\phi \approx 4$ eV, the current decreases by roughly one order of magnitude for each Ångström increase in tip-sample distance. The tunneling current is also proportional to the number of electronic states of the sample at the Fermi level.

Tersoff and Hamann [37, 38] also calculated the corrugation amplitude Δ defined as the difference between the extremal values of the tip height z for the constant current mode. They consider the case of scanning at sufficiently large distances from the surface, where $\rho(\vec{r}, E)$ becomes rather smooth, and obtain the result

$$\Delta \propto \mathrm{e}^{-\beta z} \ , \ \beta \approx \frac{1}{4}\kappa^{-1} G_1^2 \ , \tag{2.5}$$

where G_1 is the smallest surface reciprocal-lattice vector. The corrugation amplitude also depends exponentially on the distance z. Its decay length is determined by the surface lattice periodicity. Structures related to a large surface unit cell have a small G_1 and thus a high corrugation decay length. Consequently, they can be imaged at much larger distances from the surface as compared to small structures.

In the general case of a considerable tunneling voltage the evaluation of Equation 2.1 becomes more complicated. An electron may in this case not only tunnel into the surface electronic states at E_F but into any state E lying between E_F and $E_F + eV$ as indicated in Figure 2.2. As an approximation we may assume that the current produced by electrons tunneling into a surface energy level E is proportional to the surface local density of states at that energy level $\rho(E)$ [40, 41]. One then obtains the total current by integrating over all available surface energy levels between E_F and $E_F + eV$:

$$I \propto \int_{E_F}^{E_F+eV} dE \ \rho(E)\, T(E, V, d) \ , \tag{2.6}$$

where T is a transmission factor accounting for the tunneling barrier. T can be approximated using the average barrier $\left((\Phi_t + eV) + \Phi_s\right)/2$, where Φ_t and Φ_s are the work functions of tip and sample [41] (see Figure 2.2).

$$T = \mathrm{e}^{-2d\sqrt{\frac{m}{\hbar^2}}\sqrt{\Phi_t + \Phi_s + eV - 2(E - E_F)}} \ . \tag{2.7}$$

The transmission factor depends exponentially on the tunneling gap distance d. Electrons from higher energy levels are more likely to tunnel because of the reduced barrier height.

During tunneling spectroscopy measurements the first and second derivatives of the tunneling current are measured. According to Equation 2.6 the first derivative is proportional to the electron local density of states (LDOS) times the transmission factor:

$$\frac{\mathrm{d}I}{\mathrm{d}V} \propto \rho(E)\,T(E,V,d)\ . \tag{2.8}$$

Stroscio and co-workers [42] showed that in some cases $\mathrm{d}I/\mathrm{d}V$ divided by I/V reflects reasonably well the surface LDOS. In general, however, the appropriate method to display spectroscopy results depends on the problem at hand [35].

2.2 Low-Energy Electron Diffraction

In this section a short introduction to low-energy electron diffraction (LEED) as a surface characterization method revealing the geometrical structure of the surface is given. LEED measurements were part of the experiments that will be described in Section 4.1.

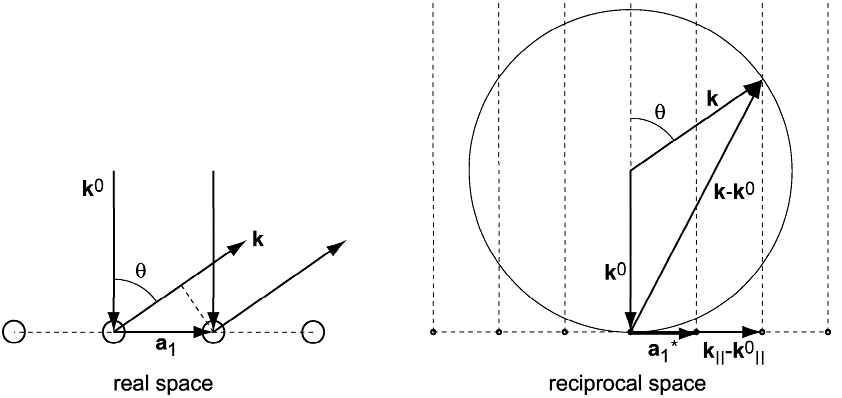

Figure 2.3: Low-energy electron diffraction for a perpendicular incident beam with wave vector $\mathbf{k}^0$. $\mathbf{a}_1$ and $\mathbf{a}_1^*$ are the surface lattice vector and reciprocal vector, respectively. The diffracted beam wave vector $\mathbf{k}$ lies in the $\mathbf{k}^0 - \mathbf{a}_1$ plane.

In a LEED experiment electrons with a de Broglie wavelength in the order of typical interatomic spacings, which corresponds to an energy of

20–500 eV, are elastically backscattered from a crystal surface. The mean free path for electrons in a solid takes a minimum at typical LEED energies and the diffracted electron beam thus yields structural information only about the first 2–3 monolayers. The elastically backscattered electrons are accelerated onto a fluorescent screen, where the two-dimensional diffraction pattern can be seen, representing basically the Fourier transform of the surface atom arrangement.

The location of the maxima of the diffracted electron beam can be explained by a simple geometrical theory. Maxima occur at angles determined by the Laue condition (see also Figure 2.3)

$$\mathbf{k}_{\|} - \mathbf{k}^0_{\|} = h_1\,\mathbf{a}^*_1 + h_2\,\mathbf{a}^*_2 \ , \tag{2.9}$$

where $\mathbf{k}^0$ and $\mathbf{k}$ are the wave vectors of the incident and scattered electron waves, $\mathbf{a}^*_1$ and $\mathbf{a}^*_2$ are the reciprocal lattice vectors, and h_1 and h_2 are integers. The Laue condition can be illustrated in reciprocal space by the Ewald sphere as shown on Figure 2.3. From $a^*_1 = 2\pi/a_1$, $a^*_2 = 2\pi/a_2$, and $k = 2\pi/\lambda$, where a_1 and a_2 are the surface lattice constants, it follows that the Laue condition is equivalent to the one-dimensional Bragg relation (cf. Figure 2.3).

$$a_1\,\sin\theta = n\,\lambda \tag{2.10}$$

Backscattered waves from neighboring (identical) atoms interfere constructively if the path difference is a multiple of the wavelength λ.

Within the geometrical theory the exact surface atom positions can in general not be determined because LEED projects information from a three-dimensional real space (a few crystal monolayers) onto a two-dimensional reciprocal space. More information can be gained by performing LEED measurements as a function of electron energy or by studying the intensity variation across the width of a single spot, called spot profile analysis (SPA-LEED). Generally, more elaborate analysis methods include the assumption of a surface model, for which straightforward theoretical calculations are made, also considering multiple scattering. The theoretical results are then compared to intensity variations in the measured LEED pattern.

For further information the reader is referred to [43, 44].

2.3 Auger Electron Spectroscopy

This section gives a very short introduction to Auger electron spectroscopy (AES). AES is generally used to determine the chemical composition of a crystal surface. We used AES for the characterization of our samples.

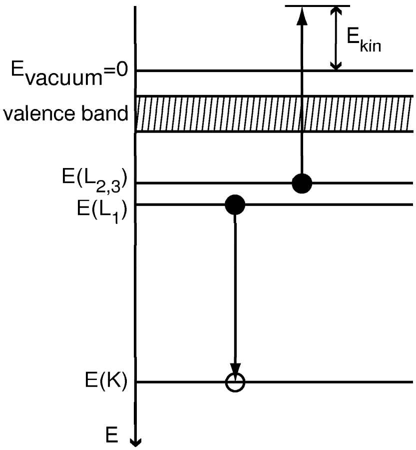

Figure 2.4: Example of an Auger process. An incoming electron creates a hole in the K-shell of the atom, which is subsequently filled by an electron from the L-shell. Due to the liberated transition energy another electron from the L-shell is emitted to vacuum.

In AES an electron beam with an energy of 1–5 keV is directed onto the sample surface and the spectrum of backscattered electrons is measured. When an incident electron collides with a surface atom, it can ionize the atom by creating a hole in one of the inner atom shells. Figure 2.4 gives an example of an Auger process, where the initial hole is created in the K-shell. The K-shell hole is subsequently filled by an electron from an outer shell, in this case from the L_1-shell. The energy liberated by the radiationless transition ($L_1 \rightarrow K$) is transferred to another electron, which is emitted with an energy $E_{kin} = E_K - E_{L_1} - E_{L_{2,3}}$, where E_K is the binding energy of a K-shell electron and E_{L_1} and $E_{L_{2,3}}$ are the binding energies in the L-shells in presence of the K-shell hole. The Auger process shown in Figure 2.4 is denoted as a $KL_1L_{2,3}$ or simply KLL transition, according to the core levels involved. The kinetic energy of an emitted Auger electron depends on the properties of the atom. Each element of the periodic table has got its own characteristic Auger electron energies, which, however, are modified by the chemical environment of the atom. Oxidized or reduced atoms for instance have different Auger energies.

For further information refer to [43, 44].

Chapter 3

Variable-Temperature Scanning Tunneling Microscope Design

3.1 UHV Chamber

The scanning tunneling microscope described in this thesis was designed as part of an existing UHV system. The main UHV chamber with a cylindrical shape is shown in Figure 3.1. In the following, I give a brief description of our UHV system.

The UHV chamber is held by a metallic frame which stands on four standard pneumatic dampers (Newport Corporation). The system consists of the main UHV vacuum chamber and a small chamber that serves mainly to pump on all the lines of the gas inlet system. It also provides the differential pumping of a quadrupole spectrometer and a load-lock (see below).

A home-made manipulator for sample preparation and analysis allows sample cooling by liquid nitrogen or helium down to about 100 K or 60 K, respectively, and sample heating up to 2000 K while staying in the 10^{-10} mbar range. A filament from a commercial halogene light bulb (50 W) is placed at about 0.3 mm from the sample backface for heating by irradiation and, preferably, by electron impact if a positive voltage of up to about 500 V is applied to the sample. We achieve heating rates of 7 K/s through electron bombardment (+400 V applied to sample, 100 mA emission current). The holder contains two pairs of thermocouples to monitor the sample temperature, W–5%Re/W–26%Re and Alumel-Chromel (Omega Engineering Inc.),

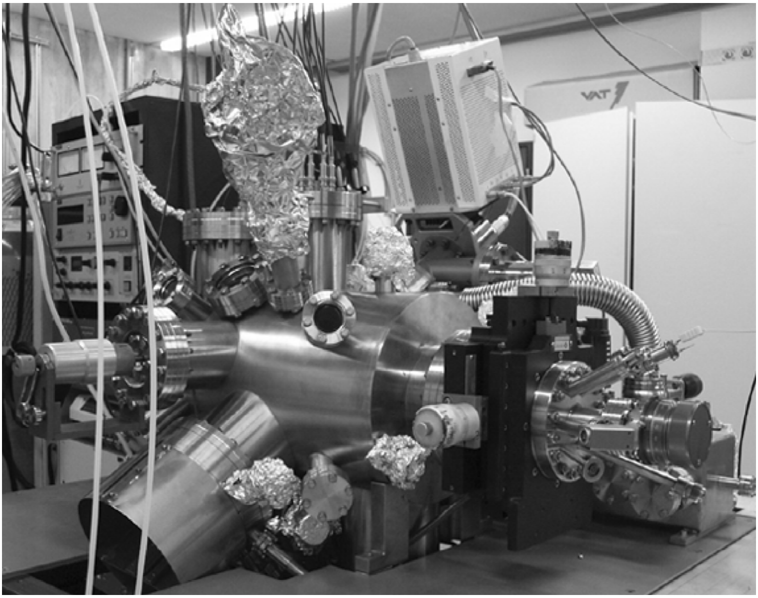

Figure 3.1: UHV chamber equipped with standard sample preparation and analysis instrumentation, including low-energy electron diffraction, Auger electron spectroscopy, and Quadrupole mass spectrometry.

one of which is used depending on the sample.

The sample holder can be rotated around the chamber axis to bring the surface in front of the different surface preparation and analysis instruments, all arranged in the same plane perpendicular to the chamber axis. Our ion gun (Specs GmbH) allows sample bombardment with Ar^+ ions of up to 5000 eV. For metal evaporation onto the surface we have a triple e-beam evaporator (Omicron) and a Knudsen cell (Sci-Cam Ltd). Surface characterization is done by low-energy electron diffraction (Spectaleed, Omicron) and Auger electron spectroscopy (Physical Electronics GmbH). A differentially pumped quadrupole mass spectrometer (QMG 422, Balzers) monitors partial gas pressures in the vacuum chamber and near to the sample surface and allows thermal desorption spectroscopy (TDS) measurements.

A second plane in the vacuum chamber contains the STM flange. Sample transfer between the home-made sample holder and the STM takes place by means of a wobble-stick with a home-made fork-like end. Our chamber also includes a sample storage system and a sample transfer flange separated by a gate valve and serving as load lock to insert and take out samples without opening the chamber.

Both, main and small UHV chamber are equipped with a turbomolecular pump (360 l/s and 150 l/s, Turbovac, Leybold Vakuum GmbH). The main chamber further contains an ion pump and a titanium sublimation pump (Varian Vacuum Products), which permits to switch off the turbomolecular pumps during STM measurements. The UHV pressure is read by ionization pressure gauges (STABIL-ION, Granville-Phillips). After bakeout a base pressure of the UHV chamber down to $7 \cdot 10^{-11}$ mbar has been achieved.

3.2 Microscope Specifications

The new VT-STM is designed to perform single-molecule vibrational spectroscopy at variable temperatures, in addition to standard STM measurements as constant-current imaging. When taking single-molecule vibrational spectra, one records the dependence of the tunneling current on the sample bias at constant tip-sample distance. The tunneling current feedback has to be switched off during the measurement and no height correction can be made. Therefore the stability of the tip-sample distance is crucial. A variation in tip height causes a change in the tunneling current, adding noise to the measurement. The tunneling current typically changes by a few percent upon excitation of vibrational modes [11, 45, 46] but by about 10% upon a change of 0.01 Å in tip height. This means the tunneling gap distance has to be stable in the frequency range of interest with a resolution of about 0.005 Å.

The peak width increases with temperature, which makes peak identification and the determination of peak positions much more difficult at elevated temperatures [46]. To achieve the required resolution, the microscope has to be cooled with liquid helium. The microscope geometry and thermal mass must allow rapid cooldown and a low consumption of liquid helium. One liquid helium dewar of 25 l should last for at least 2 days with 5 h measurement time per day. In addition, the microscope must support temperature cycling.

To achieve high stability we have to deal with two major technical problems: vibration isolation and thermal stability. The microscope has to be protected from external vibrations and at the same time the impact of microscope eigenresonances has to be minimized. For thermal stability we have to take care of heat conduction and radiation, as well as of thermal compensation.

The planned experiments include in situ dosing and for future applications in situ irradiation of the sample. We would also like to study temperature-dependent phenomena. For this purpose, both increasing or decreasing the temperature should be possible in order to investigate hysteresis-like phenomena. When raising the temperature, the sample has to be heated directly. Otherwise there is desorption from the heated surroundings resulting in sample contamination. Finally, it is desirable to get temperature readings as near at the sample surface as possible.

To summarize, the new VT-STM should fulfill the following requirements:

- Thermal stability comparable to that of fixed-temperature STMs, i.e. within 0.01 K
- Good vibration isolation
- Mechanical stability
- In situ dosing and irradiation of sample
- Direct contact to sample for cooling, heating and temperature control

3.3 Microscope Overview

This section gives a descriptive overview of the whole microscope setup. For more details and theoretical considerations about thermal stability, vibration isolation, and the coarse approach mechanism see Sections 3.4, 3.5, and 3.6, respectively.

3.3.1 General

Our microscope design is based on a microscope used by the research group of Ho [47], who was the first to perform inelastic electron tunneling spectroscopy (IETS) on single molecules with an STM[1]. In Figure 3.2 and Figure 3.3 drawings of our microscope can be seen while Figure 3.4 is a picture of the setup toward the final test phase, without radiation shields. The STM is suspended inside two cylindrical electrolytic tough pitched (ETP) copper radiation shields, which are directly screwed onto a liquid helium flux cryostat (Heli-tran LT-3B, Advanced Research Systems, Inc.) and protect the microscope from room temperature radiation. The cryostat is mounted on a flange on top of the chamber, which also contains all electrical feedthroughs.

---

[1] For examples of other home-built low-temperature and variable-temperature STMs see e.g. [48–52]

The inner shield is in contact with the cryostat cold tip at liquid helium temperature while the outer shield is cooled by the helium exhaust gas.

The STM molybdenum base plate consists of a drawer-like piece, which contains the sample holder with the sample. Underneath the sample holder is a molybdenum counterpart disk, which pushes the sample against the top of the drawer by three steel compression springs. The beetle-type STM is mounted on the lid of this drawer. The base plate hangs on an intermediate sapphire plate by three Inconel (X-750, California Fine Wire) suspension springs. The sapphire plate is suspended by three Inconel springs attached to the top of the inner shield. We thus have a double stage damping system. All cables to the STM pass via the sapphire plate. The radiation shields contain sapphire windows serving as cable feedthroughs.

The shields also contain two holes for in situ dosing and irradiation. The holes in the outer shield are closed by shutters (small sliding doors) to avoid room temperature radiation on the sample. Besides that there are vertical sliding doors for sample transfer. The door of the outer shield can be pulled up by a thin wire, which has its other end connected to a rotary drive motion feedthrough and takes the door of the inner shield along with itself.

For sample transfer, the microscope base plate is pulled downwards by means of a bevel gear attached to a flange on one end of the vacuum chamber. The rod moved up and down by the gear traverses the bottom of the outer radiation shield. It then continues as a double rod, which enters the inner shield and pulls a ring attached to the base plate. The double rod helps defining the azimuth angle. When the base plate is pulled down completely it contacts the inner shield. Pulling further results in lowering the molybdenum counterpart disk underneath the sample holder. The sample can then be transferred using a wobble-stick. For rapid cooldown the molybdenum disk has to be released while keeping the base plate in contact with the inner shield. After cooldown, the base plate is released by moving the rod further up. Usually the Inconel springs will retract and the base plate return to its normal position, mechanically decoupled from the bevel gear. If the base plate remains sticking to the inner shield, it can also be pushed actively upwards.

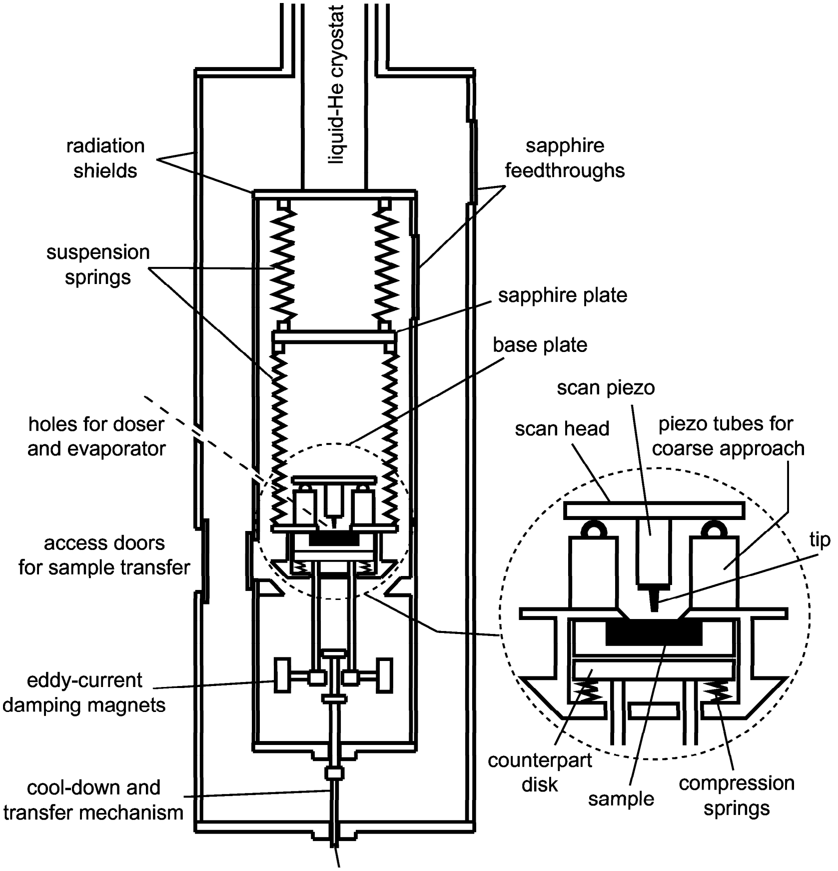

Figure 3.2: Schematic drawing of the VT-STM suspended inside two radiation shields.

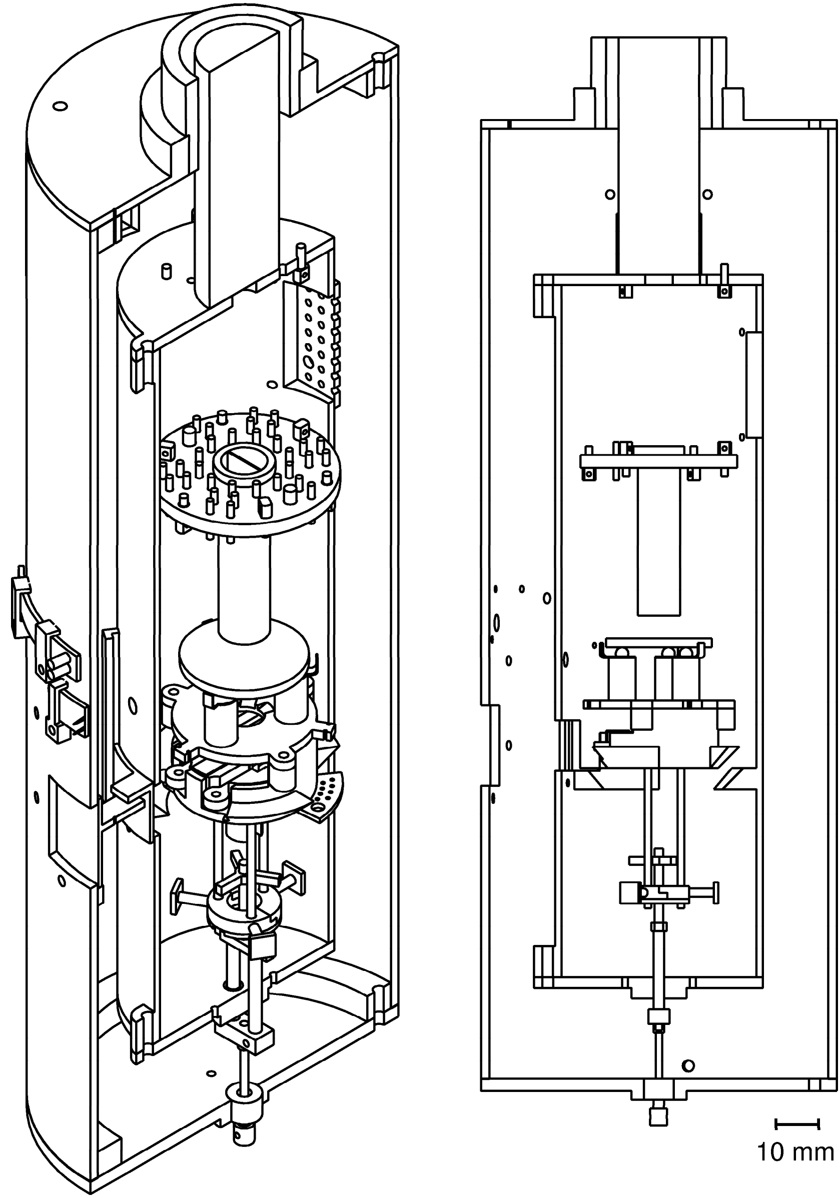

Figure 3.3: Drawing (AutoCAD) of the VT-STM suspended inside two radiation shields. The suspension springs are not shown.

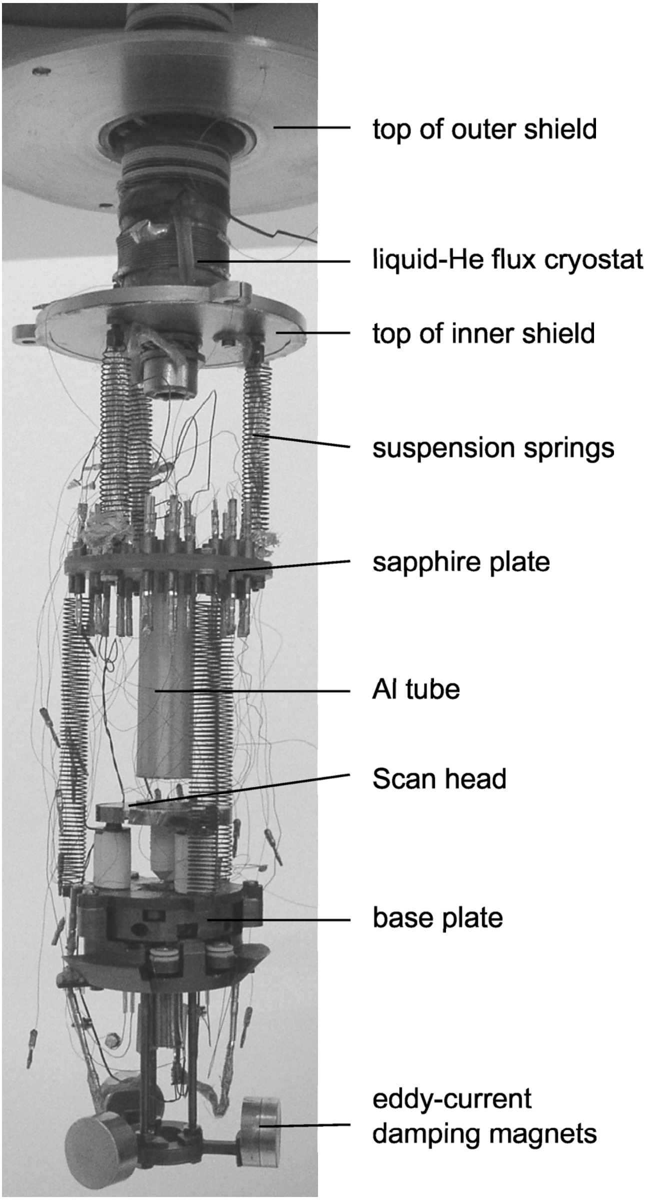

Figure 3.4: STM setup in its test phase.

3.3.2 Base Plate

A schematic view of the STM base plate is depicted in Figure 3.2 while Figure 3.5 shows the base plate at an initial (a) and a later (b) stage. The drawer with its removable lid are made of molybdenum. Inside the drawer the Mo sample holder is placed above a Mo counterpiece. Between the counterpiece and the bottom of the drawer are three compression steel springs, which push the counterpiece and the sample upwards with a total force of about 10 N. The top of the sample holder is therefore in firm thermal contact with the base plate and its height is well defined. The drawer lid has a 8 mm diameter hole, through which the sample surface is accessible. Around the hole there are three piezoceramic tubes (Staveley Sensors, EBL#1) used for coarse approach, sample-tip distance offset, and coarse lateral displacements. Our geometry allows a total displacement of about ∅3 mm on the sample surface. The tubes have an outer diameter of 0.25”, a wall thickness of 0.02” and a length of 0.433”. The x-y electrodes are on their outside while the inner electrode is used for z-offset. The tubes carry the STM scan head.

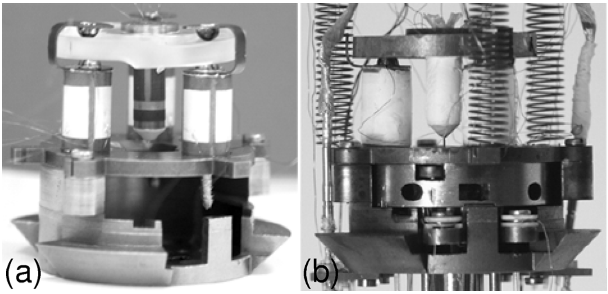

Figure 3.5: (a) STM base plate assembled for testing the coarse approach mechanism. The sample and its counterpiece are not inserted yet. (b) Base plate in the final setup.

A first version of the scan head was a sapphire plate with ramps on both sides as can be seen in panel (a) of Figure 3.5. The ramps were clamped between three pairs of Cu-Be balls in order to increase the contact force between ramps and balls. An increased contact force is advantageous for the stick-slip motion (Section 3.6) and helps eliminating rattling resonances (Section 3.5.2). At the same time the weight of the scan head can be very small, which leads to higher eigenfrequencies of the beetle-type STM (Section 3.5.2). However, the sapphire scan head had to be replaced because of problems with the coarse approach mechanism as discussed in Section 3.6. The improved version of the scan head can be seen in panel (b) of Figure 3.5. The scan head is made of a molybdenum plate, onto which three segments of a flat sapphire ring are glued. These sapphire segments reside on the three Cu-Be balls and serve as ramp material.

For the final setup the electrodes on the piezo tubes were covered with teflon to avoid short-circuits induced by adsorption of metallic particles during in situ dosing.

The scan piezo tube of 0.17" outer diameter, 0.02" wall thickness, and 0.433" length is glued into the molybdenum scan head. The z-electrode and the x-y electrodes on its outside have a length of 1.5 mm and 5.5 mm, respectively, with a spacing of 1 mm. The dimensions were chosen considering the desired dynamical z and the x-y scan ranges. The formulae for the deformation of piezoceramic tubes are

$$\Delta x = \frac{0.45\, d_{31} V L^2}{d_m\, t} \quad \text{and} \quad \Delta L = \frac{d_{31} V L}{t} \quad , \tag{3.1}$$

L : height of electrode
t : tube wall thickness
d_m: tube mean diameter
V : voltage
d_{31}: piezoelectric coefficient.

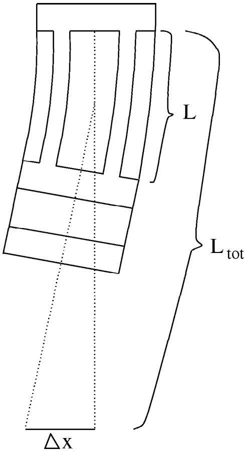

Figure 3.6: Piezo tube deflection.

The Δx in the above formula indicates the horizontal deflection of a tube with electrodes over the whole length. In our case the effective Δx on the sample surface is calculated by taking the x-y electrodes length L and the additional distance down to the sample into account (Figure 3.6). For the case of small deflections simple geometrical considerations lead to

$$\Delta x = \frac{0.45\, d_{31} V L_{tot}^2}{d_m\, t}\,(2R - R^2) \quad , \tag{3.2}$$

where R is the proportion of active length (electrode) to total length L_{tot}(active plus additional, in our case $L_{tot} = 14$ mm).

In our setup the voltage varies between -220 V and $+220$ V. Opposite voltages are applied to opposite electrodes when scanning in the x-y direction and negative as well as positive voltages can be applied to the z-electrode. The inner electrode of the scan piezo tube is grounded. At room temperature the piezoelectric coefficient d_{31} is -1.27 Å/V. This results in about 1650 Å dynamic z-range and 1.6 μm in x and y direction. Near to 4 K the piezoelectric coefficient d_{31} decreases by a factor of about 2.5 [48], which means that at low temperatures the z-range is still at least about 660 Å and the x-y scan range about 0.6 μm.

A Macor piece is glued into the lower end of the scan piezo tube, which contains an oxygen-free high conductivity (OFHC) copper tube of 0.275 mm inner diameter. The tungsten tip wire is inserted from below into this copper tube. The tunneling current cable is glued to the upper copper tube end within the piezo tube. It is shielded by the inner piezo electrode until it gets out of the scan head. For the cables to the outer electrodes ($\pm x$, $\pm y$, z) the molybdenum disk contains five additional holes.

Two pairs of thermocouples, W-Re and Chromel-Alumel, touch the sample directly. Thin flat springs screwed onto the Mo counterpiece and U-shaped wires on the bottom side of the sample holder contact each other. A fifth contact is for the sample bias. A Si-diode as an additional temperature sensor for temperatures down to 4 K is glued onto the Mo counterpiece, in proximity to the sample.

A filament beneath the sample serves for direct sample heating. The filament was supposed to make direct contact to the sample through an appropriate sapphire piece. The idea was to change the sample temperature rapidly and with a low power consumption since the filament temperature would stay below 300 K. The sapphire piece has, however, been taken out of the assembly, because it caused sample transfer problems.

3.3.3 Cabling

The following points must be considered when making electrical connections to the STM: pick-up noise, vibration transmission, and heat transfer. Vibration transmission and heat flows from the room temperature vacuum chamber to the microscope should be minimized. These two points and their impact on the STM cabling design are treated in more detail in Sections 3.4 and 3.5. The minimization of electronic pick-up noise demands careful routing and shielding of the cables.

The cables coming from the vacuum chamber STM flange are passed through the sapphire windows of the radiation shields. The contacts are made by connecting the gold pins glued into the plates (cf. Section 3.4). All connections then pass to the microscope via the middle stage of the damping system, i.e. the cylindrical sapphire plate, which also contains gold pins.

The middle stage plate contains an anodized aluminum tube with two compartments machined into it (see Figure 3.3), through which the tunneling current cable and the z-signal of the scan piezo tube are passed. Then, the two cables enter directly the STM head beneath. The I_t cable is further shielded by the inner electrode of the scan piezo tube. This electrode, as well as the aluminum tube are connected to the shield of the I_t coaxial cable. The cables to the x and y electrodes of the scan piezo tube descend outside the aluminum tube to the STM head.

The cables to the thermocouples, the filament, and the Si-diode coming from the middle stage are passed through some special cable holders on the base plate. From there they enter the base plate from below. The wires of the four point contact Si-diode are pairwise twisted together. The cables to the piezoceramic tubes are directly brought down from the middle stage to the top of the base plate.

Table 3.1 gives an overview over all the cable thicknesses and materials.

Flange - outer shield - inner shield:

Connection	Material	Diameter [mm]
TC Chromel-Alumel (2)	Chromel-Alumel TC wire (Omega Engineering Inc.)	0.2
TC W-Re (2)	W-Re TC wire (Omega Engineering Inc.)	0.254 (0.01")
Si diode (4)	polyimide isolated phosphor bronze (Lake Shore, Quad-Lead wire)	0.203 (AWG 32)
tunneling current (1)	home-made coaxial cable with Cu conductor	~1.4 outer ∅ 0.05 conductor
z-signal, sample bias (2)	flexible coaxial stainless steel (Lake Shore, Type SS)	1.0 outer ∅ 0.203 conductor
piezo electrodes (17)	PTFE insulated stainless steel braid wire (Advent Research Materials Ltd.)	7 x 0.05
tungsten filament (2)	stainless steel	1.00

Inner shield - middle stage - baseplate:

Connection	Material	Diameter [mm]
TC Chromel-Alumel (2)	Chromel-Alumel TC wire (Omega Engineering Inc.)	0.076
TC W-Re (2)	W-Re TC wire (Omega Engineering Inc.)	0.127
Si diode (4)	polyimide isolated phosphor bronze (Lake Shore, Quad-Lead wire)	0.203 (AWG 32)
tunneling current, z-signal (2)	teflon insulated Cu	0.05
piezo electrodes, sample bias (18)	insulated Ag-coated Cu wire (Isotec Kabel GmbH) teflon insulated Cu	0.127 0.05
tungsten filament (2)	silver coated copper braid wire (Drahtwerk Waidhaus GmbH)	~1.00

Table 3.1: Wire materials and diameters used for the electrical connections to the STM. The number of cables is indicated in brackets in the first column.

3.4 Cooling System and Thermal Stability

As discussed in Section 3.2 the VT-STM measurements must be performed at low temperature. Thermal stability is of great importance as the sample-tip distance should remain constant within 0.005 Å during one voltage scan. In this section I'm going to discuss the thermal heat fluxes, cooldown time, and thermal stability of our system.

3.4.1 System Description

In our setup the following thermal fluxes as indicated in Figure 3.7 occur.

Between chamber and outer radiation shield:

- cooling of the inner shield by the cryostat cold tip at 4 K (1)
- cooling of the outer shield by the helium exhaust gas (2)
- heating by heat conduction through the cables (3) and the pull-down mechanism (4) connected to the chamber at room temperature
- heating by room temperature irradiation from the chamber (5)

Between outer and inner radiation shield:

- heating of the inner shield by heat conduction through cables (6) and pull-down mechanism (7) from outer shield
- heating of the inner shield by radiation from the outer shield (8)

Within inner shield:

- heat fluxes through all cables, the suspension springs, and the Cu braids mounted for this purpose (9) (in Figure 3.7 just two examples are shown)
- heat radiation between the different parts of the microscope inside the inner shield (10)

Other:

- outer shield or room temperature irradiation onto the sample through the dosing and evaporation holes (11)

For both shields the cooling power must exceed the heating power during cooldown, while at equilibrium the cooling power must equalize the heating power, i.e. the total cold loss.

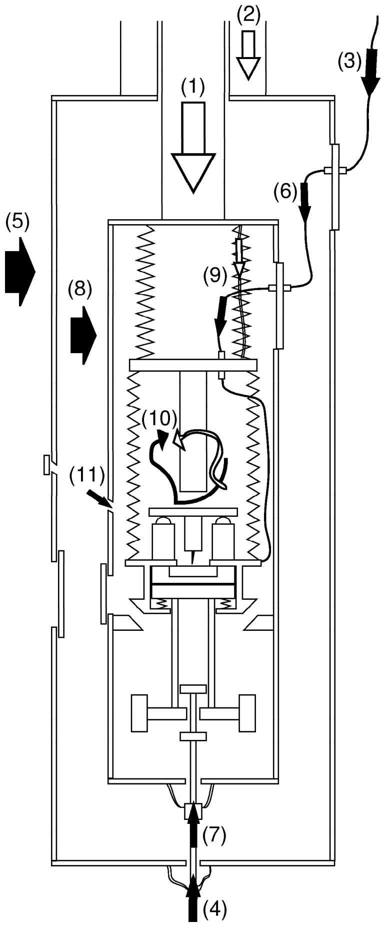

Figure 3.7: Schematics of the various heat fluxes in our STM system.

The heat exchange with the outer world is important in terms of liquid helium consumption and cooldown time. To minimize the total liquid helium consumption, the necessary cooling power to the inner shield is decisive. First, the total thermal mass of the microscope should be sufficiently small. A lower limit is however given by the minimal geometrical size of some STM parts (piezo tubes, electrical connections, etc.). Second, the cold losses of the inner shield have to be estimated and minimized taking into account the thermal connections with the outer shield and the vacuum chamber.

For this purpose all cables are heat sunk at the sapphire feedthrough windows in the outer and inner shield. Sapphire is an electric insulator with a high heat conduction at low temperatures [53, 54]. When gluing different pieces together, one has to pay attention to the thermal resistance of the contact area [54]. For our setup we always used special UHV compatible epoxy, which has a good thermal conduction at low temperature and a good mechanical stability (Epo-tex H27D, electrically conductive; Epo-tex H77, electrically insulating; Epoxy Technology). In addition to heat sinking all electrical and mechanical connections, we let gold plate the copper shields, which lowers the absorption of heat radiation.

The heat fluxes within the inner shield define the thermal stability of our microscope and are important for the cooling of the STM core parts. The stability is best when all parts of the STM are thermally well connected. When the heat sinking of the cables and the cooldown mechanism rod at the inner shield is efficient enough, no significant heat fluxes within the inner shield should occur after cooldown, unless the sample is heated or one of the dosing/evaporation holes is opened. In the latter case the baseplate with the sample has to be cooled down again or held at a certain temperature. Therefore good thermal conduction paths between the inner shield and the STM core parts must be built. This is why silver coated ETP copper braids connect the top of the inner shield with the upper stage and continue down to the baseplate (see Section 3.3). We established an additional thermal connection between the baseplate and the STM head. Braids lead from the baseplate to the Cu-Be balls within the outer three piezoceramic tubes. Finally, to reduce the effects of temperature variations on the tip-sample distance, the core part of the microscope could in principle be thermally compensated[2], which is not possible in our setup (see Section 3.3.2). In turn, we have direct sample access for temperature reading and heating.

3.4.2 Calculation of Heat Fluxes

In this section an estimation of the above identified heat fluxes is given.

The heat radiation power, i.e. the heat radiation absorbed per unit time by parts of our system, can be calculated according to the formula

$$\frac{\mathrm{d}Q}{\mathrm{d}t}_{rad} = \sigma \cdot \epsilon \cdot A \cdot (T_e^4 - T^4) \quad , \tag{3.3}$$

---

[2] Stipe et al. [47] presented a beetle type STM, where the scan piezo tube and the outer piezo tubes all show upwards. The thermal expansion of the scan tube carring a tungsten tip matches that of the outer tubes carring the tungsten balls. The sample in the sample holder with ramps is put onto the tungsten balls face downwards. This results in an almost constant tip-sample distance with respect to temperature variations.

where σ is the Stefan-Boltzmann constant, ϵ is the absorption (emission) coefficient, A is the area, T_e is the temperature of the environment, and T is the temperature of the absorbing body. Non-radiative heat flow between two points at different temperature is given by

$$\frac{\mathrm{d}Q}{\mathrm{d}t}_{non-rad} = -\lambda \cdot A \cdot \frac{\mathrm{d}T}{\mathrm{d}l} \quad , \tag{3.4}$$

where λ is the thermal conductivity, A is the cross sectional area of the connecting material, and $\mathrm{d}T/\mathrm{d}l$ is the temperature variation along the conduction path. For a small temperature difference ΔT and when λ does not vary significantly in the temperature range considered, this yields

$$\frac{\mathrm{d}Q}{\mathrm{d}t} = -\bar{\lambda} \cdot A \cdot \frac{\Delta T}{\Delta l} \quad , \tag{3.5}$$

where Δl is the length of the heat conduction path and $\bar{\lambda}$ is a mean value of the thermal conductivity. The quantity $\Delta l/\bar{\lambda}A$ is also called thermal resistance in analogy to the electrical resistance. In our case, for the heat conduction between the outer world and the STM and between the two shields, we cannot neclect the variation of λ in the respective temperature ranges. But for constant A we can calculate the transferred heat power $P = \mathrm{d}Q/\mathrm{d}t$ along the heat conduction path l from one end at T_2 to the other end at $T_1 < T_2$:

$$\begin{aligned} P \cdot \mathrm{d}l &= \lambda(T) \cdot A \cdot \mathrm{d}T && (3.6) \\ P &= \frac{A}{l} \cdot \int_{T_1}^{T_2} \lambda(T)\ \mathrm{d}T && (3.7) \end{aligned}$$

Defining the thermal integral

$$\tilde{\lambda} := \int_{T_{ref}}^{T} \lambda(T)'\ \mathrm{d}T' \quad , \tag{3.8}$$

where T_{ref} is an arbitrary reference temperature we can write

$$P = \frac{A}{l} \cdot \left[\tilde{\lambda}(T_2) - \tilde{\lambda}(T_1)\right] \quad . \tag{3.9}$$

Finally, for our application, we consider the case where we have a heat conduction path consisting of n pieces of the same material, each piece having its own sectional area A_i and length l_i. The temperatures at the ends of piece i are T_i and T_{i-1}. As the heat transferred per unit time is the same all along the path we have according to Equation 3.9:

$$\frac{l_i}{A_i} \cdot P = \left[\tilde{\lambda}(T_i) - \tilde{\lambda}(T_{i-1})\right] \tag{3.10}$$

Summation of all n equations leads to

$$P = \frac{\tilde{\lambda}(T_n) - \tilde{\lambda}(T_0)}{\sum_i \frac{l_i}{A_i}} \quad . \tag{3.11}$$

I now give an quantitative estimation of all heat fluxes indicated in Figure 3.7 on page 26. Due to the simplified calculations all values should indicate the order of magnitude. The temperature of the outer shield depends on the temperature of the helium exhaust gas and is not exactly known. It will be in the order of 70 K at equilibrium (cf. Section 3.4.3).

Cold losses due to heat radiation according to Equation 3.3 (see Figure 3.7):

- Outer shield (5) with dimensions of ⌀84 × 230 mm, $\epsilon = 0.02$ [55], $T_2 = 300$ K, $T_1 = 70$ K: 660 mW.
- Inner shield (8) with dimensions of ⌀49 × 169 mm, $\epsilon = 0.02$ [55], $T_2 = 70$ K, $T_1 = 4$ K: 1 mW.
- Sample (11), with open sliding doors of the dosing or evaporation hole, ⌀3 mm and ⌀1 mm, $\epsilon = 1$, $T_2 = 300$ K, $T_1 = 4$ K: 3.2 mW and 0.4 mW.

Cold losses due to heat conduction according to Equations 3.9 and 3.11. The thermal integrals were calculated based on the values for the thermal conductivity of stainless steel given in [56] and the cables specifications.

- Cables between chamber and outer shield (3). 30 cables of about 160 mm length (cf. Table 3.1 on page 24): 41 mW.
- Pulldown mechanism rod between chamber and outer shield (4) with dimensions of ⌀1.6 × 10 mm: 660 mW.
- Cables between outer and inner shield (6). 30 cables of about 160 mm length, see Table 3.1 on page 24: 4 mW.
- Pulldown mechanism rod between inner and outer shield (7) with dimensions of ⌀1.6 × 13.5 mm, ⌀2.5 × 6.5 mm: 3 mW.

For the outer shield the heating power transmitted by the cooldown mechanism and from irradiation is several hundreds of milliwatt and dominant over the conduction trough the cables. For the inner shield all cold losses are in the order of some milliwatt. This can now be compared to the maximal cooling power from the cold tip of the cryostat, which is 750 mW at 4.2 K as specified by the supplier. Hence, at equilibrium the maximal cooling power exceeds the cold losses significantly. At equilibrium the cooling power equals the heating power and we can estimate the temperature difference between the top and the bottom of the inner shield using Equation 3.9. The thickness of the copper tube is 1.5 mm, that of the lids 2.5 mm. We only consider the heat conduction through the cylinder. The thermal integrals are calculated based on the values for the thermal conductivity of ETP copper given in [56][3]. The resulting temperature difference between top and bottom of the inner shield cylinder is about 0.02 K. We conclude that in our system the heat conduction within the inner shield parts is largely sufficient. The critical point is therefore the thermal resistance at the contact surfaces between the cold tip of the cryostat and the inner shield top plate, and the inner shield top and bottom plates and the cylinder. Between metals the actual contact area can be several orders of magnitude lower due to microscopic irregularities of the opposing surfaces [54]. To improve thermal conductance indium sheets were layed between all important contact surfaces. The very soft indium metal adapts itself much better to rough surfaces under pressure and thus increases the effective contact area.

3.4.3 Cooldown Time and Helium Consumption

The time for cooling down our system is determined by

$$P_c(T) = \frac{\mathrm{d}Q}{\mathrm{d}t} + P_h(T) \quad \text{and} \quad \mathrm{d}Q = \left[\sum_i C_{M,i}(T)M_i\right] \mathrm{d}T \ , \tag{3.12}$$

where P_c is the cooling power and P_h the heating power (the cold losses), Q is the transferred heat, $C_{M,i}$ is the specific heat capacity and M_i the mass of the body i, and T is the temperature. This yields

$$t = \sum_i M_i \int\limits_{T_1}^{T_2} \frac{C_{M,i}(T)}{P_c(T) - P_h(T)} \, \mathrm{d}T \ . \tag{3.13}$$

---

[3] Note that the thermal conductivity at low temperatures of any metal and in particular of copper depends on its purity and the number of defects and can change by some orders of magnitude for different types of the same material [53].

The most important thermal mass are the radiation shields made of ETP copper. Above 50 K neither the maximal cryostat cooling power to the inner shield nor that to the outer shield is known. Anyway, the real cooling power is limited by the highest thermal resistance between the cold tip and the STM core parts, which are the contact surfaces. The cold losses, as discussed in the previous section, strongly depend on the temperatures of the inner and outer shield.

Cooling tests in the laboratory were made before complete STM setup, with only the two radiation shields mounted onto the cryostat. The purpose was to verify that the thermal mass would be low enough and to gain information about the thermal contacts, first, between the cold tip and the inner shield and, second, between the various parts of the shields. We could cool down the inner shield to 5 K in roughly 2 hours. The temperature of the outer shield was about 90 K after 2 hours and dropped subsequently to about 65 K.

We can calculate the liquid He consumption using the He evaporation energy of 2.6 kJ/l [53]. Cooling down the inner shield with $M \approx 460$ g from 80 K to 4 K, after precooling with liquid nitrogen, theoretically needs 0.7 l of liquid He. However, neither losses nor the cooling of the He transfer line are considered in this calculation. The real helium consumption during cooldown turned out to be several liters.

At 4 K the typical liquid He consumption of our cryostat is about 1.5 l/h. With a dewar of 25 l of liquid helium we can therefore cool our setup for at least 2 days of 5 hours of measurement each.

3.5 Vibration Isolation

As outlined in Section 3.2, inelastic electron tunneling spectroscopy measurements (STM-IETS) require a tip-sample distance with a stability of about 0.005 Å in the frequency range of interest. Therefore, on the one hand, the tunneling assembly must be well protected against external vibrations, which could show up in the tunneling current. Building vibrations, which occur typically from 1 Hz to 100 Hz, and vibrations of laboratory equipment should not be transferred to the STM base plate. We note that these external vibrations can also cause a movement of the whole baseplate, i.e. a simultaneous movement of the tip and the sample surface, during which the tip-sample distance remains unchanged.

For good protection from external vibrations we made a double stage spring suspension system with very low eigenfrequencies. Details are discussed in the following section.

Besides external vibrations, the tunneling assembly is subject to an internal vibrational excitation: the periodic correction of the tip height by the electronic feedback loop, which takes place at frequencies of several hundred or thousand hertz. Thus the assembly should preferably not have eigenfrequencies in this frequency range. We pushed the eigenresonances of our tunneling assembly beyond about 10 kHz by making it very stiff.

3.5.1 Two-Stage Spring Suspension System

Theory

The problem of vibration isolation is to find a proper mounting of a mass such that its displacement or vibrational response amplitude upon an external vibrational excitation amplitude is minimal.

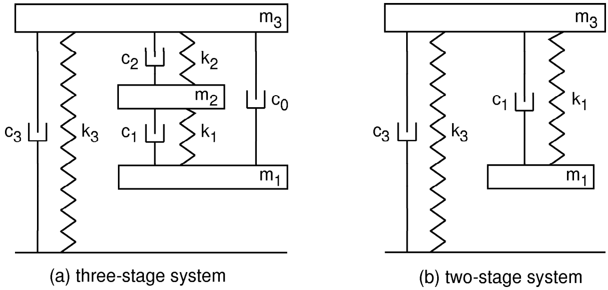

(a) three-stage system (b) two-stage system

Figure 3.8: Schematics of a three-stage (a) and a two-stage (b) vibration isolation system. The masses are connected to each other by harmonic springs and dampers.

In our case the mass is the STM base plate and the external vibrations are, on the one hand, mechanical vibrations transmitted through the laboratory floor and, on the other hand but to a smaller extent, acoustic noise from the surroundings. In Figure 3.8 (a) a schema of our system is given. The base plate m_1 is attached on an upper plate m_2 by three suspension springs and the upper plate hangs on the top of the inner shield also by means of three suspension springs. The inner shield is fixed to the liquid He flux cryostat and therefore to the chamber, which stands on four pneumatic dampers. We describe the overall setup by a three-stage damping system, composed of two-stage spring suspension (k_1, k_2) and one-stage pneumatic (k_3) damping. Newton's equations for this setup read:

$$
\begin{aligned}
m_1\ddot{x}_1 + c_1(\dot{x}_1 - \dot{x}_2) + k_1(x_1 - x_2) + c_0(\dot{x}_1 - \dot{x}_3) &= 0 \\
m_2\ddot{x}_2 + c_2(\dot{x}_2 - \dot{x}_3) + k_2(x_2 - x_3) + c_1(\dot{x}_2 - \dot{x}_1) + k_1(x_2 - x_1) &= 0 \\
m_3\ddot{x}_3 + c_3(\dot{x}_3 - \dot{X}) + k_3(x_3 - X) + c_2(\dot{x}_3 - \dot{x}_2) + k_2(x_3 - x_2) &= 0
\end{aligned}
\tag{3.14}
$$

Assuming a sinusoidal external excitation $X = X_0 \exp(i\omega t)$ we have for small damping constants c_n $(n = 0, 1, 2, 3)$ approximately $x_n = x_{n,0} \exp(i\omega t)$ $(n = 1, 2, 3)$. We are interested in the ratio of the response amplitude $x_{1,0}$ to the excitation amplitude X_0. It is convenient to use the transfer function defined as

$$T = 20 \log_{10} \left| \frac{x_{1,0}}{X_0} \right| \tag{3.15}$$

in units of dezibel [36, 57]. In Figure 3.9 the transfer function is plotted (red and green lines) for a system with masses and spring constants similar to those of our setup. Our three-stage system can be compared to a two-stage system (black lines) composed of a one-stage spring suspension damping, with a mass $m = m_1 + m_2$ and a length $l \approx l_1 + l_2$, and a one-stage pneumatic damping, as illustrated in Figure 3.8 (b).

We can compare the slope of the undamped curves at frequencies beyond the resonances. For a single-stage system the slope is -40 dB/Decade, which corresponds to a decrease of the response amplitude of two orders of magnitude upon one order of magnitude increase in frequency. For a multiple-stage system, at frequencies much higher than the resonance frequencies, the transfer function equals the sum of the single transfer functions, which leads a slope of -80 dB/Decade for a two-stage system and -120 dB/Decade for a three-stage system. This steeper slope results in a much better vibration isolation over the important frequency range 1–10 kHz. For damped systems, the amplitudes at the resonances are flattened out but the slope is less steep at higher frequencies. One has to find a good compromise between vibration isolation at higher frequencies and the suppression of the resonance frequencies.

Calculations show that for a two-stage spring suspension system with damping constants c_1 and c_2 a damping only at stage 1 (cf. Figure 3.8) is best for the overall transfer function [57]. In fact, damping the relative movement of the base plate 1 with respect to the upper stage 2 seems to be a good solution for our case as can be seen from Figure 3.8, where the green curves are the three-stage transfer function plotted for two different values of the damping constant c_1. However, in our setup it is difficult to incorporate a well-defined damper c_1 because of space restrictions and the cabling. As an alternative, we decided to use eddy-current damping magnets glued to

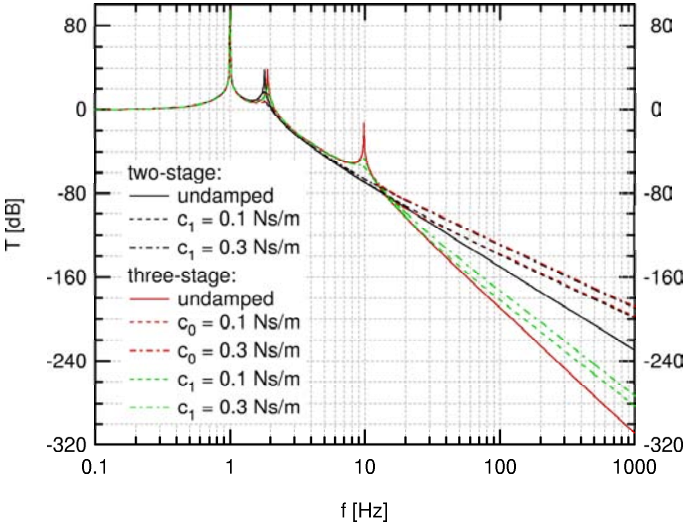

Figure 3.9: Transfer function for a three-stage (red and green lines) and a two-stage (black lines) vibration isolation system as sketched in Figure 3.8. The transfer function T is defined as $T = 20 \log_{10} \left| \frac{x_{1,0}}{X_0} \right|$, where $x_{1,0}$ is the response and X_0 the excitation amplitude. Masses and spring constants: three-stage system: $m_1 = 20$ g, $k_1 = 45$ N/m, $m_2 = 120$ g, $k_2 = 29$ N/m, $m_3 = 3 \cdot 10^3$ kg, $k_3 = 1.18 \cdot 10^5$ N/m. Two-stage system: $m_1 = 140$ g, $k_1 = 18$ N/m, $m_3 = 3 \cdot 10^3$ kg, $k_3 = 1.18 \cdot 10^5$ N/m. The damping constant c_1 refers to a damping between stage 1 and the adjacent stage whereas c_0 represents a damping between stage 1 and stage 3 in the three-stage system.

a mechanical piece attached to the base plate from below (cf. Figure 3.2 on page 17). That way the magnets are also placed far from the cables to the STM. This kind of damping corresponds to a damping constant c_0 as shown in Figure 3.8. Owing to the direct coupling between stages 1 and 3 the transfer function is highly affected by $c_0 > 0$. If damping values for c_0 in the three-stage system are equal to those for c_1 in the two-stage system, the two transmission curves become quasi identical at higher frequencies, as seen from the dashed and dash-dotted red and black curves in Figure 3.8.

However, for our setup the three-stage system has still some advantages over the two-stage system. Vibration transmission through wires can be reduced by clamping the wires on the intermediate stage. The intermediate stage also holds the aluminum tube which shields the tunneling current and the z-signal and serves as a cold plate for cable heat sinking. Nonetheless, the construction of the three-stage system should be reconsidered for future setups due to its more complicated nature.

At 1 kHz the transfer function takes a value of $\lesssim -180$ dB for a damping constant $c_0 \lesssim 0.3$ Ns/m. Mechanical vibration noise is therefore reduced by a factor of 9. An excitation amplitude of 0.01 mm would result in a response amplitude of 10^{-4}–10^{-7} Å in the 1–10 kHz frequency range, which is sufficient for spectroscopic STM measurements.

Realization

In this section I describe the experimental realization of the double-stage vibration damping system concerning masses and spring material and dimensions. These parameters must be optimized within the technical limits of the experimental setup. The eddy-current damping, which hardly affects the resonance frequencies, is discussed in the next section.

The following restrictions are present in our setup:

- The overall length $\sim l_1 + l_2$ of the double-stage system is limited by the length of the inner shield.
- The second stage mass m_2 (base plate) is more or less given since the whole setup should be as compact as possible and the overall thermal mass minimized.
- The first stage mass m_1 must not be too big for the same reasons.
- The diameters of the springs d_1, d_2 are limited because the springs must not touch the inner shield.
- The maximum yield strength of the springs must not be exceeded.
- The spring material should not deform during bakeout.
- The springs (under tension of the mass) must not significantly change their length at low temperatures.

The last two points address only the question of spring material. We chose Inconel X-750 (California Fine Wire), which has been used successfully by another research group [47].

To determine the optimal wire diameter and spring dimensions, the following points have to be considered:

- The two eigenresonances of the double-stage system appear at frequencies in the range of the eigenresonances of the corresponding single stages (m_1,k_1 and m_2,k_2). The eigenfrequency of the single-stage system is given by

  $$f = \frac{1}{2\pi}\sqrt{\frac{k}{m}} = \frac{1}{2\pi}\sqrt{\frac{g}{\Delta l}} \quad , \tag{3.16}$$

  where m is the mass, $k = mg/\Delta l$ is the spring constant, Δl is the spring length variation, and g is the gravitational acceleration. The eigenfrequencies can obviously be lowered by increasing the masses and/or decreasing the spring constants. Furthermore, the closer to each other the two resonances of the single stages are, the closer are also the two resonances of the overall setup.

- The relation between the axial load $F = mg$ (m: mass, g: gravitational acceleration) and the deflection Δl of a spring with coil diameter D, number of coils n, and wire diameter d is [36]

  $$F = \frac{Gd^4}{8nD^3}\Delta l = k\Delta l \quad , \tag{3.17}$$

  where G is the shear modulus of elasticity of the wire (about 75.8 GPa for our Inconel X-750 wire as specified by the supplier) and k the spring constant.

- The maximum shear stress or yield strength (about 724 MPa for our wire) is [36]

  $$\tau_{max} = \frac{8D}{\pi d^3}\Delta l \quad . \tag{3.18}$$

The goal is to make the two ratios k_1/m_1 and k_2/m_2 [58] as small as possible and not too different from each other. The weight of the upper stage m_1 is much smaller than m_2 and as a consequence k_1 should be smaller than k_2. But at the same time the upper springs carry the total weight $m_1 + m_2$. As a result it is sufficent to test the maximum shear stress condition given in Equation 3.18 for the upper spring stage. According to Equation 3.17, we can vary d_1 and D_1 and obtain the same k_1 as long as $d_1^4/D_1^3 = constant$. From Equation 3.18 we see that the best of these solutions in terms of shear stress is obtained for a maximal spring diameter D_1. In fact, in our setup the shear stress of Inconel X-750 would be exceeded for too small values of d_1 and D_1. Then we can calculate the minimal wire diameter d_1 from Equation 3.18.

The other dimensions were then determined by considering the theoretical transmission curves for different values of d_2, D_2 and l_1, l_2. It turned out to be best if D_2 is also maximized. Increasing the weight of the upper stage m_1 or decreasing D_2 in order to approach the two ratios k_1/m_1 and k_2/m_2 does not give better results.

Eddy-Current Damping

As can be seen from Figure 3.9 on page 34, for our setup a damping constant of a few tenths of Ns/m seems reasonable. The damping is achieved by means of three cylindrical samarium cobalt magnets (Recoma 28, Magnequench, Inc.) rigidly connected to the base plate (Figure 3.2 on page 17). When the base plate is vibrationally excited, the moving magnets induce eddy currents in the copper shield in front of them, which decelerates the base plate movement. The eddy-current damping constant C for a magnetic damper consisting of a circular magnetic flux facing a rectangular metal sheet is given by [57, 59]:

$$C = C_0 \frac{B^2 t \pi a^2}{\rho} \quad , \tag{3.19}$$

where B is the magnetic flux with a circular cross section of radius a, t is the thickness and ρ the electrical resistivity of the metal, and C_0 is a constant depending on the dimensions of the rectangular conductor with respect to a.

In our case the diameter of a magnet is 5 mm and the magnetic field at the copper shield is about 0.018 T as measured with a Hall effect magnetometer. The constant C_0 can be taken as 0.5 [57, 59] and the electrical resistivity is $\rho \approx 0.002 \cdot 10^{-8}\,\Omega\text{m}$ at 4–8 K copper shield temperature. This results in an overall damping constant of about 0.7 Ns/m at 4–8 K. However, for higher temperatures the damping force drops significantly due to the higher electrical resistivity of copper.

3.5.2 Eigenresonances of the Beetle Type STM

Theory

The principal theoretical eigenfrequencies of a beetle type microscope are related to periodic movements of the microscope head with respect to the base plate as well as to the movement of the scan piezo tube.

The mass of the outer three tubes can be neglected with respect to the mass of the scan head with the scan piezo tube attached to it. In this case the whole microscope can be treated as a three dimensional harmonic

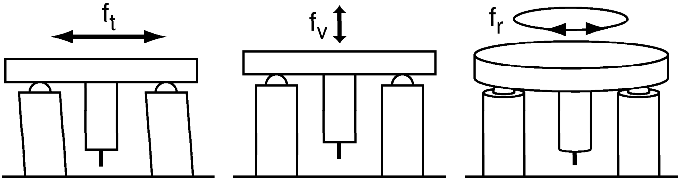

Figure 3.10: Principal eigenresonance modes of a beetle-type STM.

oscillator with the three outer tubes acting as spring and the scan head as mass. The main intrinsic eigenresonances can be thought of as horizontal translation, vertical translation, and rotation around the symmetry axis of the scan head with respect to the base plate as indicated in Figure 3.10. The spring constants for a tube of length L, outer diameter D, inner diameter d, and elastic modulus Y are [60–62]:

$$\text{transversal mode:} \quad k_t = \frac{3\pi}{64} Y \frac{D^4 - d^4}{L^3} \tag{3.20}$$

$$\text{vertical mode:} \quad k_v = \frac{\pi}{4} Y \frac{D^2 - d^2}{L} \tag{3.21}$$

From this the corresponding resonance frequencies for the microscope head carried by three tubes are calculated:

$$f_t = \frac{1}{2\pi}\sqrt{\frac{3k_t}{M}} \quad \text{and} \quad f_v = \frac{1}{2\pi}\sqrt{\frac{3k_v}{M}} \quad , \tag{3.22}$$

where M is the mass of the scan head. The rotational frequency is found in analogy, using the torsional spring constant $D_t = k_t r^2$, where r is the distance of the piezo tube centers from the center of the sapphire disk, and J the moment of inertia of the disk [61]:

$$f_r = \frac{1}{2\pi}\sqrt{\frac{3D_t}{J}} \tag{3.23}$$

The outer tube dimensions in the present setup are $D = 6.35\,\text{mm}$, $d = 5.334\,\text{mm}$, $L = 10\,\text{mm}$ (see also Section 3.3.2 on page 20), and $Y = 8.1 \cdot 10^{10}\,\text{N/m}^2$. For the scan head in the final setup we have $M = 8.2\,\text{g}$, $J_t \approx 715\,\text{g}\,\text{mm}^2$, and $r = 9\,\text{mm}$. This results in $f_t = 9.5\,\text{kHz}$, $f_v = 26.5\,\text{kHz}$, and $f_r = 9.2\,\text{kHz}$.

For the bending mode of the scan piezo tube the following formula applies [60]:

$$f_{scanpiezo} = \frac{1}{2\pi}\sqrt{\frac{\pi}{64} Y \frac{D^4 - d^4}{L^3} \frac{3 \cdot 3.515^2}{3m + 3.515^2 M}} \tag{3.24}$$

with tube mass m and attached mass M. With the scan tube dimensions $D = 4.318\,\mathrm{mm}$, $d = 3.302\,\mathrm{mm}$, $L = 10\,\mathrm{mm}$, the density of the piezoceramic material of $7.5\,\mathrm{g/cm^3}$, and $M = 0.064\,\mathrm{g}$, we find $f_{scanpiezo} = 20\,\mathrm{kHz}$. This is far beyond the critical range of 1–10 kHz. I note that the vertical mode of the scan tube occurs at an even higher frequency and is thus not considered.

Measurements

Due to the simplifications made, the calculated frequencies just give an estimate of the resonance frequencies we have to expect. To find the real resonance frequencies I excited the scan piezo tube with a sinusoidal voltage and measured the response voltage at electrodes of the outer tubes [63].

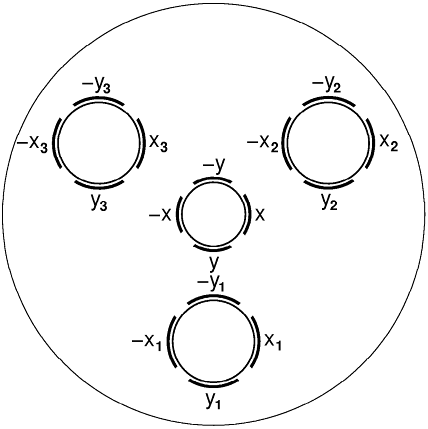

Figure 3.11: Arrangement of the piezoceramic tubes with their x, y electrodes.

The top view of the piezo tubes and electrodes arrangement is sketched in Figure 3.11. The voltage measurements were performed with a lock-in amplifier, using the internal oscillator of the instrument as signal source. The excitation amplitude was typically 220 mV. If it is set too high, the

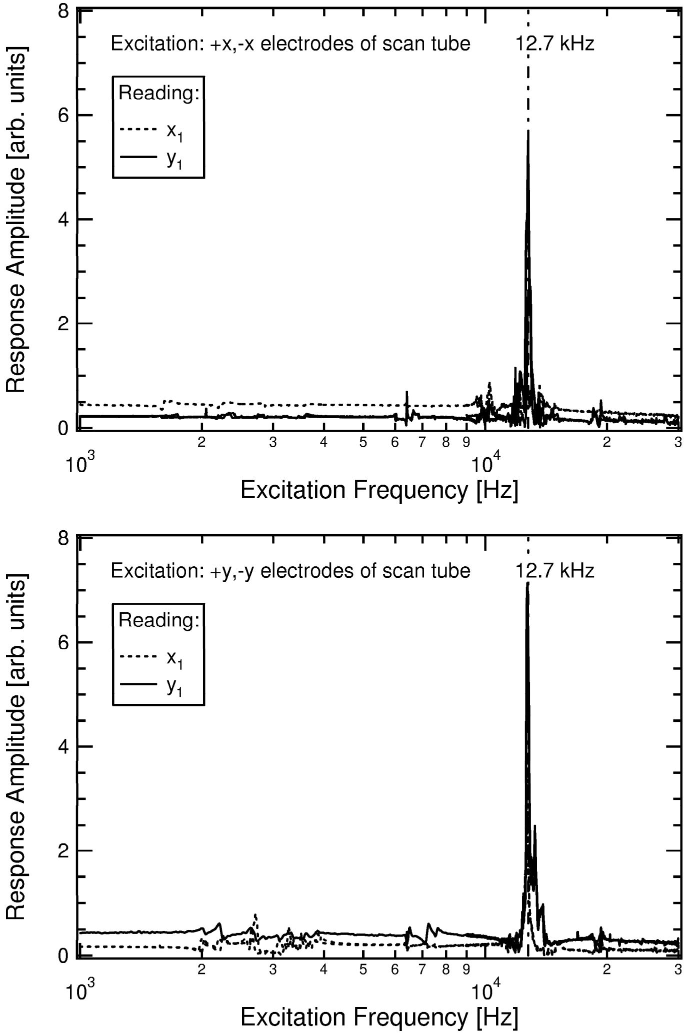

Figure 3.12: Response signals at electrodes of outer piezoceramic tubes upon sinusoïdal excitation of scan piezo tube.

sapphire ramp starts to slip with respect to the Cu-Be semi-balls, inhibiting the detection of resonances. The measurements were performed over the range of 1–30 kHz. Below this range the measured voltage would have to be corrected for the effect of the finite entrance impedance of the lock-in amplifier (see reference measurement for an isolated tube in Appendix B).

Figure 3.12 depicts the results for excitation of the scan piezo tube in the final setup. I applied opposite voltage signals to two opposite electrodes of the scan piezo and measured the response signals at x_1 and y_1. The top panel shows the results for the excitation of $-x$, x. The two solid lines correspond to different positions of the sapphire ramps with respect to the Cu-Be half spheres. A single pronounced peak at 12.7 ± 0.1 kHz is visible in the spectra, for both curves x_1 and y_1. The same peak shows up when exciting $-y$ and y as shown in the bottom panel and the peak does not depend on the ramp position. It can therefore be attributed to an eigenmode of the microscope. The peaks in the range of 2–10 kHz depend on the sapphire ramp position and might be so-called rattling resonances [61]. However, with respect to the microscope resonance peak, these peaks are considerably lower than measured in other setups [48, 64], possibly owing to different ramp and ball materials. In our case the sapphire ramps are harder than the Cu-Be balls, in contrast to other setups, where a metal ramp resides on sapphire balls [48, 64]. This might reduce rattling resonances that originate from microscopic irregularities of the ramp surface.

Figure 3.13 summarizes the identified resonances for four different scan head masses during STM construction, including the final one. The detected resonance frequencies do not vary according to a simple $f \propto 1/\sqrt{M}$ law. Moreover, the measured resonances appear at higher frequency values than theoretically predicted and they also depend on the geometry (mass distribution) of the microscope. A possible explanation for this behaviour could be that the measured mode does not represent a real transversal or rotational mode but rather some more complicated movement, where the geometry of the scan head also plays a role.

I further investigated the resonance modes for the scan head masses of 6.9 g and 8.4 g by measuring the response amplitude and phase of each of the electrodes of all the outer tubes. From this the kind of movement of each tube and consequently of the microscope as a whole can be inferred. I came to the conclusion that all detected modes correspond to a transversal-like movement of the scan head. The direction of this oscillation is in all cases rotated by about 45° with respect to the direction of excitation in the x-y plane. The obvious preference for one specific oscillatory direction is probably due to imperfections in symmetry of the setup (orientation of the tubes, slightly different wall thicknesses at electrodes, etc.).

The vertical mode with a theoretical value of $f_v = 26.5$ kHz never appears in the spectra, even when the z-electrode of the scan piezo tube or the z-electrodes of the outer tubes are excited. Excitation of z-electrodes

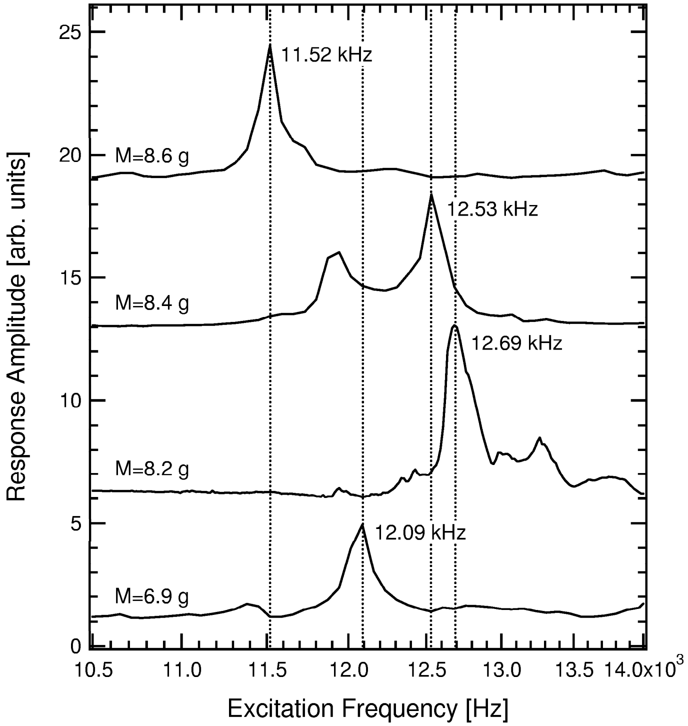

Figure 3.13: Resonance peaks for different scan heads. M denotes the scan head mass. The peak shifts are not compatible with a simple $f \propto 1/\sqrt{M}$ relation.

usually results in flat spectra without any pronounced peaks.

To sum up, I found only one pronounced resonance peak in the final STM setup, corresponding most probably to a kind of transversal-like mode. The resonance frequency lies beyond the critical range of 1–10 kHz and does thus not disturb the tunneling current measurements. Rattling resonances also appear, but they are weak with respect to the microscope eigenresonances. Finally, the sinusoïdal vertical movement of the scan piezo does not excite any microscope vibrational modes over the 1–30 kHz range.

3.6 Coarse Approach by a Stick-Slip Mechanism

The coarse approach is one of the critical points of an STM. In this section the coarse approach behaviour of our final setup is discussed. In this context I also mention some difficulties which arose during the mounting and test periods of the STM.

Our new STM is of the Besocke type [65, 66]. Cu-Be balls glued onto the three outer piezoceramic tubes are in contact with three sapphire ramps on the STM head (Figure 3.5 on page 20). The coarse approach occurs through stick-slip motion. A sawtooth-like signal is applied to the outer piezo tubes. During a slow bending of the tubes the semi-balls carry the STM head into a certain direction (stick). This movement is followed by a quick jerk of the tubes into the opposite direction during which the STM head remains motionless at its new location due to its inertia and therefore the semi-spheres slip on the surface of the STM head. By means of consecutive stick-slip steps the STM head can be moved in a well-defined manner. However, ideal stick-slip movements are difficult to achieve. A detailed investigation of stick-slip actuators can be found in [67]. Here we focus our attention on the most important issues.

The stick-slip movement crucially depends on the friction between ramp and ball. As the friction forces change with humidity and temperature and consequently a stick-slip mechanism working under ambient conditions does not necessarily work as well in UHV and at low temperatures.

The slip movement can only take place if the static friction force is overcome by the acceleration of the balls with respect to the ramps. This leads to the following condition for linear movements parallel to the STM head:

$$m\ddot{x} \geq \mu F_N \quad \Rightarrow \quad \ddot{x} \geq \frac{\mu F_N}{m} = \frac{\mu\, mg}{m} = \mu\, g \quad , \tag{3.25}$$

where $\ddot{x}$ is the acceleration of the balls with respect to the ramps, μ is the static friction coefficient, m is the scan head mass, and F_N is the normal force. The normal force is in our case simply one third of the scan head weight. The condition must be fulfilled at the point where the tubes start to jerk back, i.e. at the beginning of the slip movement. For a circular movement of the scan head, which is used for approaching and retracting the tip, a similar expression is found:

$$J\ddot{\varphi} \geq \mu F_N r \quad \Rightarrow \quad a = \ddot{\varphi} r \geq \mu g \frac{mr^2}{J} \quad , \tag{3.26}$$

where $\ddot{\varphi}$ is the angular acceleration of the balls with respect to the ramps and J is the moment of inertia. A higher moment of inertia facilitates the slip for rotational movements.

According to the equations above the important parameters for the stick-slip motion are the following:

- scan head mass and moment of inertia
- material and roughness of the ramps and of the semi-balls
- voltage signal applied to the outer piezo tubes, which determines a

Our scan head ramps are made of sapphire and the three semi-balls of copper-beryllium. One advantage of this choice is that the sapphire ramps do not wear due to their hardness. The stick-slip behaviour should thus remain reliable and reproducible with time. The static friction coefficient for copper-beryllium on polished sapphire is estimated to be smaller than 0.1. This leads to a theoretical minimal acceleration a of about 1 $\mathrm{m/s^2}$ (worst case). By measuring the voltage signal applied to the electrodes of the piezoceramic tubes and considering the piezoelectric coefficient, I find that the actual acceleration of the balls is about 6 $\mathrm{m/s^2}$. This turned out to be sufficiently high for the slip motion in the experiment. Nevertheless the value is rather low as compared to the theoretically required minimum.

I investigated the stick-slip behaviour of our setup. Assuming an ideal stick-slip movement the distance s by which the ramp moves in a time t is given by

$$s = d_{31} A f t \quad , \tag{3.27}$$

where d_{31} is the piezoelectric coefficient, and A and f are the amplitude and frequency of the voltage signal sent to the electrodes. This yields the following relations for a constant distance s:

$$t \propto \frac{1}{Af} \quad \Rightarrow \quad \ln t \propto -(\ln A + \ln f) \tag{3.28}$$

Figure 3.14 shows stick-slip measurements in air for an intermediate setup. It depicts the time versus frequency for turning the STM head over a distance of 2 mm into the sample approach direction for two constant ramp signal amplitudes. The experimental data is shown together with the theoretical lines for an ideal stick-slip movement. I find values that correspond well to theory.

In Figure 3.15 the time against amplitude for constant frequency is plotted, now for the final setup and both approach and retract direction, denoted as T_A and T_R, respectively. For the approach direction the data lie on the theoretical line at low amplitudes and deviate from it at higher amplitudes.

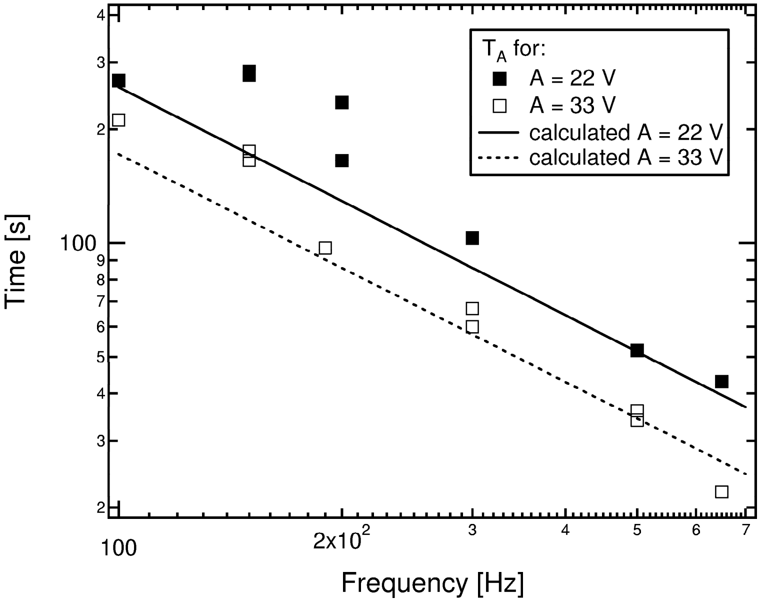

Figure 3.14: Stick-slip time versus step frequency for coarse approach at constant ramp signal amplitude A in air.

At amplitudes higher than 40–50 V the STM disk turns faster than theoretically predicted. For very high amplitudes we even observe a completely uncontrolled behaviour, where the behaviour of the disk resembles that of ice-skating. The contrary holds for retraction, where the system behaves ideally at higher amplitudes, but moves slowlier than predicted at amplitudes below 40 V. Hence, an amplitude close to 40 V works best for approach and retraction.

The difference between retraction and approach behaviour can be explained by the geometry of the setup. As can be seen from Figure 3.17, in case of approach the balls move away from the ramps during the slip. At high amplitudes the effect is more pronounced. The disk moves not only during the stick but continues to move into the same direction during the slip as it cannot be decelerated instantly at the end of the stick movement. Hence the disk turns faster than in theory. On the other hand, when retracting, the balls move "into" the ramps. As a result the friction force to overcome is higher and at low amplitudes the acceleration of the balls might become too small. The disk is then pushed a little backwards at each slip

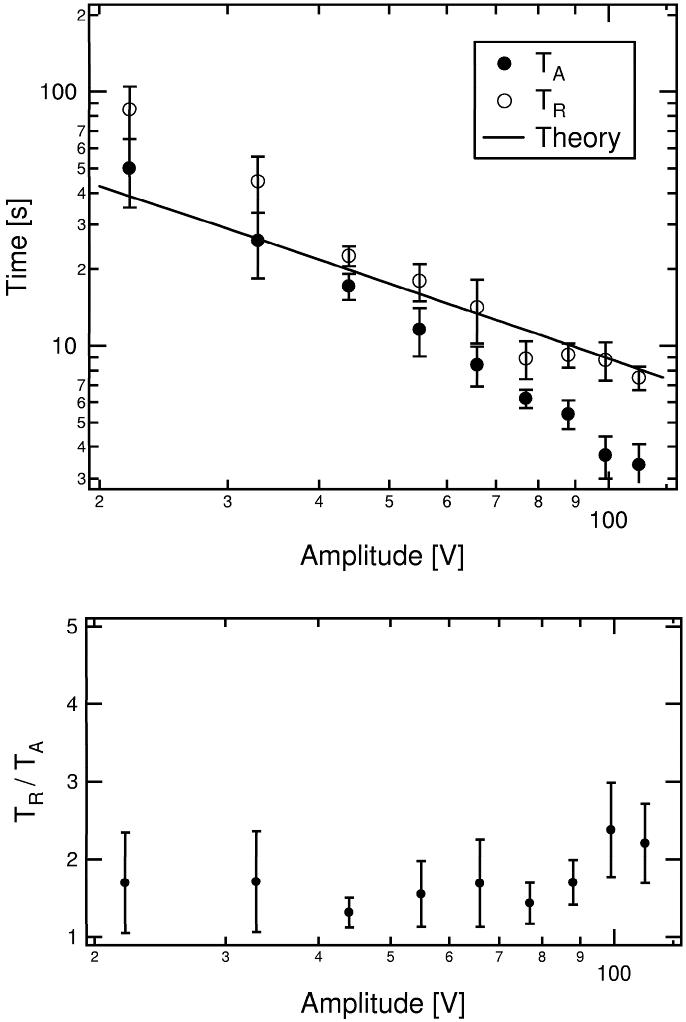

Figure 3.15: Stick-slip time versus ramp signal amplitude for coarse approach (filled symbols) and retraction (open symbols) at constant step frequency of 866 Hz in air.

and turns slowlier.

I measured the time versus amplitude also in UHV after bakeout. When

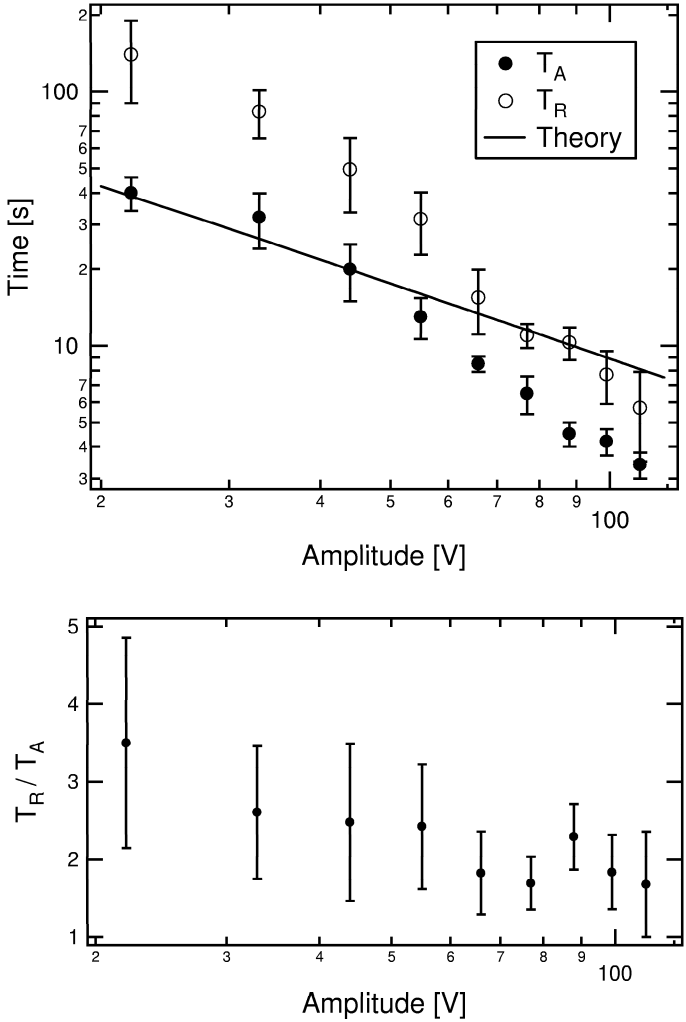

Figure 3.16: Stick-slip time versus ramp signal amplitude for coarse approach (filled symbols) and retraction (open symbols) at constant step frequency of 866 Hz in UHV after bakeout.

approaching, the results were the same as in air, i.e. at amplitudes higher than about 50 V the ramps move faster than predicted, as shown in Fig-

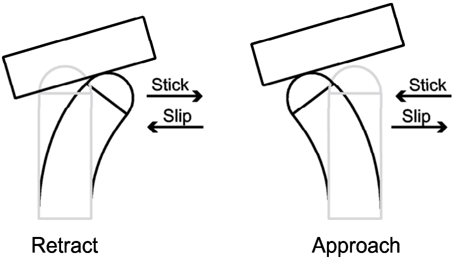

Figure 3.17: Basics of stick-slip motion.

ure 3.16. When retracting, the STM head turns again slowly at low amplitudes, but the effect starts already at amplitudes as high as about 60 V. Looking at Figures 3.15 and 3.16 the difference in the onset of the deviation from the theoretical line is clearly visible. It can be explained by assuming that the friction force increases under UHV conditions (after bakeout) such that higher amplitudes are needed for an ideal slip motion. The reason is most probably the lack of a waterlayer acting as lubricant between balls and ramps in UHV.

3.7 Tests on Graphite

To test our STM we imaged a highly oriented pyrolytic graphite (HOPG) surface in air. Figure 3.18 shows a 35×35 Å STM image of HOPG recorded with the new STM. We note that during the measurement the STM was hanging from a mechanically unstable support standing on a normal table in our laboratory. The x and z distances are indicated as calculated from the applied piezo voltage according to Equations 3.1 and 3.2 on page 21. The resulting distance of about 2.6 Å between adjacent peaks in the image agrees reasonably well with the in-plane lattice constant of 2.46 Å of graphite. The observed height variation is roughly 0.5 Å, wich is in the order of magnitude of the graphite LDOS corrugation [69]. Note that the LDOS corrugation of HOPG graphite at the Fermi level is about 0.8 Å while the one of the total charge density amounts only to 0.2 Å [69]. According to Figure 3.18 the z-noise is estimated to be $\lesssim 0.05$ Å for frequencies of 5 Hz–10 kHz, inducing intra-line noise, and about 0.2 Å for frequencies < 5 Hz, corresponding to height variations expanding over several linescans.

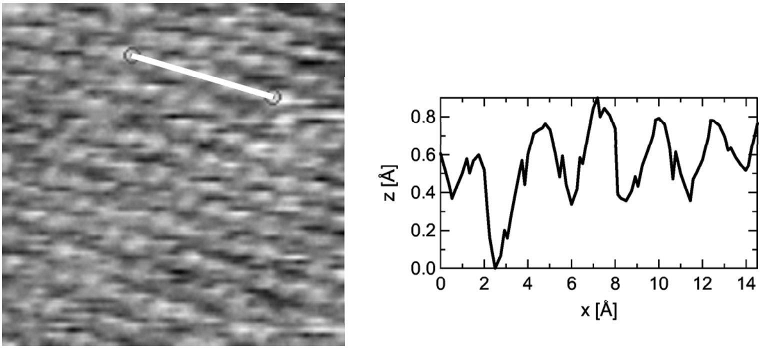

Figure 3.18: 37 × 37 Å STM image of HOPG graphite in air taken with the new STM hanging from a mechanically unstable support standing on a normal table in our laboratory. $I_t = 1$ nA, $V_t = -40$ mV. Image treatment included line per line mean value subtraction, plane subtraction, and y-direction scaling [68], but no frequency filtering.

3.8 Conclusions and Suggestions

The following list reviews the current state of the STM setup:

- The STM in its present state has been shown to work when operated in air, permitting atomic resolution on HOPG graphite. The tunneling current has proved to be quite stable with a z-signal noise below 0.2 Å (0.05 Å intra-line) when working with the mechanically unstable test mount. A significantly reduced current noise can be expected for the planned UHV measurements owing to the improved vibration isolation (pneumatic dampers and eddy-current damping) and the low measurement temperatures. Single-molecule vibrational spectroscopy should therefore be feasible.

- The eigenresonances of the tunneling assembly all lie beyond 10 kHz, thus not interfering with the tunneling feedback.

- The outer and inner radiation shields could be cooled down within 2 hours with a temperature reading of 5 K at the inner shield. However, a cooldown and thermal stability test for the completely mounted microscope remains to be made.

- The stick-slip mechanism with sapphire ramps and Cu-Be balls works satisfyingly, after several modifications.

During the STM setup and test phases a couple of problems and disadvantages of our STM were identified, which could not all be addressed immediately. Major points are:

- At present the position of the STM coarse approach ramps cannot be observed from outside. Hence, there is a risk of hitting the STM tip with the sample holder during sample transfer. At long-term a solution to this problem has to be found.
- The original design included reversible sample heating by means of a filament which is in direct contact with the sample bottom side via a sapphire piece. This system should be redesigned because the sapphire piece obstructed sample transfer. Though even without the filament going from higher to lower temperatures is still possible by regulating the liquid He flux and counterheating the cold tip, direct heating through heat conduction is preferable in terms of liquid helium consumption.
- The sample contact system turned out to be rather fragile and false electrical contacts sometimes occurred in the sample manipulator. This could also be the case for the sample in the STM baseplate.
- The Cu-Be balls could eventually be replaced by sapphire balls. This might lead to a better defined stick-slip behaviour over time since sapphire does not wear as much.
- Asymmetries between coarse approach and retraction could be lifted by inclining the piezoceramic tubes according to the pitch angle of the ramps.

Chapter 4

Thin Superstructured Oxide Films on Metal Substrates

4.1 Introduction

In the search of suitable supports for model systems in heterogeneous catalysis, i.e. small metal clusters, ultrathin oxide films on metals have proved to be excellent candidates [12, 13, 70]. The deposition or growth of small metal clusters onto ultrathin oxide layers grown on metal substrates allows to study the catalytic properties of the clusters by charged-particle surface characterization techniques, which is not possible in the case of bulk oxide supports. Moreover, ultrathin defect-free oxide films with a superstructure can be used for the growth of a regular array of metal clusters with a narrow size distribution [13, 71]. Such a distribution facilitates the study of the strongly size-dependent catalytic properties of the metal clusters, which could so far only be addressed by depositing size selected clusters from the gas phase [72–74]. The latter technique requires, however, elaborate experimental techniques for cluster production. Monodispersed clusters can be produced by using a quadrupole mass spectrometer for size-selection, but for kinetic energies above 1 eV cluster fragmentation upon landing can occur [74]. Furthermore, no control of the cluster arrangement on the surface is possible. In contrast, self-organized growth on superstructured oxide films can result in regularly spaced metal clusters and relies only on standard UHV instrumentation. Consequently, superstructured thin oxide films are especially interesting as a support for model catalysts.

A range of ultrathin oxide layers on metallic substrates has already been investigated [12, 75], with a focus on well-known bulk oxides and technologically relevant systems such as Al_2O_3, TiO_2, or MgO. A few systems have been observed to form superlattices owing to the lattice misfit between the metal substrate and the oxide adsorbate [76, 77].

In this chapter two ultrathin superstructured oxide films are presented. First, we have reproduced the moiré pattern of FeO/Pt(111) and, second, we have studied MgO overlayers on Mo(100)–(1 × 1)–O, which form a superstructure induced by a presumably c(2 × 14)–O reconstructed interface.

4.2 FeO/Pt(111)

The system FeO/Pt(111) has been investigated by several groups [78–82]. Depositing 0.75–1.75 ML FeO on Pt(111) results in a hexagonal oxide overlayer with a lattice constant of 3.09 Å and a rotational angle of 0.6° with respect to the Pt substrate [79, 81]. The resulting moiré pattern has a periodicity of about 26 Å and a rotation angle of 5.2°. It was shown that the iron oxide forms a bilayer with the oxygen atoms outermost and an interplanar spacing of 1.25 Å [80].

The FeO/Pt(111) moiré pattern would seem adequate for the growth of metal clusters of about 7 atoms in terms of superstructure periodicity. However, a suitable template for the growth of small iron clusters must also be inert enough, i.e. it should not form a compound with the cluster material. We reproduced the FeO/Pt(111) superstructure and deposited small iron islands onto the oxide layer to test its reactivity. At the same time the reproduction of a previously reported FeO/Pt(111) structure was a test for our new UHV system.

The Pt(111) sample was cleaned by repeated cycles of sputtering at 800 K, annealing at 800 K in $5 \cdot 10^{-8}$ mbar oxygen background pressure, and subsequent flash annealing to 1400 K. The FeO layer was prepared following the procedure indicated in Ref. [79]. Iron was evaporated from a pure iron wire (⌀ 2 mm, 99.998 % purity) in an e-beam evaporator (Omicron, EFM 3T, flux during evaporation: ∼20 nA). After Fe deposition the sample was heated to 980 K for about 1 min in $4.5 \cdot 10^{-6}$ mbar of oxygen, followed by a rapid cooldown to room temperature.

The thickness of the FeO layer was inferred from AES measurements carried out after deposition of Fe onto the clean Pt(111) surface. In a first approximation, for layer by layer growth, the intensity of a Fe AES peak

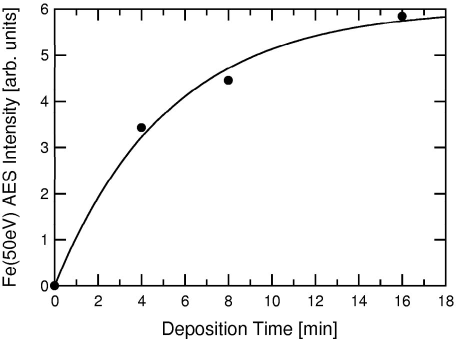

Figure 4.1: AES signal (peak-to-peak height) of the Fe 50 eV peak for Fe/Pt(111) as a function of Fe evaporation time.

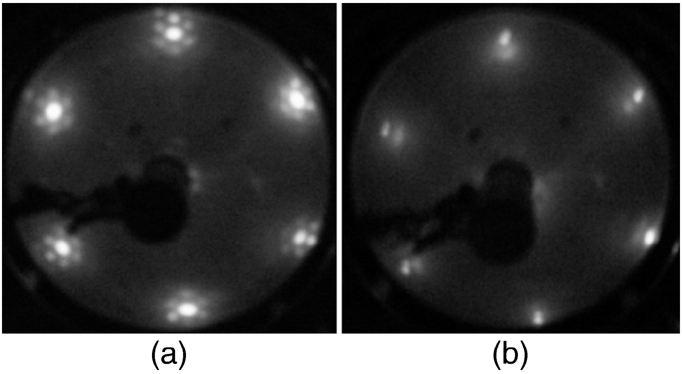

Figure 4.2: LEED pattern of (a) 1 ML FeO/Pt(111), (b) 0.1 ML Fe on 1 ML FeO/Pt(111).

increases exponentially with the number of deposited Fe monolayers. In Figure 4.1 the intensity of the Fe 50 eV AES peak is reported. The increase of the Fe peak signal is well fitted by an exponential $(1-\exp(-t/t_0))$ with a decay constant of $t_0 = 5.2$ min. From the mean free path of 50 eV electrons of 2 ML we infer an evaporation flux of 0.4 ML/min.

In Figure 4.2 (a) a LEED pattern of about 1 ML of FeO on Pt(111) taken at 60 eV is shown. Each of the six main spots, which are due to the FeO lattice, is surrounded by six satellite spots. The pattern is characteristic for the moiré FeO overlayer observed by other groups [78–82].

Upon deposition of 0.1 ML of Fe onto the FeO/Pt(111) superstructured surface at 140 K the satellite spots disappear as can be seen in Figure 4.2 (b). We conclude that the iron atoms do not form regularly distributed islands on the FeO/Pt(111) moiré superstructured surface but instead bind strongly to the iron oxide.

4.3 MgO/Mo(100)

4.3.1 Introduction

In the following we report on an ultrathin superstructured MgO film on a molybdenum substrate. Thin MgO layers are of particular interest because bulk magnesium oxide is commonly used as a support for industrial metal catalyst particles due to its chemical, thermal and mechanical stability [83, 84]. Ultrathin MgO films have been grown epitaxially on Ag(100) [14, 85, 86] and Mo(100) [87–89] surfaces with a (1 × 1) stochiometry. MgO films of only a few Ångström thickness can already exhibit bulk oxide properties [14] and their suitability as a support for cluster deposition has recently been demonstrated [70]. Goodman and co-workers first reported an epitaxial growth of MgO(100) on Mo(100) for a substrate temperature of 200–600 K [87–89]. On the other hand, STM studies of MgO thin films on Mo(100) carried out by Gallagher et al. [76, 90] revealed the growth of smooth and uniform MgO films with small MgO domains (20–60 Å) at 300–900 K.

To our knowledge no MgO film with a superstructure on a metal (100) surface has been reported so far. We have observed a thin MgO film on molybdenum (100) with a c(14 × 2) superstructure, which is obtained by MgO growth on a Mo(100)–(1 × 1)–O surface and subsequent annealing to 1300 K. The c(14 × 2) pattern most probably relates to a surface reconstruction of the oxygen covered molybdenum (100) substrate.

Oxygen induced reconstructions of the Mo(100) surface have been reported by several groups [91–96]. At a sample temperature of 820–1100 K or 600–700 K with subsequent annealing to 1000–1450 K the following structures were commonly observed in the coverage range of 0.2–1.4 ML: c(4 × 4) at $\theta \approx 0.3$ ML, (2 × 1) at $\theta \approx 0.4$ ML, $(\sqrt{5} \times \sqrt{5})$R26° at $\theta = 0.8$ ML, (2 × 1) at $\theta \approx 1$ ML, (4 × 1) at $\theta \approx 1$ ML, c(2 × 2) at $\theta \approx 1.1$ ML, and a diffuse (1 × 1) pattern for $\theta \gtrsim 1.4$ ML. The $(\sqrt{5} \times \sqrt{5})$R26° structure consists of Mo_4O_4 clusters as confirmed by STM studies [91]. The transitions between the various structures are smooth, and at most coverages the coexistence of different structures was observed [95, 96]. For oxygen adsorption at 300 K further oxygen induced reconstructions, namely a c(2 × 2) at $\theta = 0.15$ ML, a (6×2) at $\theta = 0.33$ ML, a (6×1) at $\theta = 0.66$ ML, and a (3×1) structure at $\theta = 1$ ML, were found [95]. The variety of observed structures points to the sensitivity of the system with respect to oxygen adsorption conditions and subsequent surface treatments. There might be a range of other possible structures if the growth conditions are altered.

In the next section, we first report on the structure of ultrathin MgO(100) layers grown on Mo(100)–(1×1)–O and then on reconstructed oxygen overlayers on Mo(100), revealing the influence of the interface structure onto the MgO layer.

4.3.2 Experimental

The experiments were carried out at a base pressure of 1.2×10^{-10} mbar.

The sample is a hat-shaped Mo(100) crystal (diameters 7.0 and 10.0 mm of top surface and of rim, respectively, total thickness 3.0 mm) with 99.99 % purity and 0.1° orientational accuracy (MaTeck). The W–5%Re/W–26%Re (C-type) thermocouple is used to measure temperature.

Sample Preparation

Quite different cleaning procedures of Mo(100) crystals have been reported in the literature. The standard procedure consists of repetitive cycles of annealing at 1300 K in an oxygen pressure of 10^{-7} mbar to remove segregating impurities, such as carbon, and a subsequent flash to 2000 K or above, which removes chemisorbed oxygen [90, 95]. Variations of this procedure go from repetitive heating to 2200 K without oxygen treatment [89] to cycles of Ar^+-ion sputtering at 300 K with annealing to only 1100 K under oxygen [93]. With our Mo(100) crystal the standard procedure led to oxygen free surfaces revealing an excellent (1×1) LEED pattern, however, with a few percent of C at the surface, as evidenced by AES. Note, however, that the C coverage did not suffice to produce the weak $c(2 \times 2)$ LEED pattern reported in ref. [97]. The C segregated from the bulk during flash annealing to the surface. Its amount diminished during the course of prolonged preparation, however, at a rate implying that an entirely clean surface would have taken a few months of preparation. We attribute this problem to the comparably large volume of our crystal.

An AES clean Mo(100) surface ($\theta_O, \theta_C \ll 1\%$) could be obtained after sputtering the sample for 10 min at room temperature. However, this surface was less well ordered as inferred from the broad (1×1) spots in the LEED pattern. This surface was used for the Mg coverage calibration as described below.

In order to work with a highly ordered and chemically well defined surface we chose to use a (1 × 1) O–covered Mo(100) surface as starting substrate. To produce a Mo(100)–(1 × 1)–O surface the Mo substrate was prepared by repeated cycles of sputtering (Ar^+ ions, 1 keV, 0.5 μA, 20 min) and annealing at 1200 K under an oxygen partial pressure of 1×10^{-7} mbar (20 min). After annealing, the heating power and oxygen partial pressure were removed simultaneously. This led to a Mo(100) surface with an oxygen saturation coverage of 1.0 ± 0.1 ML with no further impurities, as determined by AES, and a sharp (1 × 1) LEED pattern. Note that the escape length for Mo is taken to be the same (2 ML) as that determined for Mg below. If we take an escape length uncertainty into account, the error of the coverage is estimated to be 0.3.

Mg and MgO Coverage Calibration

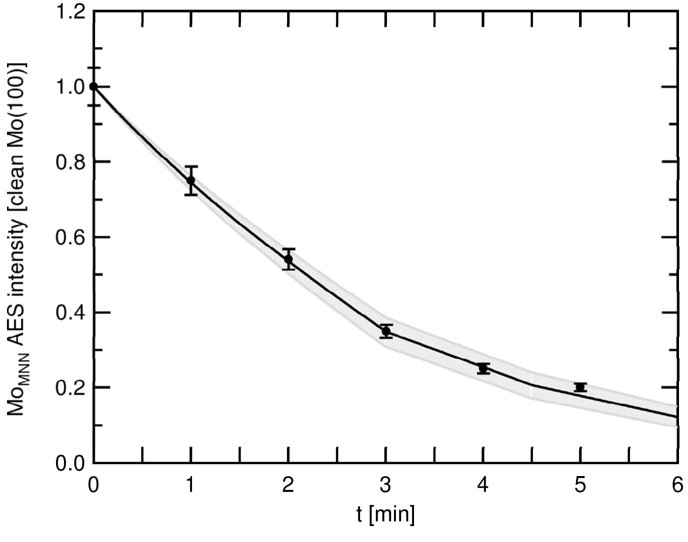

Figure 4.3: Normalized intensity of the Mo_{MNN} Auger signal (190 eV) versus Mg deposition time for Mg deposition onto the clean Mo(100) substrate at 300 K. The first break in slope is caused by a transition of growth morphology from 3D islands due to limited interlayer diffusion to layer-by-layer growth. This transition takes place at 2.0 ML of pseudomorphic Mg on Mo(100).

Mg was evaporated onto the AES clean Mo(100) surface at a background pressure of $p_{\mathrm{tot}} < 2 \times 10^{-10}$ mbar from a BNi crucible of a Knudsen cell operated at 650 K. The Mg deposition flux has been calibrated by monitoring the $\mathrm{Mo_{MNN}}$(190eV)-Auger peak–to–peak height as it is attenuated in the course of Mg deposition (see Figure 4.3). The sample temperature during deposition was chosen to be 300 K since for this case the growth morphology has been reported as a function of film thickness in a recent STM study [97]. Submonolayer films were reported to nucleate from a high density of islands having already at 0.3 ML small second layer islands on-top. Subsequent deposition leads to island growth on the first and second atomic plane until first and second layer coalesce and finally get completely filled. For coverages between 2.0 ML and 4.0 ML, the STM study reports step flow growth which is attributed by the authors to a higher adatom diffusion constant on-top the second Mg layer [97]. The distinct change in growth morphology at 2.0 ML is reflected in a different attenuation rate of the substrate AES signal [98]. Our $\mathrm{Mg_{MNN}}$-Auger peak–to–peak heights reported in Figure 4.3 clearly show the change of slope which can safely be identified with a coverage of 2.0 ML. Apart from a slight vertical buckling of the surface leading to a c(2 × 2) structure, Mg was reported to grow pseudomorphic on Mo(100) until 4.0 ML where it starts to form a hexagonal lattice. The Mg monolayer definition therefore refers to one Mg atom per Mo(100) unit cell.

For the quantitative analysis of our AES data we consider the attenuation length λ of the $\mathrm{Mo_{MNN}}$(190eV)-Auger electrons when they escape through the Mg film as fit parameter. The growth morphology is modeled assuming a poisson distribution for the filled layers up to 2.0 ML and subsequently step flow growth. This leads to the following equations for the Mo AES intensity y as a function of Mg layer thickness s [ML] and Auger electron escape depth λ:

$$s < 2: \qquad y(s,\lambda) = [1 - s_1(s)] + [s_1(s) - s_2(s)]\,\mathrm{e}^{-1/\lambda} + s_2(s)\,\mathrm{e}^{-2/\lambda}$$

$$\text{with} \quad s_1(s) := \frac{1-\mathrm{e}^{-s}}{1-\mathrm{e}^{-2}} \quad \text{and} \quad s_2(s) := s - \frac{1-\mathrm{e}^{-s}}{1-\mathrm{e}^{-2}} \tag{4.1}$$

$$2 \le s < 3: \qquad y(s,\lambda) = [1 - (s-2)]\,\mathrm{e}^{-2/\lambda} + (s-2)\,\mathrm{e}^{-3/\lambda} \tag{4.2}$$

$$3 \le s < 4: \qquad y(s,\lambda) = [1 - (s-3)]\,\mathrm{e}^{-3/\lambda} + (s-3)\,\mathrm{e}^{-4/\lambda} \tag{4.3}$$

The best fit to the AES signal in Figure 4.3 is obtained for an escape depth of $\lambda = 1.9 \pm 0.2$ ML, which corresponds to 4 Å according to the Mg interlayer distance on Mo(100) [97] and is a reasonable value. The Mg deposition flux as inferred from our data is $F = (0.67 \pm 0.07)$ ML/min.

We note that our growth model leads to a non-linear fit function $y_\lambda(s)$

for $s < 2$ ML owing to the nucleation of small first layer islands on top of the first layer islands. In contrast, a linear fit would result from a model assuming only ideal bilayer islands with no second layer atoms exposed up to completion of 2 ML [98]. As can be seen from Figure 4.3 a non-linear function fits better to our experimental AES data points, as it should be according to the growth morphology inferred from STM.

MgO films were grown by Mg deposition at an oxygen partial pressure of 1×10^{-7} mbar and a sample temperature of 600 K. In this process the MgO thickness is given by the Mg coverage. According to AES $\mathrm{O_{KLL}/Mg_{MNN}}$ peak–to–peak ratios our MgO(100) overlayers are stoichiometric. MgO(100) grows on Mo(100) with a 45° rotation roughly pseudomorphic (the misfit is -5.5%). Therefore MgO(100)/Mo(100) has the same atomic Mg density as Mg/Mo(100) and thus the flux calibration above equally refers to MgO(100) monolayers.

4.3.3 MgO Overlayers on Mo(100)–(1×1)–O

Figure 4.4 (a) shows the LEED pattern of the Mo(100)–(1 × 1)–O substrate, taken at 60 eV, which exhibits sharp (1 × 1) diffraction spots. After the growth of a MgO film of 7.2±1.2 ML the same LEED diffraction spots appear (see Figure 4.4(b)) indicating that the MgO layer grows epitaxially, in agreement with the results reported earlier in the Literature [89, 99]. The LEED spots are, however, much more diffuse than those obtained for the Mo(100)–(1 × 1)–O substrate, which might be due to the presence of MgO ordered domains. In fact, MgO domains on Mo(100) of a size of 20–60 Å were reported earlier by Gallagher et al. [90]. Upon annealing the MgO film at 1300 K for a few seconds and subsequent slow decrease down to room temperature new LEED spots with satellites, characteristic for the formation of a superstructure, appear in the LEED image (Figure 4.4(c)), in addition to the large and bright (1 × 1) spots. The distance between a new spot and one of its satellites is equal to about one sixth of the distance between the (00) spot and the (10) spot of the substrate.

Figure 4.5 shows the Auger spectra corresponding to the three LEED patterns of Figure 4.4. In the AES signal for the Mo(100)–(1×1)–O substrate (curve (a)) the molybdenum MNN peaks can be found at 170–250 eV and the oxygen KLL peaks at 480–550 eV. An additional Mo Auger transition at 30 eV is also visible in the bottom panel, which is a zoom of the 10–50 eV energy range. After the deposition of 7.2±1.2 ML of MgO (curve (b)) the Mo peaks have almost vanished. The main Mg LVV peak appears at an energy of 33 eV, which is evidence of oxidized magnesium $\mathrm{Mg^{2+}}$ [99]. Note that metallic magnesium has its main LVV peak nominally at 48 eV.

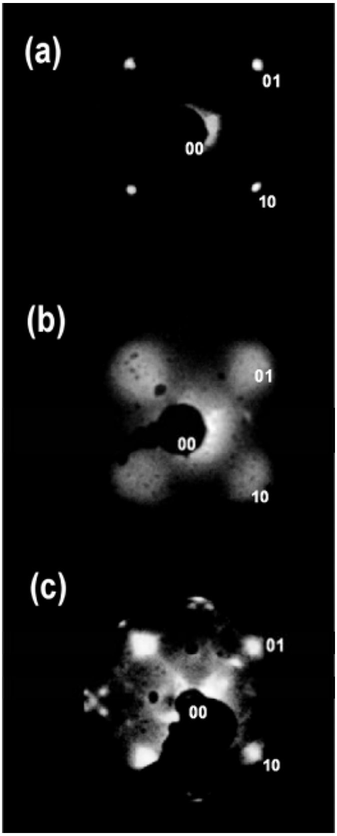

Figure 4.4: LEED patterns taken at $E = 60$ eV. (a) Clean Mo(100)–(1×1)–O surface. (b) After growth of 7.2 ± 1.2 ML MgO(100) on Mo(100)–(1 × 1)–O at 600 K. (c) After annealing to 1300 K the MgO–coverage reduces by thermal desorption to 2.5 ± 0.4 ML and an ordered superstructure appears.

Oxidation also induces a shift of the oxygen KLL peaks by some eV towards lower energies. Curve (c) shows the AES spectrum after annealing the MgO surface to 1300 K. The increased Mo Auger peak heights indicate that during the annealing process a significant amount of MgO evaporates. Only 2.5 ± 0.4 ML of MgO remain on the surface, as inferred from the $\mathrm{Mo_{MNN}}$(190eV)-Auger signal.

The LEED pattern in Figure 4.4 (c) corresponds thus to a MgO layer

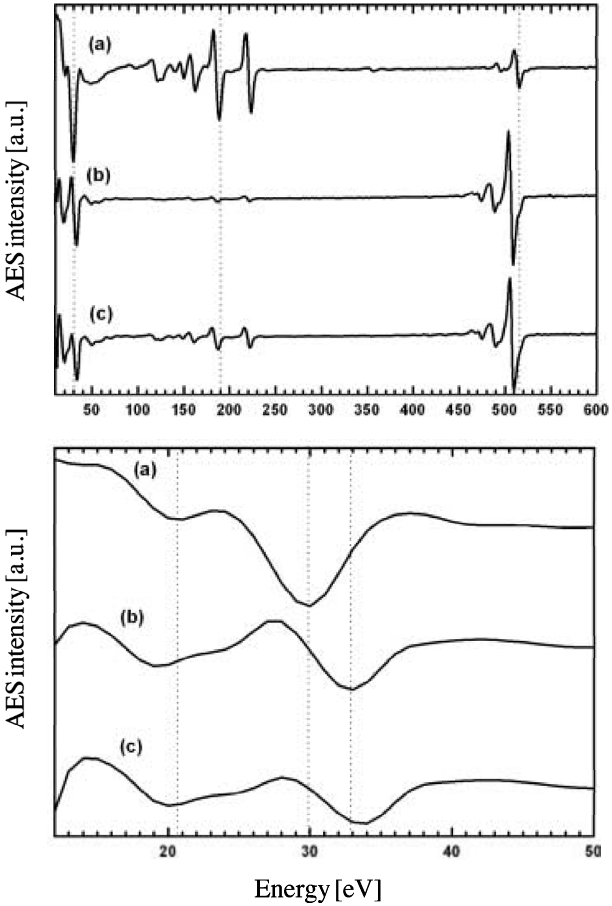

Figure 4.5: Auger spectra recorded from the samples for which LEED patterns are shown in Figure 4.4. (a) Clean Mo(100)–(1 × 1)–O surface. (b) After growth of 7.2 ± 1.2 ML MgO(100) on Mo(100)–(1 × 1)–O at 600 K. (c) After annealing to 1300 K.

of 2.5 ± 0.4 ML thickness on a Mo(100)–(1 × 1)–O substrate. The observed pattern could originate either from a MgO superstructure or from an interfacial reconstruction of Mo(100) induced by oxygen. To clarify this question we have also studied oxygen layers on Mo(100).

4.3.4 Oxygen Overlayers on Mo(100)

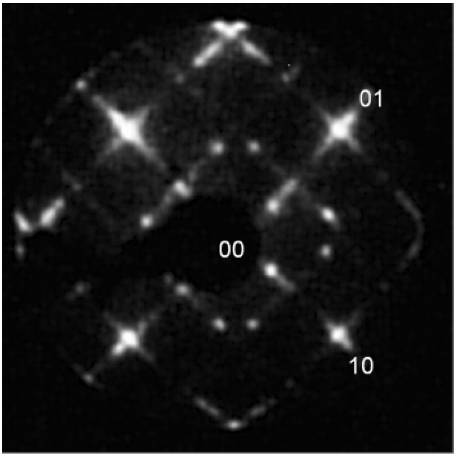

Figure 4.6: LEED pattern of the Mo(100)–(1 × 1)–O surface after annealing to 1300 K ($E = 60$ eV).

In order to find out if the LEED pattern of the annealed MgO film on Mo(100)–(1 × 1)–O is caused by an interfacial reconstruction, we have annealed the Mo(100)–(1 × 1)–O substrate surface at 1300 K in exactly the same way. The resulting LEED pattern taken at 60 eV is shown in Figure 4.6. It is essentially the same as that for the annealed MgO film on Mo(100)–(1 × 1)–O (Figure 4.4 (c)) but has better resolved spots. Figure 4.7 (a) depicts the LEED image of the annealed Mo(100)–(1 × 1)–O surface taken at an energy of 30 eV, for which the (00), (01) and (10) spots are still visible.

In Figure 4.8 Auger spectra of the molybdenum MNN (top panel) and oxygen KLL (bottom panel) peaks taken before and after annealing the Mo(100)–(1 × 1)–O surface at 1300 K are compared. After annealing, the AES peaks are shifted toward lower energies by 1–2 eV. There is, however, no sign of Mo^{4+} or Mo^{6+} peaks corresponding to MoO_2 and MoO_3 oxides, which would appear shifted by 5–7 eV with respect to the metallic Mo^0 peaks [96, 100]. We conclude that annealing the Mo(100)–(1 × 1)–O surface at 1300 K leaves the oxygen on the surface in a chemisorbed state and does not lead to any oxide formation. The normalized peak-to-peak height of the Mo_{MNN}(190eV) Auger signal remains constant upon annealing, whereas the O_{KLL}(516eV) Auger signal increases by 17 ± 5 %. The origin of this increase is not clear. The presence of subsurface oxygen diffusing to the surface upon

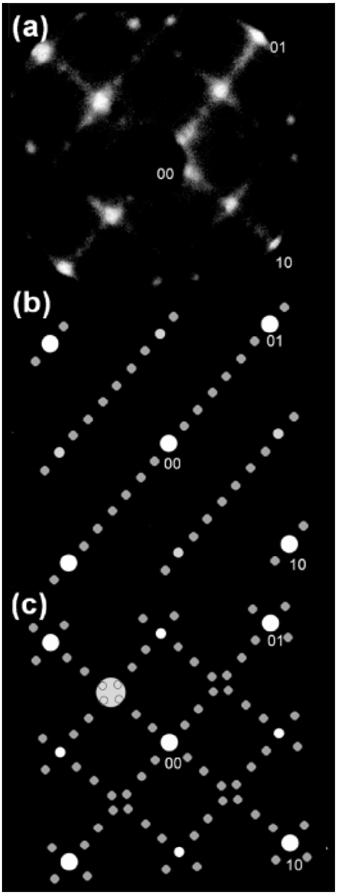

Figure 4.7: (a) LEED pattern of the Mo(100)–(1 × 1)–O surface after annealing at 1300 K ($E = 30$ eV). (b) Schematic representation of the LEED image resulting from a c(2 × 14)–structure. (c) Schematic representation of the LEED image expected for a surface with coexistence of the two possible domains of the c(2 × 14)–structure which are rotated by 90° with respect to each other.

annealing is unlikely, nor can we relate the increase to structural changes of the oxygen surface layer.

We propose that the LEED pattern in Figures 4.6 and 4.7 (a) originates from a c(2 × 14)–O reconstruction of oxygen on Mo(100). Figure 4.7 (b) rep-

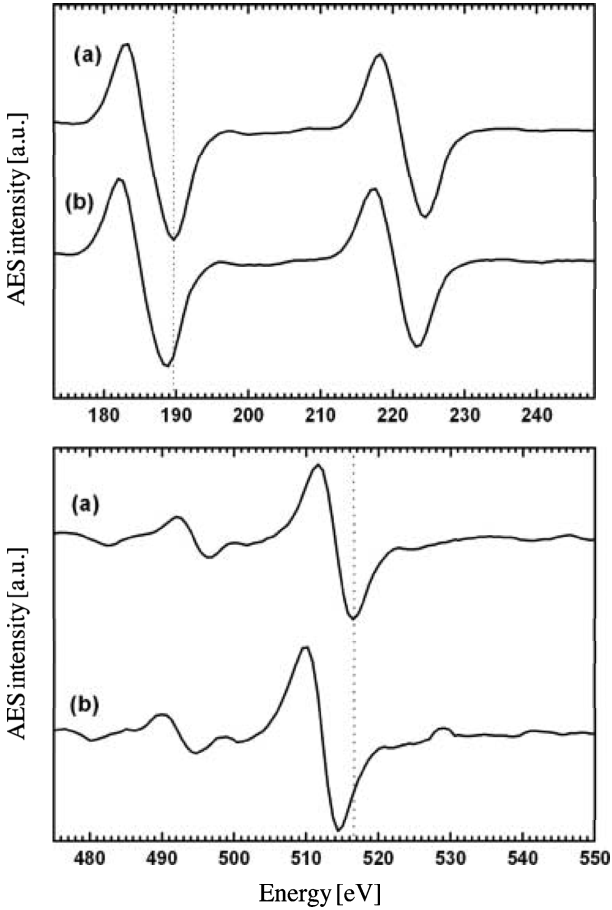

Figure 4.8: Auger spectra recorded from the samples for which LEED patterns are shown in Figure 4.4. (a) Clean Mo(100)–(1 × 1)–O surface. (b) After growth of 6 ± 1 ML MgO(100) on Mo(100)–(1 × 1)–O at 600 K. (c) After annealing to 1300 K.

resents a schematic LEED pattern of a c(2 × 14) superstructure. Because of the fourfold symmetry of the Mo(100)–(1 × 1)–O surface, the two reciprocal lattices of a c(2 × 14) superstructure rotated by 90° with respect to each other are equivalent. The superposition of these reciprocal lattices leads to the theoretical LEED pattern given in panel (c) of Figure 4.7, which is very similar to the real LEED pattern of our annealed Mo(100)–(1 × 1)–O surface (panel (a)). The distances between intense spots correspond reasonably well and almost all spots can be identified, despite the low intensity or poor resolution of some spots of the real LEED pattern. The proximity of the four spots indicated by a large white circle in the theoretical LEED pattern (c) could result in one large spot in the experimental LEED image (a). Possibly, the formation of a c(2 × 14)–O reconstruction on Mo(100) could be facilitated by a small excess of oxygen on the annealed Mo(100)–(1 × 1)–O surface. An excess of Pd was found to be responsible for the transformation of a c(2 × 2) structure into a c(2 × n) structure ($n = 8, 10$) for Pd on Mo(100) [101].

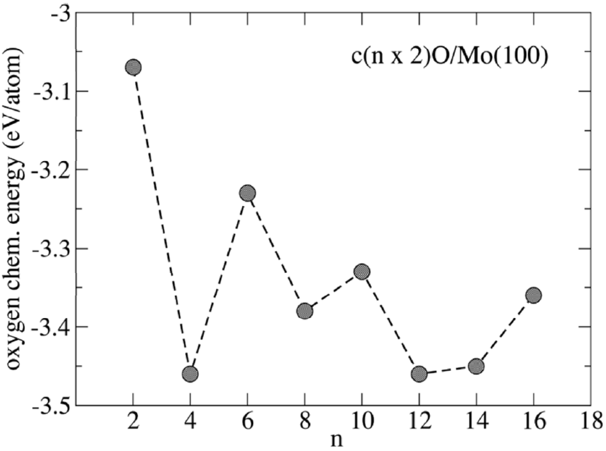

Figure 4.9: Binding energy per O atom for a c(2 × n)–O reconstruction on Mo(100) as determined by density functional calculations (Zeljko Sljivancanin, chaire de simulation à l'échelle atomique, Prof. A. Pasquarello, EPFL). The c(2 × 14)–O structure represents a local energy minimum.

To find out if the formation of a c(2 × 14) superstructure of oxygen on the Mo(100)–(1 × 1)–O surface is energetically favored, and what the exact surface structure could be, density functional theory (DFT) calculations have been performed by Zeljko Sljivancanin[1]. In Figure 4.9 the binding energy per oxygen atom in c(2 × n)–O structures is given as a function of n. Calculations were done for a slab model. Five Mo bcc(100) layers separated by 11 Å of vacuum are repeated in a super-cell geometry. A theoretical

---

[1] Chaire de simulation à l'échelle atomique, Prof. A. Pasquarello, EPFL

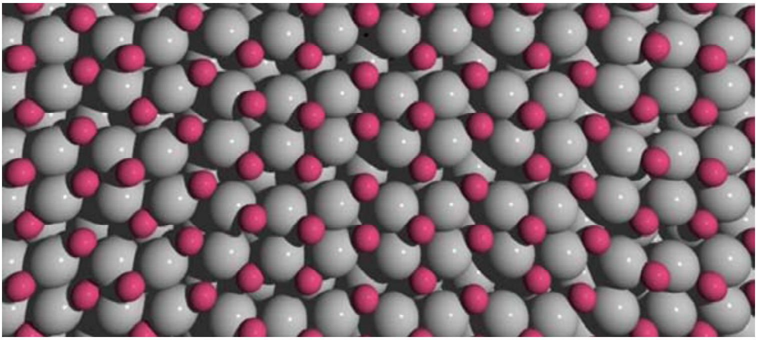

Figure 4.10: Structural model for a c($2 \times n$)–O reconstruction on Mo(100) as determined by density functional calculations (Zeljko Sljivancanin, chaire de simulation à l'échelle atomique, Prof. A. Pasquarello, Institut de théorie des phénomènes physiques, EPFL). The oxygen atoms and the first and second layer Mo atoms were allowed to relax.

lattice constant of 3.2 Å and 1 ML of oxygen was assumed. The O atoms as well as the two uppermost Mo(100) layers were allowed to relax. The GGA-PW91 exchange-correlation functional and Brillouin-zone integration over 4 k-points was used. The c(2×14)–O structure belongs actually to the energetically favored structures even if no global energy minimum is obtained at $n = 14$. The corresponding structural model in Figure 4.10 shows how in the c(2×14)–O structure the toplayer Mo atoms arrange into four-atom clusters. Therefore the c(2×14) structure is not a bare adsorbate superstructure, but it involves considerable rearrangement of substrate atoms.

The formation of a c(2×14) superstructure after deposition of about 1 ML of oxygen onto a clean Mo(100) surface has, to our knowledge, never been reported in the Literature. We observe this structure upon annealing the Mo(100)–(1×1)–O surface at 1300 K. Most probably, the slightly different surface treatment is responsible for the formation of this new structure.

4.3.5 Conclusions

In summary, we have shown that the annealing of 2.5 ± 0.4 ML MgO on Mo(100)–(1×1)–O at 1300 K leads to the formation of a superstructure exhibiting a LEED pattern very similar to that of the annealed Mo(100)–(1×1)–O substrate. We conclude that the MgO structure does most probably not correspond to a reconstruction of the MgO overlayer on the (1×1) Mo(100) substrate, but to the MgO film residing on an interfacial superstructure induced by oxygen. The LEED pattern of the interfacial superstructure could originate from a $c(2 \times 14)$–O reconstruction of the Mo(100) surface, assuming two domains rotated by 90° with respect to each other. This means the reordering of the interface upon annealing is dominant and a crucial factor for the structure of the oxide overlayer.

Chapter 5

Coarsening by Cluster Diffusion

5.1 Introduction

One way to obtain small metal clusters with a narrow size distribution is self-assembly on a single crystal surface. By carefully controlling the deposition flux and the substrate temperature the mean metal island size can be tuned [102, 103]. This requires a deep knowledge of the atomistic processes involved in the growth mechanism, in particular of the surface diffusion of adsorbed atoms.

The starting point for the growth of metal islands of specific size on metal surfaces is the deposition of single atoms through adsorption from the gas phase. At low enough temperatures thermally activated diffusion of the adsorbed atoms is frozen, which leads to statistical growth. This growth regime can be characterized by $D/F < 1$, where D is the monomer diffusion rate (mean number of surface unit cells visited by an adatom per unit time) and F the deposition flux (number of impinging atoms per surface unit cell per unit time). When a metal atom from the vapor phase arrives at the surface the energy gain upon adsorption can either be transferred to the substrate lattice or induce a lateral kinetic displacement of the impinging atom. The latter is called transient mobility and leads to a non random distribution of the metal atoms after adsorption since the diffusing atoms are more likely to bind to energetically favored surface sites. No transient mobility has been detected for all metal/metal nucleation systems investigated on the atomic-scale [104].

For Pt/Pt(111) the absence of transient mobility was evidenced by a field ion microscopy study [105]. An occasional occupation of hcp sites after the deposition of single Pt atoms onto a Pt(111) cluster at 20 K was found, despite the higher binding energy at fcc sites. Thermally activated diffusion out of hcp sites occurs only at 45 K resulting in the exclusive occupation of fcc sites.

For Ag/Pt(111) transient mobility was ruled out on the basis of mean island size measurements by STM [106]. In the case of statistical growth on a hexagonal lattice the mean island size at 0.1 ML coverage is 1.4 atoms without (pure statistical growth) and 2.3 with transient mobility according to the rate equations of mean-field nucleation theory [107], integrated for no diffusion, and according to Monte-Carlo simulations, carried out for no diffusion except over one lattice site. The experimental value of 1.2 ± 0.3 atoms found for Ag/Pt(111) upon deposition of 0.1 ML Ag at 35 K therefore permits to exclude transient mobility.

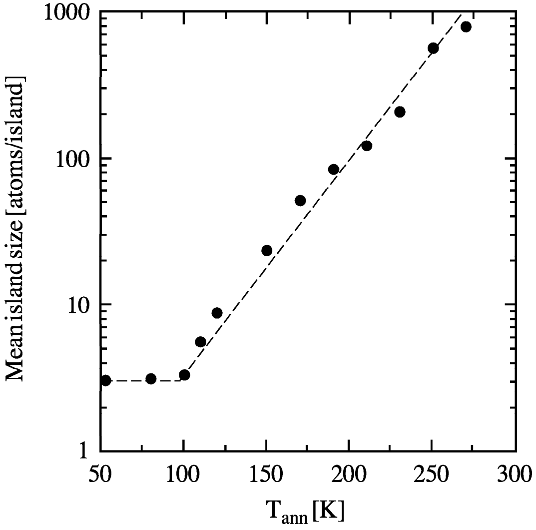

Figure 5.1: Mean island size of 0.1 ML Ag on Pt(111) as a function of annealing temperature. The temperature range below 100 K is characterized by stable dimers. The sudden exponential increase in island size at higher temperatures is due to Ostwald ripening.

Annealing a surface with a random monomer distribution after deposition leads to monomer diffusion and the formation of larger islands, essentially dimers and trimers. Note that even in the $D/F < 1$ regime some dimers already form during deposition due to the impingement of atoms from the gas phase onto or adjacent to sites already occupied. Further increase in temperature leaves the mean island size unchanged as long as dimers do not diffuse or dissociate. This temperature range is clearly identified for Ag/Pt(111) in Figure 5.1. At a certain critical temperature (100 K for Ag/Pt(111)) a sudden exponential increase in the mean island size occurs, which has been attributed to Ostwald ripening [108]. Ostwald ripening is a coarsening process induced by the dissociation of clusters at the surface. Owing to the increased temperature small clusters, such as dimers, dissociate and single atoms evaporate from island edges. The free atoms diffuse on the surface and join islands upon encounter at random. Since the evaporation rate is lower for large than for small islands, the large islands grow at the expense of the smaller ones. Ostwald ripening can be used to form compact islands containing a specific average number of atoms [102, 103] and the threshold energy yields information about the dimer dissociation energy. In the case of Ag/Pt(111) a dimer dissociation barrier of 320 ± 20 meV was estimated [106].

It has been believed that the barrier for dimer diffusion has to be significantly smaller than that for dimer dissociation, should dimer diffusion affect the nucleation process [102, 109, 110]. As this condition is generally not fulfilled for clusters on hexagonal surfaces [102], growth processes of many hexagonal metal/metal systems can be expected to resemble those of Ag/Pt(111). At the same time systems for which diffusion barriers are expected to be low as compared to dissociation barriers could behave differently and are all the more interesting to be investigated. In the following we report on diffusion and nucleation results obtained for Pt/Pt(111) and Co/Pt(111). For both systems we have observed a stepwise increase of the mean island size with annealing temperature, which stands in contrast to the coarsening process found for Ag/Pt(111).

5.2 Experimental

The experiments were carried out in another laboratory of our group using a UHV chamber with a base pressure of $3 \cdot 10^{-11}$ mbar, equipped with standard surface preparation and characterization instruments and a variable-temperature scanning tunneling microscope. The Pt(111) substrate was prepared by repeated cycles of 1000 eV Ar^+ sputtering at 800 K, followed by exposure to $3 \cdot 10^{-8}$ mbar of oxygen at 800 K and subsequent flash annealing at 1400 K. The sample cleanliness was verified by AES and STM. Co was deposited by e-beam evaporation from a high-purity rod (99.998%). Pt was evaporated by resistive heating of a high-purity (99.998%) Pt wire using a home-made evaporator. Typical evaporation rates are 0.1 ML/min. During surface preparation the chamber pressure remained below $5 \cdot 10^{-11}$ mbar.

The measurements were carried out in the following way. After each increase of the sample temperature the surface was held at that specific temperature for 5 min, during which temperature-dependent diffusion processes occurred. The sample temperature was then lowered by 10 K to freeze the diffusion processes and after some delay time, necessary to reach thermal equilibrium of the STM, the island densities were measured by acquiring several STM images at the fixed temperature. The mean island size s was inferred from the coverage and the island densities (number of islands per surface unit cell) according to $\theta = n \cdot s$, where n is the island density and θ the coverage.

5.3 Results and Discussion

Figure 5.2 shows STM images taken at different stages of the coarsening process of Co on Pt(111). 0.01 ML of Co were deposited at 50 K, where diffusion is frozen, thus leading to randomly distributed monomers. Hereafter, the surface was annealed step by step following the procedure described above. The decrease in island density and simultaneous increase in mean island size is clearly visible on the STM images. In Figure 5.3 the mean island size is plotted versus annealing temperature in the range of 50–240 K. We observe a stepwise increase of the island size from 50 K up to 210 K. This behavior can be explained assuming that dimer and trimer diffusion takes place before their dissociation. Annealing the surface above 62 ± 4 K induces monomer diffusion resulting in the formation of dimers and trimers, which prevail up to 90 K. After the onset of dimer diffusion at about 90 ± 5 K a further plateau develops. In this temperature range the mean cluster size is about 4.8 atoms, compatible with a great number of clusters containing about five atoms. At still higher temperatures a third saturation regime with a mean island size of about 7 atoms can be observed, triggered by the diffusion of trimers starting at 147 ± 8 K.

The stepwise increase of the mean island size can be reproduced by kinetic Monte-Carlo simulations accounting for monomer and dimer diffusion as indicated by the red curve in Figure 5.3. The free parameters entering the Monte-Carlo simulation are the attempt frequencies and the migration barriers, cluster dissociation was excluded. The annealing time was 1 h. Good agreement with the data is obtained for a general attempt frequency

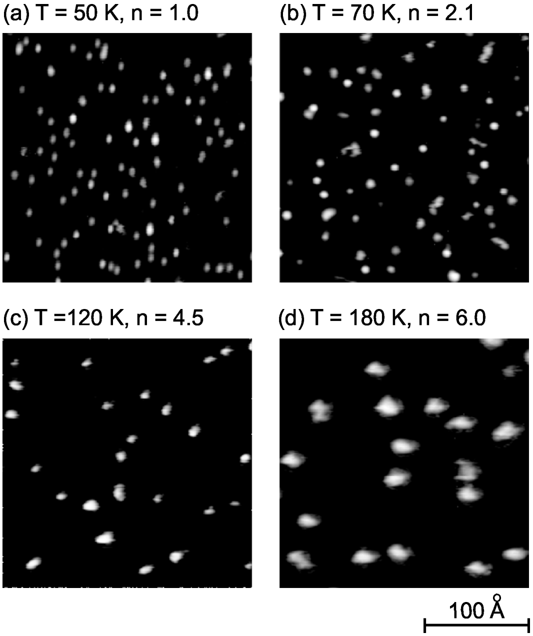

Figure 5.2: 240×240 Å^2 STM images ($I_t = 1.0$ nA, $V_t = 1.0$ V) of 0.01 ML Co deposited onto Pt(111) at 50 K and annealed to the indicated temperatures. n indicates the resulting mean island sizes.

of $\nu_0 = 1.5 \cdot 10^{15}$ Hz and migration barriers of $E_{m,1} = 0.21 \pm 0.02$ eV and $E_{m,2} = 0.27 \pm 0.02$ eV for monomers and dimers, respectively. The migration barrier for trimers was extracted from a numerical integration of the rate equations from mean-field nucleation theory (see Appendix C) for the case of monomer, dimer, and trimer diffusion, as shown by the blue line in Figure 5.3. Assuming $\nu_0 = 1.5 \cdot 10^{15}$ Hz we found an energy barrier of $E_{m,3} = 0.44 \pm 0.05$ eV for trimer diffusion.

Figure 5.4 shows the mean number of atoms per island versus annealing temperature for Pt on Pt(111). The initial monomer distribution was created by evaporating 0.01 ML of Pt onto the Pt(111) substrate at 50 K. Again, we observe a stepwise increase of the mean island size upon annealing, with monomer diffusion setting in at 95 ± 7 K, dimer diffusion at 191 ± 10 K, and trimer diffusion at 288 ± 15 K. Even though the mean island size values are not perfectly constant but rather show an increase over

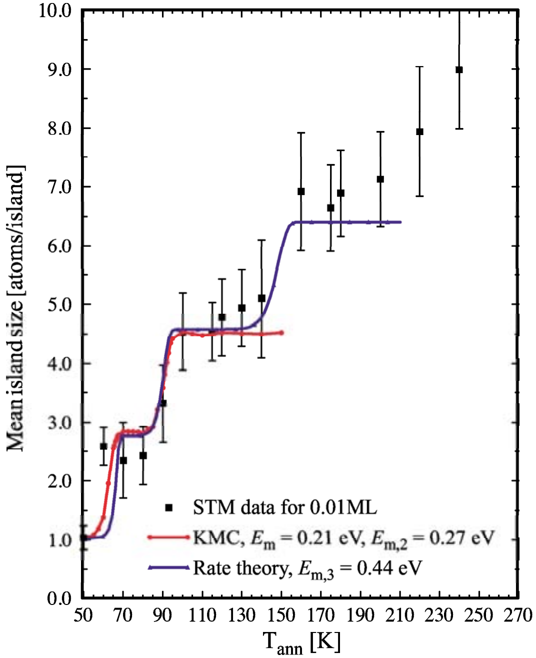

Figure 5.3: Stepwise increase of the mean island size of 0.01 ML Co on Pt(111) as a function of annealing temperature. The STM data are compared to kinetic Monte-Carlo simulations, performed by Harald Brune at EPFL-FSB-IPN (red curve), as well as to results obtained by integration of the rate equations from mean-field nucleation theory, done by Philipp Buluschek at EPFL-FSB-IPN, (blue curve).

the temperature range of 100–190 K, transition temperatures can be easily identified. We derived diffusion barrier values for Pt/Pt(111) based on the assumption that the diffusion rates $D_i = D_0 \exp(-E_{m,i}/kT)$ at the transition temperatures must be universal and hence equal to those found for the system Co/Pt(111). The diffusion rate is in fact the only temperature-dependent parameter, which enters into the set of rate equations from mean-field nucleation theory (cf. Appendix C) and the kinetic Monte-Carlo simulations. Therefore diffusion rates completely determine the variation of the mean island size with temperature. The onset temperatures of cluster diffusion are characterized by a specific ratio $E_{m,i}/T$, which is roughly $2.72 \cdot 10^{-3}$ eV/K for Co/Pt(111). We note that this corresponds to diffusion

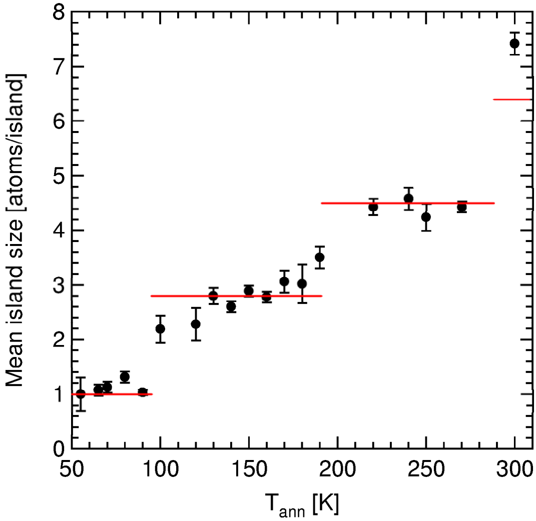

Figure 5.4: Stepwise increase of the mean island size of 0.01 ML Pt on Pt(111) as a function of annealing temperature. The lines indicate the mean island sizes as found for 0.01 ML Co on Pt(111) (Figure 5.3).

rates of $D_i \approx 5 \cdot 10^{-3}$ s^{-1} if an attempt frequency of $\nu_0 = 1 \cdot 10^{12}$ Hz is assumed. The values we deduce for the migration barriers of Pt on Pt(111) are $E_{m,1} = 0.26 \pm 0.02$ eV for monomers, $E_{m,2} = 0.52 \pm 0.03$ eV for dimers, and $E_{m,3} = 0.78 \pm 0.05$ eV for trimers.

Diffusion barriers for Pt/Pt(111) have been reported recently by other groups [109, 111–113]. Kyuno et al. [111, 112] derived migration barriers from field ion microscope observations. They found 0.260 ± 0.003 eV with an attempt frequency of $1 \cdot 10^{13}$ Hz for monomers, 0.37 ± 0.02 eV with $1 \cdot 10^{12}$ Hz for dimers, and 0.52 ± 0.01 eV with $7 \cdot 10^{12}$ Hz for trimers. Bott et al. [109] inferred a monomer migration barrier of 0.26 ± 0.01 eV with an attempt frequency of $5 \cdot 10^{12 \pm 0.5}$ Hz from STM island density measurements and Monte-Carlo simulations in the 110–160 K range. Furthermore, a diffusion barrier of 0.29 eV was calculated using density functional theory (DFT-GGA) [113]. The monomer migration barrier of 0.26 ± 0.02 eV that we find agrees perfectly with the previously reported experimental results. However, our barriers for dimer and trimer diffusion of 0.52 ± 0.03 eV and 0.78 ± 0.05 eV, respectively, are significantly higher than the values measured by Kyuno et al. [112]. We tend to attribute this divergence to a possible contamination of our Pt(111) surface during the course of annealing. Particles evaporating from the sample manipulator during heating could condense on the Pt(111) surface and impede cluster migration, which might result in apparently higher migration barriers.

Despite the rather high values we estimated for the diffusion barriers of dimers and trimers, our measurements clearly indicate that for the system Pt/Pt(111), and likewise for Co/Pt(111), dimer and trimer diffusion must take place before dissociation of the clusters. This coarsening behavior is distinctly different from that of Ag/Pt(111), where Ostwald ripening occurs owing to the dissociation of dimers followed by the one of larger islands. This one difference can be explained by the fact that the relative dissociation barriers for Pt and Co clusters on Pt(111) are higher than those for Ag on Pt(111). In fact, for Pt/Pt(111) an activation energy for Pt-dimer dissociation of 0.79–0.88 eV was calculated by DFT-GGA [113], which is significantly higher than both the dimer (0.37 ± 0.02 eV [112]) and the trimer (0.52 ± 0.01 eV [112]) diffusion barriers. For Co/Pt(111) a dissociation barrier of 0.41 eV for dimers and 0.61 eV for trimers is estimated from tight-binding molecular-dynamics simulations [114] while the migration barriers inferred above from the comparison of experiment and simulation are $E_{m,2} = 0.27 \pm 0.02$ eV and $E_{m,3} = 0.44 \pm 0.05$ eV.

5.4 Conclusions

We have monitored a stepwise increase of the mean island size upon annealing for the two systems 0.01 ML Co/Pt(111) and 0.01 ML Pt/Pt(111). The initial distribution of randomly placed monomers is followed by three subsequent regimes of constant mean island size, which relate to the onset of monomer, dimer, and trimer diffusion. The stepwise island size increase is evidence of cluster diffusion occurring at significantly lower temperatures than cluster disintegration for Co and Pt on Pt(111). Our results show that coarsening, but also nucleation, process on hexagonal surfaces can indeed be influenced by cluster diffusion, contrary to what previous results and theories suggested. For Co/Pt(111) a migration barrier of 0.21 ± 0.02 eV for monomers, 0.27 ± 0.02 eV for dimers, and 0.44 ± 0.05 eV for trimers was extracted by comparing kinetic Monte-Carlo simulation and rate equation (mean-field nucleation theory) results to the experimental data. For Pt/Pt(111) the migration barrier of 0.26 ± 0.01 eV for monomer diffusion confirms previously reported values. Theoretically estimated activation barriers for cluster dissociation are indeed higher than the barriers found for cluster diffusion [113, 114].

The ripening of the cluster distribution by cluster diffusion can be used to grow metal islands containing just a few atoms. Its advantage over cluster growth by Ostwald ripening lies in the well-defined mean cluster sizes over whole temperature ranges and in the more narrow size distributions.

Chapter 6

CO/Pt(111) Structures at High Pressures

6.1 Introduction

The studies of catalytic reactions at low temperatures are often carried out to learn something about industrial catalysts. However, the relevance of low-temperature results to real catalysts, which work at high pressures and temperatures, has often been questioned [115, 116]. For some systems experimental results obtained under UHV conditions diverge from theoretical results obtained for realistic pressures. This difference is generally referred to as "pressure gap" (see, e.g., [1]). The recent development of high-pressure STMs has allowed to bridge the pressure gap, i.e. to investigate catalytic systems on the atomic scale under conditions in-between UHV and atmospheric pressure. The results reported in this chapter have been obtained using a high-pressure STM at the Department of Physics and Astronomy at University of Aarhus, Denmark, where I was working in the group of Prof. Flemming Besenbacher.

Few adsorbate systems have received as much attention as carbon monoxide on transition metal surfaces. The enormous interest originates from the system's relevance to catalysis, since CO takes part in many important reactions such as CO hydrogenation and oxidation and the Fischer-Tropsch synthesis [117], and transition metal particles are the most common catalytic materials for these reactions. Notwithstanding these beneficial interactions, carbon monoxide is also an unwanted poison molecule in, e.g., the hydrogen feed for low-temperature fuel cells produced from hydrocarbons [118]. Since all these aspects can be traced back to adsorbate-surface interactions, it is important to acquire a thorough understanding of the properties of the adsorption of CO on transition metal surfaces.

A detailed knowledge has been gained on the adsorption of CO on Pt(111) under ultra-high vacuum (UHV) conditions (see, e.g., Refs. [119–121]). The development of surface-sensitive techniques which are capable of working at elevated pressures has renewed the interest in the CO/Pt(111) system, and a number of recent high-pressure studies have addressed the subject using various techniques [115, 116, 122, 123]. These studies revealed that carbon monoxide forms a hexagonal overlayer on Pt(111) at atmospheric pressure and room temperature. Two different structures were proposed, one close to a (4×4)-9CO non-rotated structure [116], the other one compatible with a $\left(\sqrt{19} \times \sqrt{19}\,\right)$ R23.4°-13CO commensurate structure [123]. The latter structure has also been proposed for adsorption of CO in an electrochemical cell at 0 to 0.2 V electrode potential [124]. In contrast, under UHV and low-temperature conditions a series of non-hexagonal commensurate structures is observed [119, 120, 125]. These are the c(4 × 2) or $(\sqrt{3} \times 2)$rect ($\theta = 0.5$, where θ is the coverage (number of CO molecules per substrate atom) and c$(\sqrt{3} \times 5)$rect ($\theta = 3/5$), $(\sqrt{3} \times 3)$rect ($\theta = 2/3$), and c$(\sqrt{3} \times 7)$rect ($\theta = 5/7$) structures, the latter three of which can be cast in a unified picture, in which unit strips of the c(4 × 2) are separated by domain walls of higher, structure-specific CO-density [120]. It is not clear yet, however, whether these lattice gas structures represent global or local minima of the potential energy surface.

While it was shown that a hexagonal CO overlayer can also be produced under vacuum conditions when the sample is cooled sufficiently [119, 123], the understanding of the atomic-scale details of the room temperature adsorption structures of CO on Pt(111) over the whole pressure range from UHV pressures up to atmospheric pressure is still incomplete. In particular, there is no study that has been able to unambiguously determine the adsorbate structure for the complete pressure range in between UHV and one atmosphere.

For the present study we used high-resolution scanning tunneling microscopy (STM) to unravel the room temperature adsorption structures of CO/Pt(111). At all pressures above 10^{-6} Torr[1] we observed moiré patterns characteristic for the formation of a hexagonal CO overlayer. At low CO pressures, up to 10^{-2} Torr, the moiré pattern is characterized by a superlat-

---

[1] The pressure unit Torr instead of bar is used in this chapter, for the sake of simplicity. We always adjusted and read the pressure in units of Torr using the pressure gauges of the experimental setup. A conversion into another unit would result in non-rounded, "unnatural" pressure values. Note that 1 Torr = 1.33322 mbar (cf. Appendix A).

tice vector oriented along the 30° high-symmetry direction of the substrate, while at higher CO pressures a rotation of the moiré pattern is observed. In the following we discuss these results in the context of existing theories and compare them to available UHV low-temperature data and results obtained in electrochemical cells.

6.2 Experimental

The experiments were performed in a UHV chamber equipped with a home-built Aarhus scanning tunneling microscope (STM) as well as UHV standard equipment for sample cleaning and characterization. Connected to this chamber is a gold-plated cell containing the newly developed Aarhus high-pressure STM [126]. With this STM experiments can be carried out at pressures of up to 760 Torr of pure gases or gas mixtures. Sample transfer between both systems takes place under clean conditions, i.e., without removing the sample from the vacuum. The gas exposure system of the high pressure cell has been designed to avoid nickel-carbonyl ($Ni(CO)_4$) formation, which is of utmost importance when working with CO. For that purpose the gas line has been constructed primarily using copper tubing instead of stainless steel. Furthermore, just prior to the inlet the CO is passed through an activated high surface area carbon powder filter heated to ∼400 K, over which the Ni-carbonyls dissociate leaving the Ni behind. The efficiency of this system was checked by performing Auger electron spectroscopy after extended high-pressure CO exposure and subsequent pump-out.

The sample was cleaned in the UHV chamber following standard sample cleaning procedures: 30 min. 800 eV Ar^+ sputtering, followed by an annealing procedure (in case of severely contaminated samples 10 min. annealing at 800 K in 10^{-7} Torr O_2 plus 2 min. annealing at 1000 K in UHV, otherwise just the UHV anneal). The experiments at low and medium pressure (up to $5 \cdot 10^{-4}$ Torr) were then performed in the UHV chamber, while those at higher pressures (up to 760 Torr) were performed in the high pressure cell. For pressures between 0.1 Torr to 100 Torr electric discharges between the closely-spaced piezo electrodes may occur. Therefore we always worked at a total pressure of close to 760 Torr in the high pressure cell. Due to its unreactive nature ultra-pure argon as commercially available is used for backfilling from the desired CO pressure up to the working pressure.

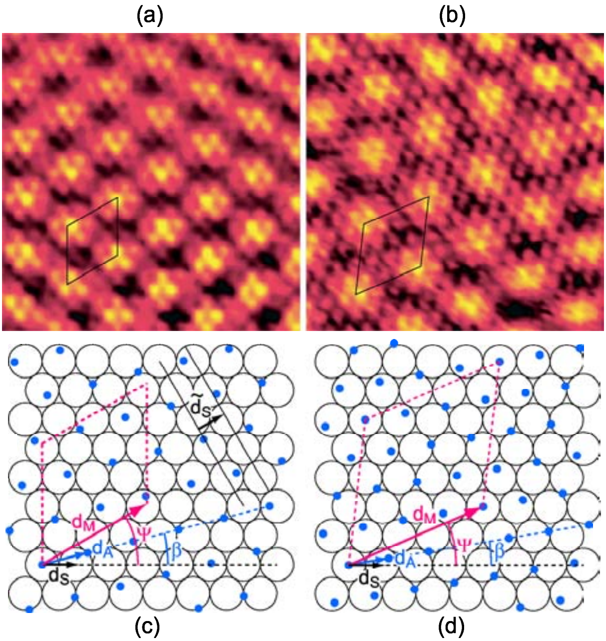

Figure 6.1: STM images of 55×55 Å^2 and corresponding ball models showing incommensurate moiré superstructures of CO on Pt(111) at room temperature. (a) $p = 10^{-2}$ Torr, $I_t = 1.06$ nA, $V_t = 8.2$ mV. (b) $p = 720$ Torr, $I_t = 1.27$ nA, $V_t = 4.9$ mV. The images (a) and (b) are aligned so that the bulk $[1\bar{1}0]$ direction is oriented along the x-axis. The image treatment comprised frequency filtering and interpolation. In the ball models in (c) and (d) the open circles represent Pt atoms and the dark blue dots CO molecules. The rotational angles β between the substrate and adsorbate lattices and Ψ between the substrate and moiré lattices are indicated. The moiré unit cell with lattice constant d_M is also shown. (c) Incommensurate structure at 10^{-2} Torr. $\Psi = 30°$, $\beta = 10.4°$, $d_M/d_S = 3.6$. $\vec{\tilde{d}}_S$ is the real space equivalent of the reciprocal vector $\vec{\tilde{q}}_S$ observed in the fast Fourier transform (cf. Fig. 6.2). $\vec{\tilde{d}}_S$ is rotated by 30° from $\vec{d}_S$ and the length relationship is $\tilde{d}_S = \sqrt{3}d_s/2$. (d) Commensurate $\left(\sqrt{19} \times \sqrt{19}\right)$ R23.4°-13CO structure at 720 Torr. $\Psi = 23.4°$, $\beta = 9.5°$, $d_M/d_S = 4.4$.

6.3 Structures and Coverage

Figure 6.1 shows two typical STM images of CO adsorbed on Pt(111) at room temperature. Image (a) was recorded at a pressure of 10^{-2} Torr, image

(b) at 720 Torr. In both images two hexagonal structures are observed at the same time, a short-periodicity and a longer-periodicity one. The short-periodicity lattice is the image of either the Pt(111) substrate (panel (a)) or the CO-overlayer (panel (b)), while the long-periodicity lattice (moiré lattice) is characterized by the periodic height modulation induced by the superposition of the hexagonal CO adlayer and the Pt(111) surface[2].

We observed quite generally that we could not image the CO molecules at pressures below 0.1 Torr (at room temperature), but instead sampled the underlying Pt(111) substrate, as in Fig. 6.1 (a). The presence of the moiré pattern with a hexagonal shape, however, proves the presence of a hexagonal CO overlayer. The invisibility of CO adsorbed on Pt and other metal surfaces is well-known to occur under certain conditions (see, e.g., Refs. [128, 129]).

Performing fast Fourier transforms (FFT) on the STM images allows one to measure the periodicities and angles of the observed structure. A typical FFT is shown in Fig. 6.2(a), and a sketch of the relevant parameters in Fig. 6.2(b). These are the reciprocal lattice vectors $\vec{\tilde{q}}_M$ of the moiré lattice, $\vec{\tilde{q}}_A$ of the adsorbate lattice, and $\vec{\tilde{q}}_S$ of the substrate lattice, which are related to each other by virtue of $\vec{\tilde{q}}_M = \vec{\tilde{q}}_A - \vec{\tilde{q}}_S$. This set of reciprocal vectors $\vec{\tilde{q}}_x$ translates into the set $\vec{q}_x$ ($x = M, S, A$), where $\vec{q}_x$ are the reciprocal space vectors of the real space vectors $\vec{d}_x$ used in Fig. 6.1, by a rotation of 30° and by virtue of $\tilde{q}_x = 2q_x/\sqrt{3}$. Hence $\vec{q}_M = \vec{q}_A - \vec{q}_S$. Ball models showing the real space vectors are given in Fig. 6.1(c) and (d). $\vec{d}_M$ and $\vec{d}_A$ form an angle Ψ and β, respectively, relative to the $[1\bar{1}0]$ direction of the substrate. From Fig. 6.2(a) it is seen that the adsorbate lattice vector can be determined even if the adsorbates are not visible in the STM image, since the moiré spots appear as satellites around the substrate spots. The substrate spots can be identified unambiguously by comparison to the Fourier transforms of images taken on the clean Pt(111) crystal. In some cases, however, the satellites were not visible in the STM. The CO lattice parameters can then be inferred from the measured moiré superlattice parameters. From Fig. 6.2(b) one can

---

[2] Note that the observation of a moiré pattern in STM is in general due to a combination of electronic and geometric effects. In fact, it has been argued that the imaging of moiré patterns in STM is not due to the modulation of the topography, but to (three-dimensional) tunneling from the buried interface [127].

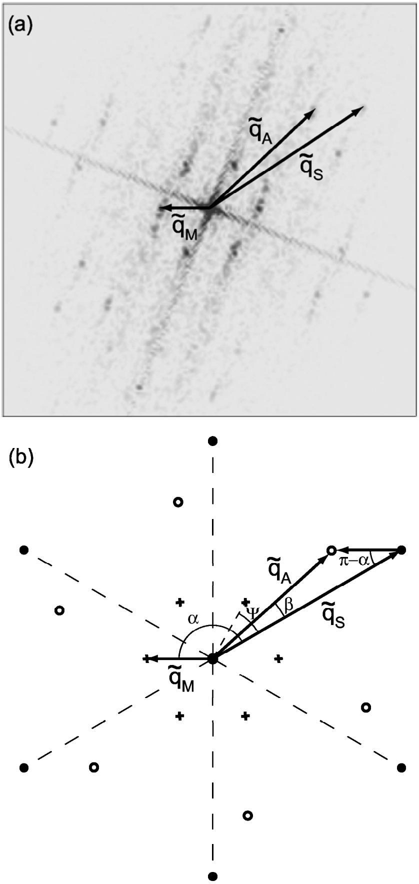

Figure 6.2: (a) Fast Fourier transform (FFT) of an STM image of a CO/Pt(111) moiré pattern (5×10^{-7} Torr). (b) Relationship between the reciprocal lattice vectors. Here, the filled circles represent the substrate lattice, the empty circles correspond to the adsorbate lattice and the crosses to the resulting moiré pattern. The observed vectors $\vec{\tilde{q}}_M$, $\vec{\tilde{q}}_S$, and $\vec{\tilde{q}}_A$ are rotated by 30° from the vectors $\vec{q}_M$, $\vec{q}_S$, and $\vec{q}_A$ used in the analysis, and the vector lengths are related via $\tilde{q}_x = 2q_x/\sqrt{3}$, where $x = M, S, A$. The moiré vector $\vec{\tilde{q}}_M$ is equal to the difference vector $\vec{\tilde{q}}_M = \vec{\tilde{q}}_A - \vec{\tilde{q}}_S$ and hence also $\vec{q}_M = \vec{q}_A - \vec{q}_S$.

derive the following formulae:

$$q_A = \sqrt{q_S^2 + q_M^2 - 2\, q_S q_M \cos(\pi - \alpha)} \tag{6.1}$$

$$\sin\beta = \frac{q_M}{q_A} \sin(\pi - \alpha) \tag{6.2}$$

$$\pi - \alpha = \frac{\pi}{3} - \Psi \tag{6.3}$$

Ψ is taken to be the smallest positive angle between substrate and moiré lattice. This set of equations allows a determination of all relevant angles and lattice vectors.

Figure 6.3 shows these parameters as a function of the CO partial pressure ranging from 10^{-6} Torr to 760 Torr. In panel (a) the moiré superlattice constant d_M is plotted in units of the Pt(111) substrate nearest neighbor distance $d_S = 2.77$ Å. In panel (b) the filled circles refer to the rotation angle Ψ between the substrate and moiré lattice and the open circles to the rotation angle β between the substrate and adsorbate lattice. In addition, crosses indicate values for β which were derived from the moiré parameters according to Equations 6.1–6.3. This procedure proved to be useful in case of barely visible satellites and gave additional confidence, since these values coincide with the β values determined directly from the images within the measurement uncertainty. From Figure 6.3(b) we can identify two regimes with different types of incommensurate moiré superstructures. In the pressure range from 10^{-6} Torr to 10^{-2} Torr we observe a moiré pattern, which is rotated by a fixed angle of $\Psi = 30°$ with respect to the Pt(111) substrate, whereas the adsorbate angle β decreases from about 14° to 10°. At the same time the lattice constant of the moiré pattern changes approximately linearly with the logarithm of CO pressure. At CO pressures above 10^{-2} Torr Ψ decreases, while β remains approximately constant at about 10°. Close to atmospheric pressure the moiré lattice constant d_M approaches a fixed saturation value.

In Figure 6.1(c) and (d) a schematic model of the CO structures observed at 10^{-2} Torr and 720 Torr is given. The ball model in panel (c) was created with the d_A and β values resulting from Equations 6.1–6.3, when using the angle Ψ and the distances d_M and d_S as determined from STM images at 10^{-2} Torr. The structure at 720 Torr is compatible with a $(\sqrt{19} \times \sqrt{19})$ R23.4°-13CO commensurate structure, and the corresponding values were used in panel (d).

It would be interesting to know more about the nature of the rotational transition between 10^{-2} and 1 Torr. In Figures 6.4 and 6.5 histograms of the Ψ angle as determined from single STM images over the whole investigated pressure range are given. Up to 10^{-2} Torr the values measured for Ψ form

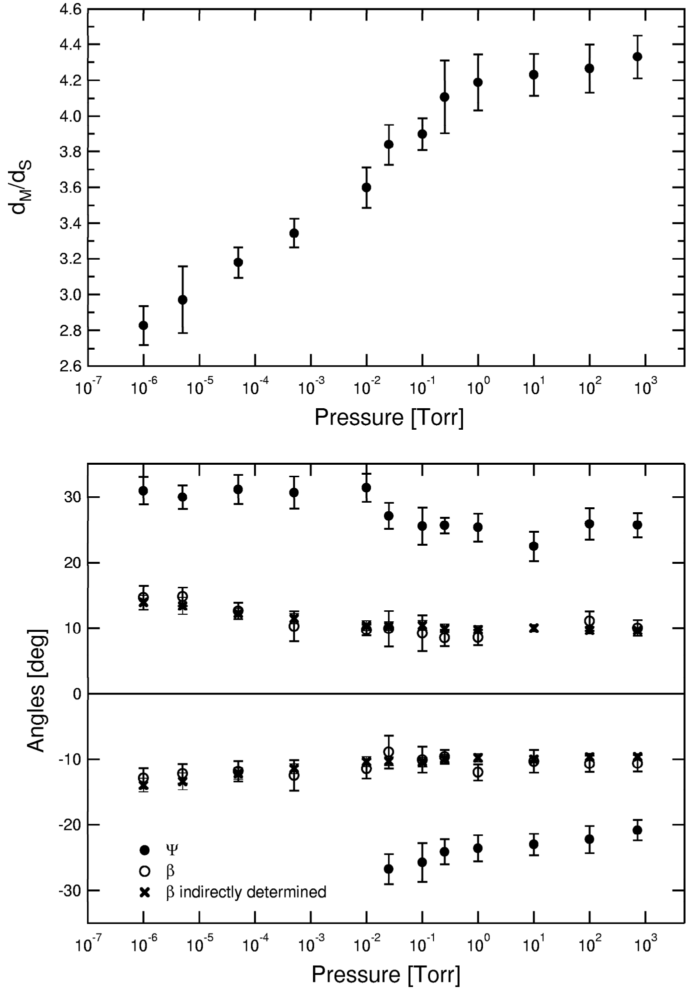

Figure 6.3: The top panel shows the measured moiré lattice constant d_M for a CO layer on Pt(111) as a function of CO partial pressure. d_M is normalized with respect to the substrate net constant d_S. In the bottom panel the rotational angles between the substrate and the moiré lattice Ψ (filled symbols) and the substrate and adsorbate lattice β (open symbols) are displayed. β is also calculated from d_M, d_S, and Ψ (crosses).

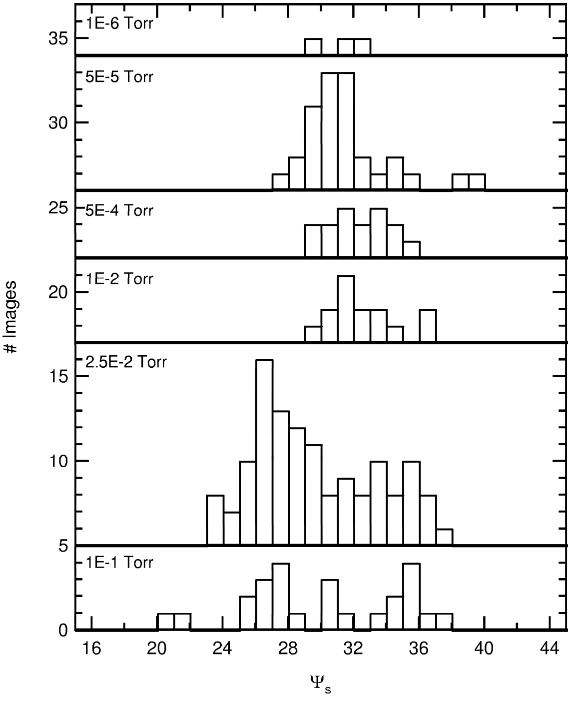

Figure 6.4: Distribution of the angle Ψ between moiré superlattice and substrate lattice for CO/Pt(111) as determined from single STM images.

a single peak centered at about 30°. In this pressure range, the moiré pattern is oriented along the high symmetry direction of 30° of the substrate and only one domain orientation can be observed. At $2.5 \cdot 10^{-2}$ Torr the single peak has broadened and starts to split into two peaks. Eventually, for pressures above 1 Torr we have two clearly separated peaks, symmetric with respect to about 30°. This means we have moiré domains, which are rotated by either $+\Psi$ or $-\Psi$. (We note that $-\Psi = 60° - \Psi$, owing to the hexagonal symmetry.) The areas of both peaks remain the same within statistical uncertainties, pointing to the fact that $\pm\Psi$ are equivalent directions in the substrate geometry. The shift of some histograms with respect to the theoretical symmetry point at exactly 30° might be caused by systematic errors, which could not be unambiguously identified.

From the STM images it is not clear what exactly happens at the rotational transition between 10^{-2}–1 Torr because of the measurement uncer-

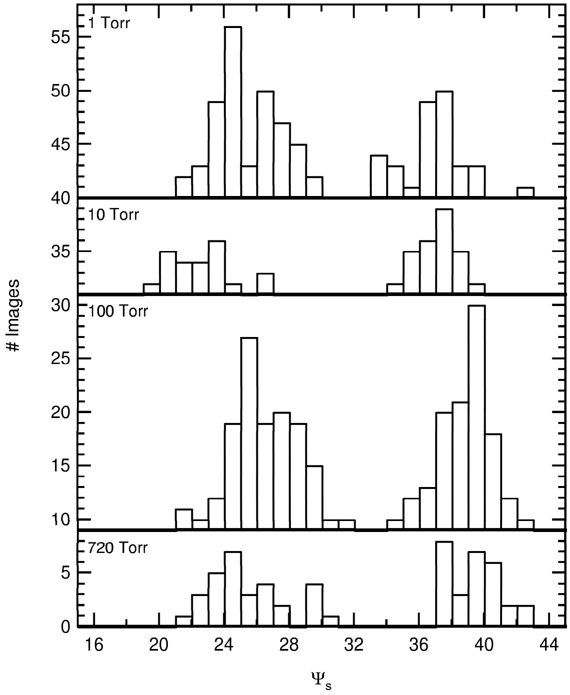

Figure 6.5: Distribution of the angle Ψ between moiré superlattice and substrate lattice for CO/Pt(111) as determined from single STM images.

tainties. The moiré domains might rotate continuously from 30° to ±24° or there might be a more abrupt transition at a certain point. We cannot discriminate between the coexistence of both moiré structures, 30° high symmetry and ±24°, and a smooth rotational transition from 30° to ±24° in the pressure range of $2.5 \cdot 10^{-2}$–10^{-1} Torr.

The variation of the CO coverage with CO partial pressure is crucial for the performance of the platinum catalyst. The coverage θ can be calculated from the substrate and adsorbate lattice constants d_S and d_A by $\theta = (d_S/d_A)^2 = (q_A/q_S)^2$. Figure 6.6 shows how the coverage increases continuously with CO pressure in the range of 10^{-8}–10^{3} Torr. The values calculated using Equations. 6.1–6.3 are consistent with the directly determined values (circles). Towards atmospheric pressures saturation of the coverage occurs due to the increasingly repulsive CO-CO interaction. Our results are in good agreement with the previously determined coverages at 10^{-8} Torr

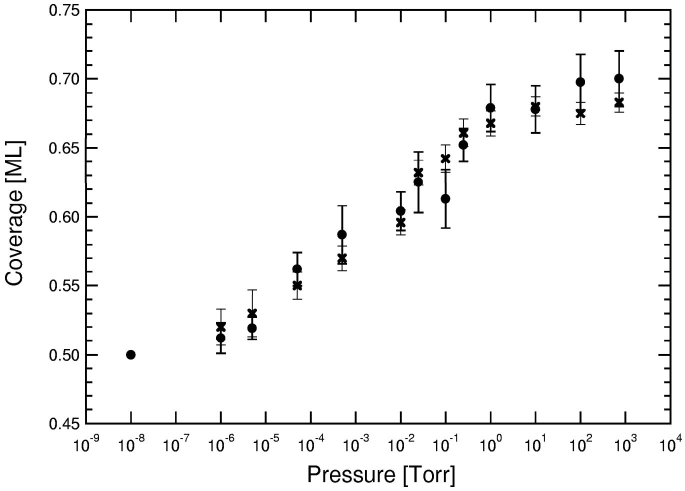

Figure 6.6: CO coverage θ on Pt(111) as a function of CO background pressure. The filled circles indicate values, which were directly determined from the STM images, while the indirectly determined values (cf. Equations 6.1–6.3) are indicated by crosses.

($\theta = 0.5$) [119] and 760 Torr ($\theta = 0.68$) [123]. The coverage given for 10^{-8} Torr corresponds to the c(4 × 2) structure observed in LEED with clear spots at temperatures below and more diffuse spots at room temperature [119].

6.4 Discussion

From Figure 6.6 it is seen that at room temperature the coverage of CO on Pt(111) varies continuously over the pressure range from 10^{-6} to 760 Torr. The finding of a continuous variation of the CO coverage with pressure and the observation of hexagonal, ordered overlayer structures for all pressures above 10^{-6} Torr contrasts with the CO/Pt(111) lattice gas structures found in the same coverage range at lower pressures and temperatures [119, 120, 125]. The formation of lattice gas structures would lead to a phase diagram with alternating regimes of ordered and disordered CO overlayers [120]. Nevertheless, a true pressure gap is not observed for the CO/Pt(111) system since sufficient cooling of the sample to approximately −100°C leads to a considerable increase in CO coverage and the formation of a hexagonal CO overlayer similar to that at 760 Torr [123].

The formation of moiré structures has been observed previously for a large variety of adsorbate systems. For example, moiré patterns for CO overlayers have been reported for the Ni(111) [130], Ag(111) [131], and graphite [132] substrates, and, at a pressure of ~760 Torr, also for the CO/Pt(111) system [116, 123]. Generally, the occurrence of moiré patterns can always be expected when the molecular lateral repulsive potential V_l balances or exceeds the corrugation ΔU of the adsorbate-substrate interaction potential. In the $V_l \gg \Delta U$ and infinite lattice limit the resulting structure can be viewed as a mere superposition of two perfect, in the present case hexagonal lattices of the substrate and adsorbate.

In case $V_l \approx \Delta U$ the situation is more complicated and has received considerable theoretical interest [133–143]. The various theories predict an alignment of the moiré vector in preferred directions if the molecular positions are allowed to relax [133–139] and/or if the system has a finite size [140–143]. The theory of Bohr and Grey [140–143] invokes a "high-symmetry hypothesis" according to which the adsorbate layer rotates by an angle β such that the resulting incommensurate moiré superlattice is either oriented along a high-symmetry direction of the substrate or along a high-symmetry direction of the adsorbate layer. Numerical calculations showed that these situation corresponds to an energy minimum, since the number of adsorbates in or close to low-energy sites is maximized [141–143]. This maximization is solely due to a finite-size effect, with relaxation only resulting in a second-order correction. We will discuss this finding in more detail later on.

In Fig. 6.7 the rotation angle β of the CO lattice with respect to the Pt substrate as a function of the lattice misfit $(d_A - d_S)/d_S$ is compared to the high-symmetry (30° and 60°) solutions relevant for the (111) surface. Also shown is the theoretical harmonic approximation solution derived by Novaco and McTague for a Lennard-Jones system [133, 136][3]. At coverages below 0.6, which corresponds to misfit values of 0.3–0.4, the experimental data points are found to be in good agreement with the $\Psi_S = 30°$ solution found from the high-symmetry hypothesis, i.e., the moiré vector aligns with the 30° high-symmetry direction of the substrate (which corresponds to the $[1\bar{2}1]$ direction in fcc bulk notation). For misfit values smaller than 0.3, however, a deviation from the theoretical lines is observed. As the compression of the CO layer continues, i.e., for smaller values of $(d_A - d_S)/d_S$, β remains constant at approximately 10° within the error bars, whereas Ψ decreases from 30° to about ±24° (cf. Fig. 6.3).

The alignment of the moiré vector with the 30° substrate direction indi-

---

[3] Anharmonic extensions of the theory of Novaco and McTague have also been formulated, see Refs. [134, 135, 139]

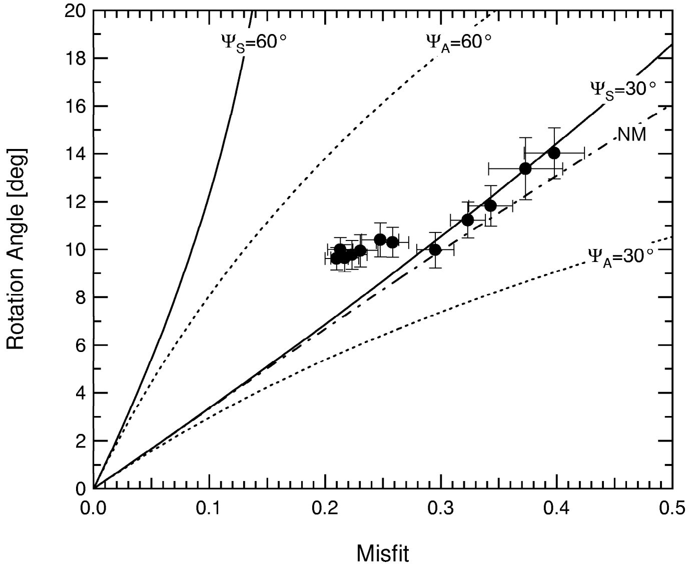

Figure 6.7: Rotation angle between CO adlayer and Pt(111) substrate as a function of the lattice misfit between d_A and d_S, $(d_A - d_S)/d_S$. The solid and short-dashed lines indicate the theoretical high-symmetry solutions of Ref. [142] and the dash-dotted line the harmonic approximation of Ref. [136] for a Lennard-Jones system. Ψ_S: rotation angle of moiré superlattice with respect to the substrate. Ψ_A: rotation angle of moiré superlattice with respect to the adsorbate.

cates that the particular rotation of the adsorbate layer is due to the finite size of the substrate [142, 143]. The role of the substrate boundaries is played by the substrate steps, which are oriented along the $[1\bar{1}0]$ and equivalent directions. It would be interesting to confirm this result in experiments using samples with varying step densities.

As established above the moiré vector does not align with any of the substrate high symmetry directions at pressures above 10^{-2} Torr. This shows that the energy gain associated with this transition (see discussion below) does not give a sufficiently high impetus to achieve the rotation. We can analyze the situation in more detail by taking the form of the substrate interaction potential U and the strength of the lateral interaction V_l into account. The exact form of V_l has not yet been determined (see Refs. [144–147]), but an approximation is given by the semi-empirical CO-CO pairwise interaction potential in Ref. [148]. A qualitative sketch of U is given in Fig. 6.8 and Table 6.1 reproduces some potential parameters, derived from the semi-empirical single molecule potential curve of Ref. [148]. The top sites are energetically most favorable, followed by the bridge sites [119–121]. Here we assume that the maximum of the potential energy barrier U_{tb} between top and bridge sites lies below the local potential energy minimum U_h at hollow sites, which is in agreement with the calculations in Ref. [145] and the experimental findings of Ref. [124]. As a consequence the hollow sites are not occupied over the whole investigated pressure range in agreement with the results of Ref. [124]. This does not contradict the observation of a hexagonal superstructure since we expect the adsorbed CO molecule positions to be relaxed, which can also include slight tilts, with respect to a perfect hexagonal overlayer. In addition, the area of the near-hollow sites amounts to a relatively small fraction of the total surface area only, so that these sites do not necessarily have to be occupied in a close-to hexagonal overlayer.

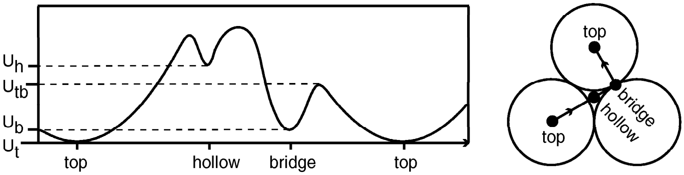

Figure 6.8: Qualitative potential energy curve for an isolated CO molecule on Pt(111) along the lines connecting the top, bridge and hollow sites.

Relevant for a comparison of the lateral interaction energy and the corrugation of the substrate potential are the barriers between the different sites. In the analysis we have to take into account that the measurements are carried out at room temperature. A crude estimation for the effective barrier height is derived by assuming parabolic and isotropic oscillators. The resulting values for the effective barriers between the bridge and on-top sites, $\Delta U_{tb-t} \equiv U_{tb} - \langle U_t \rangle - U_t$ as seen from the on-top potential energy minimum and $\Delta U_{tb-b} \equiv U_{tb} - \langle U_b \rangle - U_b$ as seen from the bridge minimum, are given in Table 6.1. ΔU_{tb-t} and ΔU_{tb-b} represent the room temperature effective barrier heights relative to the mean energy of the molecule inside the potential wells (see the Table caption), which were assumed to be parabolic, while U_t, U_b, and U_{tb} are the parameters of the potential energy surface for the on-top and bridge sites and the barrier between these [148] (cf. Fig. 6.8). For the on-top sites the lateral repulsion energy V_l is smaller

$T(K)$	U_t	U_b	U_{tb}	$\langle U_t\rangle$	$\langle U_b\rangle$	ΔU_{tb-t}	ΔU_{tb-b}	$V_l^{\theta=0.5}$	$V_l^{\theta=0.6}$
0	0	60	300	6	37	294	203	200	290
300	0	60	300	52	60	248	180	200	290

Table 6.1: Parameters of the employed substrate interaction potential and the lateral interaction. All energies are given in meV. $\Delta U_{tb-t} \equiv U_{tb}$-$\langle U_t\rangle$-$U_t$ and $\Delta U_{tb-b} \equiv U_{tb}$-$\langle U_b\rangle$-$U_b$ represent effective barrier heights relative to the mean energy of the molecule inside the potential wells, which were assumed to be parabolic. These effective barrier heights are derived assuming isotropic oscillators with energies $\langle U_{t,b}\rangle = \hbar\omega_{t,b} + \hbar\omega_{t,b}/\left(\exp\left(\frac{\hbar\omega_{t,b}}{kT}\right) - 1\right)$, where $\hbar\omega_t = 48$ cm^{-1} and $\hbar\omega_b = 300$ cm^{-1} are the vibrational motion frequencies in the top and bridge positions, respectively [148]. The values defining the potentials $(U_t, U_b, U_{tb}$, and $V_l)$ have been taken to be temperature-independent.

than the barrier height ΔU_{tb-t} at the onset of the high-symmetry moiré phase with $\theta \sim 0.5$. At $\theta \sim 0.6$, corresponding to the rotational transition at 10^{-2} Torr, V_l is essentially equal to ΔU_{tb-t}. In contrast, it is found that the barrier as seen from the bridge sites, ΔU_{tb-b}, is smaller than the lateral repulsion V_l over the entire coverage range of 0.5–0.6. This indicates that it is the occupation of top sites which is decisive for the formation of the high-symmetry moiré phase at lower CO pressures.

At pressures above 10^{-2} Torr the orientation of the moiré superstructure along the high symmetry direction $\Psi = 30°$ is not maintained. Hence, the rotation concomitant with such an alignment is not favorable anymore, and instead the CO adsorbate layer keeps a constant orientation with respect to the substrate. In this pressure regime the lateral repulsion exceeds the barrier height between the on-top and bridge position, irrespective of whether these are measured with reference to the bridge (ΔU_{tb-b}) or on-top site (ΔU_{tb-t}). As a consequence the importance of the CO molecules to occupy (near) top sites is reduced. We propose that it is the increasing dominance of the lateral repulsion over the barrier height ΔU_{tb-t}, which causes the deviation from the high symmetry direction just above 10^{-2} Torr.

However, near to 760 Torr the occupation of top sites again becomes decisive, namely for the formation of a commensurate $\left(\sqrt{19} \times \sqrt{19}\right)$ R23.4°-13CO structure. In this commensurate structure a high number of CO molecules can sit exactly on top sites. We note that the electrochemical study of Villegas and Weaver [124] indicates that going from negative to slightly positive sample bias leads to a switching from a (2×2)-

3CO structure to the $\left(\sqrt{19} \times \sqrt{19}\right)$ R23.4°-13CO system. The rotation concomitant with such a transformation indicates an enhanced stability of the $\left(\sqrt{19} \times \sqrt{19}\right)$ structure. Together with the present results this finding suggests that the occupancy of a high number of on-top sites to some extent can outweigh the lateral repulsion even at high coverages.

The energy gain due to the formation of the commensurate $\left(\sqrt{19} \times \sqrt{19}\right)$ R23.4°-13CO structure is judged to be higher than the energy gain that would result from a reorientation of the incommensurate moiré superstructure along $\Psi = 30°$ just above 10^{-2} Torr. We suggest that above 10^{-2} Torr the lateral forces are sufficient to exceed the corrugation of the substrate potential. Hence a simple reorientation along a high symmetry direction is prevented, but not the formation of a particularly stable commensurate structure.

6.5 Conclusions

We have determined the room temperature surface structure of CO on Pt(111) over the whole background pressure range of 10^{-6}–760 Torr. For all pressures the formation of a hexagonal or quasi-hexagonal CO overlayer is observed. This shows that for CO/Pt(111) a true pressure gap cannot be established. Nevertheless, extreme care has to be taken when relating UHV results to systems operating under realistic conditions such as atmospheric pressure. One has to consider (a) the existence of different commensurate vacuum structures on cooled samples (see, e.g., [119, 120]) and (b) the subtle differences between the reported hexagonal structures in terms of the adsorbate layer rotation angle.

More in detail, the CO adsorbate layer is continuously compressed with increasing pressure resulting in a continuous coverage variation from 0.5–0.7. The orientation of the moiré superlattice is pressure-dependent. First, for coverages between ~ 0.5 and 0.6 the moiré pattern is oriented by 30° with respect to the $[1\bar{1}0]$ direction of the Pt(111) substrate. This orientation can be explained in terms of a maximal occupation of high-binding energy sites for a substrate of finite size [142, 143], where the size is given by the surface terraces. Second, at a coverage of 0.6 the system undergoes a rotational phase transition. Above this coverage the angle of the adsorbate layer with respect to the substrate does not change anymore. We explain this behavior in terms of an increasing importance of the repulsive lateral molecular interaction, which starts to dominate over the corrugation of the substrate interaction potential. A quantitative analysis based on previous results [148] supports our explanation.

Bibliography

[1] G. A. Somorjai, *Introduction to surface chemistry and catalysis* (John Wiley & Sons, Inc., 1994).

[2] B. K. Burgess and D. J. Lowe, Chem. Rev. **96**, 2983 (1996).

[3] O. Einsle, F. A. Tezcan, S. L. A. Andrade, B. Schmid, M. Yoshida, J. B. Howard, and D. C. Rees, Science **297**, 1696 (2002).

[4] T. H. Rod, B. Hammer, and J. K. Nørskov, Phys. Rev. Lett. **82**, 4054 (1999).

[5] T. H. Rod, A. Logadottir, and J. K. Nørskov, J. Chem. Phys. **112**, 5343 (2000).

[6] T. H. Rod and J. K. Nørskov, Surf. Sci. **500**, 678 (2002).

[7] C. R. Henry, ed., *Surface Science Studies of the Basic Mechanisms of Heterogeneous Catalysis*, Physics of surfaces, 3ième séminaire Rhodanien de Physique (Editions Frontières, Dolomieu, France, 1996).

[8] T. Zambelli, J. Wintterlin, J. Trost, and G. Ertl, Science **273**, 1688 (1996).

[9] B. Hammer, Phys. Rev. Lett. **83**, 3681 (1999).

[10] S. Dahl, E. Törnqvist, and I. Chorkendorff, J. Cat. **192**, 381 (2000).

[11] B. C. Stipe, M. A. Rezaei, and W. Ho, Science **280**, 1732 (1998).

[12] M. Bäumer and H.-J. Freund, Prog. Surf. Sci. **61**, 127 (1999).

[13] C. Becker, A. Rosenhahn, W. Wiltner, K. v. Bergmann, J. Schneider, P. Pervan, M. Milun, M. Kralj, and K. Wandelt, New J. Phys. **4**, 75.1 (2002).

[14] S. Schintke, S. Messerli, M. Pivetta, F. Patthey, L. Libioulle, M. Stengel, A. D. Vita, and W.-D. Schneider, Phys. Rev. Lett. **87**, 2768011 (2001).

[15] I. Giaever, Rev. Mod. Phys. **46**, 245 (1974).

[16] W. A. Thompson and S. F. Hanrahan, Rev. Sci. Instr. **47**, 1303 (1976).

[17] R. D. Young, Rev. Sci. Instr. **37**, 275 (1966).

[18] G. Binnig, H. Rohrer, C. Gerber, and E. Weibel, Appl. Phys. Lett. **40**, 178 (1982).

[19] G. Binnig and H. Rohrer, Rev. Mod. Phys. **59**, 615 (1987).

[20] G. Binnig and H. Rohrer, Rev. Mod. Phys. **71**, S324 (1999).

[21] R. Young, J. Ward, and F. Scire, Rev. Sci. Instr. **43**, 999 (1972).

[22] R. Young, J. Ward, and F. Scire, Phys. Rev. Lett. **27**, 922 (1971).

[23] G. Binnig, H. Rohrer, C. Gerber, and E. Weibel, Phys. Rev. Lett. **49**, 57 (1982).

[24] G. Binnig, H. Rohrer, C. Gerber, and E. Weibel, Phys. Rev. Lett. **50**, 120 (1983).

[25] G. Binnig and H. Rohrer, Surf. Sci. **126**, 236 (1983).

[26] G. Binnig, H. Rohrer, C. Gerber, and E. Weibel, Phys. Rev. Lett. **55**, 991 (1985).

[27] R. Garcìa, J. J. Sáenz, and N. Garcìa, Phys. Rev. B **33**, 4439 (1986).

[28] A. M. Baró, R. Miranda, J. Alamán, N. García, G. Binnig, H. Rohrer, C. Gerber, and J. L. Carrascosa, Nature **315**, 253 (1985).

[29] O. Marti, G. Binnig, H. Rohrer, and H. Salemink, Surf. Sci. **181**, 230 (1987).

[30] T. Michely, *Rastertunnelmikroskopuntersuchung der Morphologie von Pt(111) nach Ionenbeschuss, Jül-Bericht 2569* (Forschungszentrum Jülich, Jülich, 1991).

[31] M. Bott, T. Michely, and G. Comsa, Rev. Sci. Instr. **66**, 4135 (1995).

[32] D. M. Eigler and E. K. Schweizer, Nature **344**, 524 (1990).

[33] I.-W. Lyo and P. Avouris, Science **253**, 173 (1991).

[34] L. Bürgi, Ph.D. thesis, Ecole Polytechnique Fédérale de Lausanne (1999).

[35] D. A. Bonnell, ed., *Scanning Tunneling Microscopy and Spectroscopy: Theory, Techniques, and Applications* (VCH Publishers, Inc., New York, 1993).

[36] C. J. Chen, *Introduction to scanning tunneling microscopy* (Oxford University Press, Inc., 1993).

[37] J. Tersoff and D. R. Hamann, Phys. Rev. Lett. **50**, 1998 (1983).

[38] J. Tersoff and D. R. Hamann, Phys. Rev. B **31**, 805 (1985).

[39] J. Bardeen, Phys. Rev. Lett. **6**, 57 (1961).

[40] A. Selloni, P. Carnevali, E. Tosatti, and C. D. Chen, Phys. Rev. B **31**, 2602 (1985).

[41] N. D. Lang, Phys. Rev. B **34**, 5947 (1986).

[42] J. A. Stroscio, R. M. Feenstra, and A. P. Fein, Phys. Rev. Lett. **57**, 2579 (1986).

[43] A. Zangwill, *Physics at surfaces* (Cambridge University Press, 1988).

[44] G. Ertl and J. Küppers, *Low Energy Electrons and Surface Chemistry* (VCH Verlagsgesellschaft mbH, Weinheim, 1985), 2nd ed.

[45] B. C. Stipe, M. A. Rezaei, and W. Ho, Phys. Rev. Lett. **80**, 1724 (1999).

[46] L. J. Lauhon and W. Ho, Rev. Sci. Instr. **72**, 216 (2001).

[47] B. C. Stipe, M. A. Rezaei, and W. Ho, Rev. Sci. Instr. **70**, 137 (1999).

[48] A. Hirstein, Ph.D. thesis, Ecole Polytechnique Fédérale de Lausanne (1998).

[49] H. Jödicke, Ph.D. thesis, Ecole Polytechnique Fédérale de Lausanne (1999).

[50] G. Meyer, Rev. Sci. Instr. **67**, 2960 (1996).

[51] S. Behler, M. K. Rose, J. C. Dunphy, D. F. Ogletree, M. Salmeron, and C. Chapelier, Rev. Sci. Instr. **68**, 2479 (1997).

[52] J. H. Ferris, J. G. Kushmerick, J. A. Johnson, M. G. Y. Youngquist, R. B. Kessinger, H. F. Kingsbury, and P. S. Weiss, Rev. Sci. Instr. **69**, 2691 (1998).

[53] *Thermophysical properties of matter*, The TPRC Data Series (Perdue Research Foundation, 1970).

[54] F. Pobell, *Matter and methods at low temperatures* (Springer-Verlag, 1996), 2nd ed.

[55] *Omega Temperature Handbook* (Omega Engineering, Inc., 2000).

[56] D. R. Lide, *CRC Handbook of Chemistry and Physics* (CRC Press LLC, 2000), 81st ed.

[57] M. Okano, K. Kajimura, S. Wakiyama, F. Sakai, W. Mizutani, and M. Ono, J. Vac. Sci. Technol. A **5**, 3313 (1987).

[58] J. A. Stroscio and W. J. Kaiser, *Scanning tunneling microscopy* (Academic Press, Inc., 1993).

[59] K. Nagaya, J. Dyn. Sys. Meas. Control **106**, 52 (1984).

[60] W. T. Thomson, *Theory of vibration with applications* (Chapman & Hall, 1993), 4th ed.

[61] S. Behler, M. K. Rose, D. F. Ogletree, and M. Salmeron, Rev. Sci. Instr. **68**, 124 (1997).

[62] B. Gasser, A. Menck, H. Brune, and K. Kern, Rev. Sci. Instr. **67**, 1925 (1996).

[63] M. H. Jericho, D. C. Dahn, and B. L. Blackford, Rev. Sci. Instr. **58**, 1349 (1987).

[64] B. Fischer, Ph.D. thesis, Ecole Polytechnique Fédérale de Lausanne (1998).

[65] K. Besocke, Surf. Sci. **181**, 145 (1987).

[66] J. Frohn, J. F. Wolf, K. Besocke, and M. Teske, Rev. Sci. Instr. **60**, 1200 (1989).

[67] J.-M. Breguet, Ph.D. thesis, Ecole Polytechnique Fédérale de Lausanne (1998).

[68] H. Brune, *Diploma thesis, Fritz-Haber Institut der Max Planck Gesellschaft* (Berlin, 1989).

[69] J. M. Soler, A. M. Baró, N. Garcìa, and H. Rohrer, Phys. Rev. Lett. **57**, 444 (1986).

[70] C. Xu and D. W. Goodman, Chem. Phys. Lett. **263**, 13 (1996).

[71] H. Brune, M. Giovannini, K. Bromann, and K. Kern, Nature **394**, 451 (1998).

[72] U. Heiz, A. Sanchez, S. Abbet, and W.-D. Schneider, J. Am. Chem. Soc. **121**, 3214 (1999).

[73] S. Abbet, A. Sanchez, U. Heiz, W.-D. Schneider, A. M. Ferrari, G. Pacchioni, and N.Rösch, Surf. Sci. **454–456**, 984 (2000).

[74] K. Bromann, C. Felix, H. Brune, W. Harbich, R. Monot, J. Buttet, and K. Kern, Science **274**, 956 (1996).

[75] S. A. Chambers, Surf. Sci. Rep. **39**, 105 (2000).

[76] M. C. Gallagher, M. S. Fyfield, L. A. Bumm, J. P. Cowin, and S. A. Joyce, Thin Solid Films **445**, 90 (2003).

[77] A. Rosenhahn, J. Schneider, C. Becker, and K. Wandelt, J. Vac. Sci. Technol. A **18**, 1923 (2000).

[78] W. Weiss and W. Ranke, Prog. Surf. Sci. **70**, 1 (2002).

[79] Y. J. Kim, C. Westphal, R. X. Ynzunza, Z. Wang, H. C. Galloway, M. Salmeron, M. A. V. Hove, and C. S. Fadley, Surf. Sci. **416**, 68 (1998).

[80] Y. J. Kim, C. Westphal, R. X. Ynzunza, H. C. Galloway, M. Salmeron, M. A. V. Hove, and C. S. Fadley, Phys. Rev. B **55**, R13448 (1997).

[81] H. C. Galloway, J. J. Benítez, and M. Salmeron, Surf. Sci. **298**, 127 (1993).

[82] G. H. Vurens, M. Salmeron, and G. A. Somorjai, Surf. Sci. **201**, 129 (1988).

[83] C. Di Valentin, G. Pacchioni, S. Abbet, and U. Heiz, J. Phys. Chem. B **106**, 7666 (2002).

[84] S. Abbet, E. Riedo, H. Brune, U. Heiz, A. M. Ferrari, L. Giordano, and G. Pacchioni, J. Am. Chem. Soc. **123**, 6172 (2001).

[85] J. Wollschläger, D. Erdös, and K.-M. Schröder, Surf. Sci. **402-404**, 272 (1998).

[86] J. Wollschläger, J. Viernow, C. Tegenkamp, D. Erdös, K. M. Schröder, and H. Pfnür, Appl. Surf. Sci. **142**, 129 (1999).

[87] M.-C. Wu, J. S. Corneille, C. A. Estrada, J.-W. He, and D. W. Goodman, Chem. Phys. Lett. **182**, 472 (1991).

[88] J. S. Corneille, J.-W. He, and D. W. Goodman, Surf. Sci. **306**, 269 (1994).

[89] Y. Kim, J. Stultz, and D. Goodman, Surf. Sci. **506**, 228 (2002).

[90] M. C. Gallagher, M. S. Fyfield, J. P. Cowin, and S. A. Joyce, Surf. Sci. **339**, L909 (1995).

[91] H. Xu and K. Y. S. Ng, Surf. Sci. **356**, 19 (1996).

[92] H. Xu and K. Y. S. Ng, Surf. Sci. **355**, L305 (1996).

[93] S. H. Kim and P. C. Stair, Surf. Sci. **457**, L347 (2000).

[94] G. J. Dooley and T. W. Haas, J. Vac. Sci. Technol. **7**, S90 (1970).

[95] E. Bauer and H. Poppa, Surf. Sci. **88**, 31 (1979).

[96] C. Zhang, M. A. Vanhove, and G. A. Somorjai, Surf. Sci. **149**, 326 (1985).

[97] M. C. Gallagher, M. S. Fyfield, and S. A. Joyce, Phys. Rev. B **59**, 2346 (1999).

[98] D. F. Droppo, C. D. Storey, and M. C. Gallagher, Phys. Rev. B **62**, 1623 (2000).

[99] M. C. Wu, J. S. Corneille, C. A. Estrada, J. W. He, and D. W. Goodman, Chem. Phys. Lett. **182**, 472 (1991).

[100] L. D. López-Carreño, G. Benítez, L. Viscido, J. M. Heras, F. Yubero, J. P. Espinós, and A. R. González-Elipe, Surface and Interface Analysis **26**, 235 (1998).

[101] D. Wu, W. K. Lau, Z. Q. He, Y. J. Feng, M. S. Altman, and C. T. Chan, Phys. Rev. B **62**, 8366 (2000).

[102] H. Brune, Surf. Sci. Rep. **31**, 121 (1998).

[103] H. Röder, E. Hahn, H. Brune, J. P. Bucher, and K. Kern, Nature **366**, 141 (1993).

[104] H. Brune, in *Physics of Covered Solid Surfaces*, edited by H. P. Bonzel (Springer, Berlin, 2001), vol. 42A of *Landolt Börnstein Series*, pp. 217–258.

[105] A. Gölzhäuser and G. Ehrlich, Phys. Rev. Lett. **77**, 1334 (1996).

[106] H. Brune, G. S. Bales, J. Jacobsen, C. Boragno, and K. Kern, Phys. Rev. B **60**, 5991 (1999).

[107] J. A. Venables, Philosophical Magazine **27**, 697 (1973).

[108] W. Ostwald, Z. Phys. Chem. **34**, 495 (1900).

[109] M. Bott, M. Hohage, M. Morgenstern, T. Michely, and G. Comsa, Phys. Rev. Lett. **76**, 1304 (1996).

[110] M. C. Bartelt, S. Günther, E. Kopatzki, R. J. Behm, and J. W. Evans, Phys. Rev. B **53**, 4099 (1966).

[111] K. Kyuno, A. Golzhauser, and G. Ehrlich, Surf. Sci. **397**, 191 (1998).

[112] K. Kyuno and G. Ehrlich, Surf. Sci. **437**, 29 (1999).

[113] P. J. Feibelman and T. Michely, Surf. Sci. **492**, L723 (2001).

[114] C. Goyhenex (2004), personal communication.

[115] X. Su, P. S. Cremer, Y. R. Shen, and G. A. Somorjai, Phys. Rev. Lett. **77**, 3858 (1996).

[116] J. A. Jensen, K. B. Rider, M. Salmeron, and G. A. Somorjai, Phys. Rev. Lett. **80**, 1228 (1998).

[117] G. Ertl, H. Knözinger, and J. Weitkamp, eds., *Handbook of Heterogenuous Catalysis*, vol. 1-5 (Wiley-VCH, Weinheim, 1997).

[118] L. Carrette, K. A. Friedrich, and U. Stimming, Fuel Cells **1**, 5 (2001).

[119] G. Ertl, M. Neumann, and K. M. Streit, Surf. Sci. **64**, 393 (1977).

[120] B. N. J. Persson, M. Tushaus, and A. M. Bradshaw, J. Chem. Phys. **92**, 5034 (1990).

[121] J.-S. McEwen, S. H. Payne, H. J. Kreuzer, M. Kinne, R. Denecke, and H.-P. Steinrück, Surf. Sci. **545**, 47 (2003).

[122] G. Rupprechter, T. Dellwig, H. Unterhalt, and H.-J. Freund, J. Phys. Chem. B **105**, 3797 (2001).

[123] E. K. Vestergaard, P. Thostrup, T. An, E. Lægsgaard, I. Stensgaard, B. Hammer, and F. Besenbacher, Phys. Rev. Lett. **88**, 259601 (2002).

[124] I. Villegas and M. J. Weaver, J. Chem. Phys. **101**, 1648 (1994).

[125] J. P. Biberian and M. A. v. Hove, Surf. Sci. **118**, 443 (1982).

[126] E. Lægsgaard, L. Österlund, P. Thostrup, P. B. Rasmussen, I. Stensgaard, and F. Besenbacher, Rev. Sci. Instr. **72**, 3537 (2001).

[127] K. Kobayashi, Phys. Rev. B **53**, 11091 (1996).

[128] P. Thostrup, E. K. Vestergaard, T. An, E. Lægsgaard, and F. Besenbacher, J. Chem. Phys. **118**, 3724 (2003).

[129] P. T. Sprunger, F. Besenbacher, and I. Stensgaard, Chem. Phys. Lett. **243**, 439 (1995).

[130] C. Quiros, O. Robach, H. Isern, P. Ordejon, and S. Ferrer, Surf. Sci. **522**, 161 (2003).

[131] G. S. Leatherman and R. D. Diehl, Langmuir **13**, 7063 (1997).

[132] W. Steele, Chem. Rev. **93**, 2355 (1993).

[133] A. D. Novaco and J. P. McTague, Phys. Rev. Lett. **38**, 1286 (1977).

[134] J. Villain, Phys. Rev. Lett. **41**, 36 (1978).

[135] A. D. Novaco, Phys. Rev. B **19**, 6493 (1979).

[136] J. P. McTague and A. D. Novaco, Phys. Rev. B **19**, 5299 (1979).

[137] H. Shiba, J. Phys. Soc. Jpn. **46**, 1852 (1979).

[138] H. Shiba, J. Phys. Soc. Jpn. **48**, 211 (1980).

[139] J. Villain and M. B. Gordon, Surf. Sci. **125**, 1 (1983).

[140] F. Grey and J. Bohr, in *Phase Transitions in Surface Films 2*, edited by H. Taub, G. Torzo, H. Lauter, and J. S.C. Fain (Plenum Press, New York, 1990), vol. B 267 of *NATO ASI Series*, pp. 83–96.

[141] F. Grey and J. Bohr, Appl. Surf. Sci. **65-6**, 35 (1993).

[142] F. Grey and J. Bohr, Europhys. Lett. **18**, 717 (1992).

[143] J. Bohr and F. Grey, Cond. Matt. News **1**, 12 (1992).

[144] D. R. Jennison, P. A. Schultz, and M. P. Sears, Phys. Rev. Lett. **77**, 4828 (1996).

[145] P. v. Beurden, H. G. J. Verhoeven, and G. J. Kramer, Phys. Rev. B **66**, 235409 (2002).

[146] R. Brako and D. Šokčević, Surf. Sci. **401**, L338 (1998).

[147] N. V. Petrova and I. N. Yakovkin, Surf. Sci. **519**, 90 (2002).

[148] E. Schweizer, B. N. J. Persson, M. Tüshaus, D. Hoge, and A. M. Bradshaw, Surf. Sci. **213**, 49 (1989).

Appendix A

Acronyms and Unit Conversion

Acronyms:

AES	Auger electron spectroscopy
DFT	Density functional theory
ETP	Electrolytic tough pitched
LEED	Low-energy electron diffraction
LDOS	Local density of states
IETS	Inelastic electron tunneling spectroscopy
OFHC	Oxygen-free high conductivity
STM	Scanning tunneling microscopy/ microscope
VT-STM	Variable-temperature scanning tunneling microscopy/ microscope

Unit conversion:

Pressure: 1 mbar = 10^2 Pa
1 Torr = 1.33322 mbar = $1.33322 \cdot 10^2$ Pa
1 atm = 760 Torr = $1.01325 \cdot 10^3$ mbar = $1.01325 \cdot 10^5$ Pa
Temperature: Temperature [°C] = Temperature [K] - 273.15
Length: 1” (1 in) = 25.4 mm

Appendix B

Frequency Characteristics of a Piezoceramic Tube

In this section I'm showing that the voltage reading at an electrode of our piezoceramic tubes exhibits the frequency characteristics of an RC circuit.

The following reference measurement was performed in the framework of the measurements described in Section 3.5.2.

We applied a sinusoïdal signal to one outer electrode of a piezoceramic tube using the internal oscillator of a lock-in amplifier, and measured the voltage at the opposite electrode. This voltage is induced by the deformation of the tube due to the applied voltage on the opposite side. In our case the inner electrode is always grounded. When reading the voltage, the instrument "sees" in principle the current flowing from or to the electrode. This current produces a voltage drop over the instrument entrance impedance, which is proportional to the value indicated on the instrument display.

Basically, we have an RC device, where the capacitance is that between the outer and the inner electrode of the piezoceramic tube, and the resistance is the entrance resistance of the lock-in amplifier. This means that at small frequencies the voltage at the entrance impedance of the instrument approaches zero. In fact we do not obtain any signal for a constant deflection of our tube, though the induced voltage cannot be zero according to piezoelectric theory. Figure B.1 shows the measured amplitude and phase versus frequency for a single free piezoceramic tube together with the theoretical RC curve. The measured curves follow the theoretical ones almost perfectly in the frequency range from 10 Hz to about 10 kHz. The cutoff frequency $f = (2\pi RC)^{-1}$ lies at 21.5 Hz for the present resistance and capacitance values. This high cutoff frequency relates to the fact that C is very small in

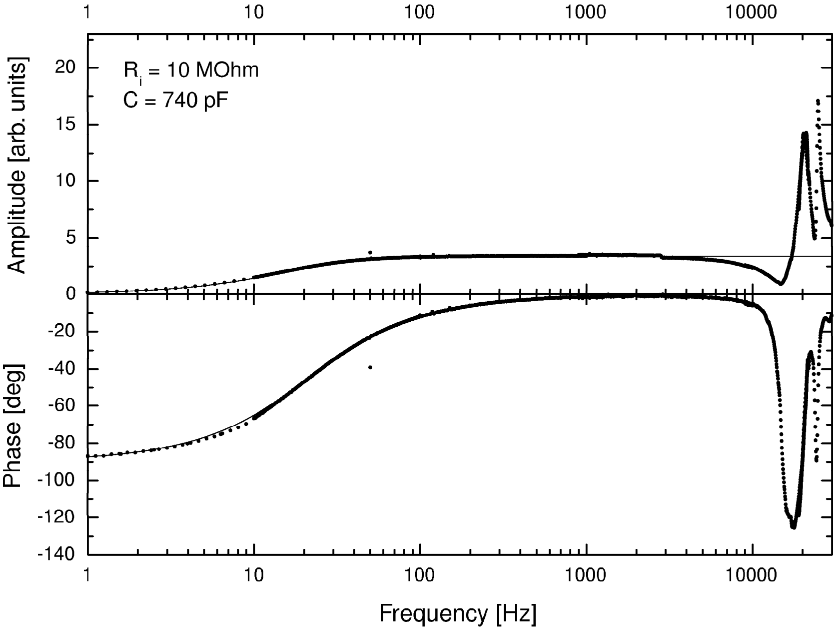

Figure B.1: Voltage reading at an outer electrode of a piezoceramic tube upon sinusoïdal excitation of the opposite electrode.

our case and the electrodes are very quickly discharged.

The origin of the observed two, rather broad, resonances in the range of 10–30 kHz is not clear. They cannot be clearly attributed to a bending or stretching eigenmode of the tube.

Appendix C

Mean-Field Nucleation Theory

In this appendix the simple rate equations used for comparison with our results of Chapter 5 shall be outlined.

Rate equations are used in classical mean-field nucleation theory. In the most simple scenario the atoms arriving from the gas phase diffuse with rate D on the surface and upon encounter with another adatom they form a stable dimer. The dimer remains immobile and grows into a larger cluster if it is joined by other single atoms. One can write down the rate equations for this growth process [102]:

$$\frac{\mathrm{d}n_1}{\mathrm{d}t} = F - 2\sigma_1 D n_1^2 - \sigma_x D n_1 n_x - \kappa_x F(Ft - n_1) - 2\kappa_1 F n_1 \quad \text{(C.1)}$$

$$\frac{\mathrm{d}n_x}{\mathrm{d}t} = \sigma_1 D n_1^2 + \kappa_1 F n_1 \quad \text{(C.2)}$$

F denotes the particle flux, i.e. the number of impinging atoms per surface unit cell and unit time. n_1 and n_x are the density and σ_1 and σ_x the capture rates of monomers and larger clusters, respectively. κ_1 and κ_x are the cross sections for impingement of atoms from the gas phase onto existing islands. The first term in Equation C.1 represents the increase of monomers due to the incoming atoms from the gas phase. The second term stands for the formation of a dimer when two monomers meat while the third term accounts for the capture of a monomer by a larger cluster. The two last terms consider the impingement of incoming atoms directly onto existing stable islands and monomers. In Equation C.2 the first term corresponds to the formation of a new dimer upon encounter of two monomers and the second term to the impingement of a gas atom onto an existing monomer.

The diffusion rate D represents the mean number of unit cells visited by an isolated random walker per unit time and is given by [102]

$$D = \left(\frac{\nu_0}{4}\right) \mathrm{e}^{-\frac{E_m}{kT}} \ , \tag{C.3}$$

where ν_0 is the attempt frequency, T the temperature, k the Boltzmann constant, and E_m the migration barrier. The rate equations are temperature-dependent via the diffusion rate D. Numerical integration of the rate equations C.1–C.2 provides theoretical island densities as a function of temperature, which can be compared to measurement results obtained by VT-STM, allowing the extraction of the parameters E_m and ν_0.

The rate equations can be extended for the case of diffusing dimers and trimers. The diffusion of the different clusters is determined by their migration barriers $E_{m,i}$ and attempt frequencies $\nu_{0,i}$.

Acknowledgments

I'm thankful to all people who contributed to the present work.

Mein erster Dank geht an Harald Brune, dafür dass er mich in seine Gruppe aufgenommen hat und damit diese sehr lehrreiche und interessante Arbeit ermöglicht hat. Harri war allzeit zu Diskussionen bereit und für meine Wünsche offen. Seine Ruhe und Kompetenz haben mir sehr viel geholfen.

J'aimerais remercier ma collaboratrice Elisa Riedo, qui a travaillé comme post-doc avec moi sur la même chambre UHV durant trois ans. Elisa m'a aidée beaucoup avec son optimisme, sa gentillesse, et son humour, surtout quand je ne voyais plus le bout du tunnel. J'aimerais remercier Imad Arfaoui, qui a travaillé comme post-doc avec Elisa et moi sur la chambre UHV pendant plus d'une année et sur le STM pendant mon absence, pour ses conseils, son grand engagement et sa générosité.

J'ai beaucoup apprécié de pouvoir faire des mesures STM avec Stefano Rusponi et Tristan Cren dans le laboratoire "à côté". Je remercie Stefano et Tristan pour le bon accueil et pour tous leurs conseils et leur aide tout au long de ma thèse. Je remercie également Philipp Buluschek pour les calculs en rapport avec nos résultats et ses explications précieuses.

J'aimerais remercier André Guisolan et tous les mécaniciens, Philippe Zürcher, Gilles Grandjean, Claude Blanc, et Pascal Cattin, qui étaient toujours de bonne humeur, pour tous les excellents travaux qu'ils ont fait pour nous. Je remercie également Michel Fazan pour son travail sur les pièces céramiques, ainsi que les électriciens Philippe Cordey et José Grandjean. Tous ces gens étaient toujours prêts à m'aider et à me donner de précieux conseils.

Ich möchte mich bei Wolfgang Harbich für all seine guten Ideen und Tipps und sein immer hilfreiches Urteil, was den Aufbau des STMs anbelangt, bedanken, und bei Max Epple für all seine Arbeit, seine Erklärungen und seine Hilfe bezüglich der STM Elektronik und Software. Je tiens aussi à remercier Stéphane Pons pour sa contribution au montage de l'STM lors de mon séjour à Aarhus.

Je remercie tous les membres du groupe et de l'institut, qui m'ont souvent donné un coup de main au laboratoire ou m'ont aidée d'une autre façon.

I'm much obliged to Flemming Besenbacher for letting me work in his impressive laboratories at the University of Aarhus. I very much enjoyed my stay in his group and could learn a lot. I'm grateful to all people with whom I had the pleasure to work in Aarhus, in particular to Joachim Schnadt, Ronnie Vang, and Ebbe Kruse Vestergaard for their help and for receiving me so well in their laboratory. Ich danke insbesondere Joachim Schnadt für

all seine Hilfe und Erklärungen, für all die interessanten Diskussionen und für seine Grosszügigkeit.

Ich bedanke mich bei Katharina Franke, die nun als Postdoktorandin in unserem Labor arbeitet und das STM sowie unsere Kammer übernommen hat. Katharina hat die letzten Monate für mich sehr viel schöner gemacht und mich zuversichtlich gestimmt durch ihre Kompetenz und Motivation.

Ich bin Wolfram Luithardt und Katharina Franke dankbar für das Lesen von Teilen dieses Manuskripts und hilfreiche Vorschläge.

Finalement, j'aimerais aussi remercier Philipp Aebi, Giovanni Dietler, et Claude Henry pour avoir jugé ce travail.

Ich danke meiner Familie und Freunden und allen, die mein Leben bereichert haben während meiner Doktorarbeit. Ich danke besonders auch allen Menschen, die mich aufgemuntert haben, wenn ich es brauchte.

Ich danke zutiefst meinem Ehemann Ralf, für sein Dasein und seine Liebe.

Curriculum Vitae

Name: Sarah Rebekka Longwitz(-Jans)
Date of birth: 28 February 1976
Nationality: Swiss

2000–2004: Research and teaching assistant

Group of Prof. H. Brune,
Institut de Physique des Nanostructures,
Ecole Polytechnique Fédérale de Lausanne
(two months in group of Prof. F. Besenbacher, University of Aarhus, Denmark)
Ph.D. thesis title: ”*Design of a variable-temperature scanning tunneling microscope to study reaction intermediates in heterogeneous catalysis*”

1995–2000: Studies in physics, lic. phil. nat.

Universität von Bern

1998–2000: Diploma student and teaching assistant

Group of Prof. P. Bochsler,
Institut for Space Physics and Planetology
(one month in group of Prof. W. Heiland, Universität Osnabrück, Germany)

Diploma thesis title: ”*Ionization of Energetic Neutral Atoms for Application in Space Instrumentation*”

1998: Exchange student
Università degli Studi di Pavia, Italy

1991–1995: Maturité type C (sci.-math.)

Collège Ste-Croix, Fribourg

Publications:

- *Stepwise increase of the mean island size in ripening by cluster diffusion*, S. Rusponi, S.R. Longwitz, T. Cren, P. Buluschek, E. Vargoz, C. Goyhenex, K. Kern, and H. Brune, in preparation.
- *Ordered Superstructure of MgO(100) on Mo(100) Caused by Interfacial Mo(100)-c(14×2)-O Reconstruction*, I. Arfaoui, S.R. Longwitz, E. Riedo, U. Heiz, and H. Brune, in preparation.
- *High-coverage structures of carbon monoxide adsorbed on Pt(111) studied by high-pressure scanning tunneling microscopy*, S.R. Longwitz, J. Schnadt,

E. Kruse Vestergaard, R.T. Vang, E. Lægsgaard, I. Stensgaard, H. Brune, and F. Besenbacher, accepted for publication in J. Phys. Chem..

- *Scattering of atoms and molecules off a barium-zirconate surface*, S. Jans, P. Wurz, R. Schletti , K. Brüning, K. Sekar, W. Heiland, J. Quinn, and R.E. Leuchtner, Nucl. Instr. Meth. B **173** (2001) 503–515.
- *Negative ion production by surface ionization at aluminum-nitride surfaces*, S. Jans, P. Wurz, R. Schletti, T. Fröhlich, E. Hertzberg, and S. Fuselier, J. Appl. Phys. **87** (2000) 2587–2592.